Photonic nanojet for nano-scale imaging and spectroscopy

By

Harishankar Patel

PHYS03201104001

Raja Ramanna Centre for Advanced Technology,
Indore-452013, India

A thesis submitted to the

Board of Studies in Physical Sciences

In partial fulfillment of requirements

for the Degree of

DOCTOR OF PHILOSOPHY

of

HOMI BHABHA NATIONAL INSTITUTE

August, 2018

Homi Bhabha National Institute[1]

Recommendations of the Viva Voce Committee

As members of the Viva Voce Committee, we certify that we have read the dissertation prepared by Harishankar Patel entitled "Photonic nanojet for nano-scale imaging and spectroscopy" and recommend that it may be accepted as fulfilling the thesis requirement for the award of Degree of Doctor of Philosophy.

Chairperson – Prof. K. S. Bindra		**Date:** 29-03-2019
Guide / Convener – Prof. S. K. Majumder		**Date:** 29/3/19
Examiner- Prof. B. V. R. Tata		**Date:** 29/03/2019
Member 1- Prof. S. R. Mishra	S R Mishra	**Date:** 29-3-19
Member 2- Prof. A. Moorti	Anand Moorti	**Date:** 29/3/2019
Member 3- Prof. P. K. Mukhopadhyay		**Date:** 29.3.19
Member 4- Prof. C. Mukherjee		**Date:** 29.3.19
External Member - Prof. V. Ganeshan		**Date:** 29-03-2019

Final approval and acceptance of this thesis is contingent upon the candidate's submission of the final copies of the thesis to HBNI.

I hereby certify that I have read this thesis prepared under my direction and recommend that it may be accepted as fulfilling the thesis requirement.

Date: 29/3/19

Place: RRCAT, Indore

S. K. Majumder

[1] This page is to be included only for final submission after successful completion of viva voce.

Version approved during the meeting of Standing Committee of Deans held during 29-30 Nov 2013

STATEMENT BY AUTHOR

This dissertation has been submitted in partial fulfillment of requirements for an advanced degree at Homi Bhabha National Institute (HBNI) and is deposited in the Library to be made available to borrowers under rules of the HBNI.

Brief quotations from this dissertation are allowable without special permission, provided that accurate acknowledgement of source is made. Requests for permission for extended quotation from or reproduction of this manuscript in whole or in part may be granted by the Competent Authority of HBNI when in his or her judgment the proposed use of the material is in the interests of scholarship. In all other instances, however, permission must be obtained from the author.

Harishankar Patel

DECLARATION

I, hereby declare that the investigation presented in the thesis has been carried out by me. The work is original and has not been submitted earlier as a whole or in part for a degree / diploma at this or any other Institution / University.

Harishankar Patel

List of publications arising from the thesis

Journal

1. “Photonic nanojet assisted enhancement in transmission of light through hollow pyramid shaped near field probes”, **H. S. Patel,** P. K. Kushwaha, M. K. Swami, and P. K. Gupta, J. Opt. **2015**, 17, 05500.
2. “Wavelength encoded polarization measurements for simultaneous spectral and polarimetric characterization in near field”, **H. S. Patel,** M. K. Swami, P. K. Kushwaha, A. Uppal and P. K. Gupta, J. Opt. **2016,** 18, 085002.
3. “Photonic nanojet assisted enhancement of Raman signal: Effect of refractive index contrast”, **H. S. Patel,** P. K. Kushwaha, M. K. Swami, J. Appl. Phys. **2018,** 123, 023102.
4. “Generation of highly confined photonic nanojet using crescent-shape refractive index profile in microsphere”, **H. S. Patel,** P. K. Kushwaha, M. K. Swami, Opt. Comm. **2018**, 415, 140–145.

Conferences

1. “Controlled shaping of photonic nanojets using core shell microspheres”, P. K. Kushwaha, **H. S. Patel,** M. K. Swami and P. K. Gupta, SPIE 9654, 96541H 1-7 (2015). doi:10.1117/12.2182806
2. “Spectrally encoded polarization sensitive near field optical microscopy”, **H. S. Patel,** M. K. Swami, P. K. Kushwaha, A. Uppal and P. K. Gupta, Proceedings of International Conference on Optics and Photonics (ICOP-2015) held at University of Calcutta during February 20-22, 2015.

3. “Controlled shaping of photonic nanojets using core shell microspheres”, P. K. Kushwaha, **H. S. Patel,** M. K. Swami and P. K. Gupta, Proceedings of ICOP-2015 held at University of Calcutta during February 20-22, 2015. This paper was selected for publication in SPIE proceedings.
4. “Interaction of Gaussian beam with microspheres: Effect of off-axis excitation”, P. K. Kushwaha, C. P. K. Jayanath, M. K. Swami, A. Uppal, **H. S. Patel** and P. K. Gupta, Proceeding of National Laser Symposium NLS22, held at Manipal University during January 8-11, 2014.

Harishankar Patel

ACKNOWLEDGEMENTS

First of all, I would like to express my profound gratitude to Dr. P. K. Gupta under whose supervision major part of the thesis work was completed. I am also highly indebted to Dr. S. K. Majumder for kindly agreeing to supervise the remaining dissertation work.

Thesis work has taken longer that what I had planned initially due to several reasons and it has resulted in a large number of members joining and leaving the doctoral committee. I am grateful to all past and present committee members, Dr. S. Sarkar, Dr. T. P. A. Devasagayam, Dr. D. K. Palit, Dr. I. Priyadarshini, Dr. D. K. Aswal, Dr. V. Ganeshan, Dr. (Ms.) Rama Chari, Dr. A. Dube Dr. K. Das, Dr. K. S. Bindra, Dr. S. R. Mishra, Dr. A. Moorty, Dr. P. K. Mukhopadhyay and Dr. C. Mukherjee for their encouragement and insightful comments.

I wish to thank all members of the Laser Biomedical Applications Section, for help rendered by them directly or indirectly in completion of this thesis.

Last but not the least I would like to thank my family and friends for their loving support and comfort. Thank you all.

Table of contents

Synopsis

Generation, manipulation and utilization of photons on the sub-wavelength scale is an intensely pursued research area because it holds promise for making further breakthroughs in the already widespread applications of photonics in different aspects of human endeavor e.g. optical communication, optical computing, energy harvesting, health care etc. to name a few. Not surprisingly this field referred to as Nanophotonics is a very rapidly growing area. Over the past decade, a rather simple yet efficient approach has emerged for generating high intensity beam of light with sub-wavelength lateral confinement often referred to as photonic nanojet (PNJ). PNJ is generated when a loss-less dielectric micro-particle of appropriate size and refractive index is illuminated with an electromagnetic wave. Generation of PNJ was first predicted by Chen et al. [1] in 2004 using numerical simulation of the electromagnetic field in and around a micrometer sized cylindrical dielectric object under plane wave illumination. Since then, objects of a variety of size, shape and refractive index have been studied for generating PNJ with the desired characteristics. The first experimental demonstration of the PNJ was made by Kong et al. [2] by reading data from sub-wavelength sized pits using nanojet of microwaves radiation. Soon after, generation of PNJ with visible light illumination of a dielectric microsphere was reported by Ferrand et al. [3].

The formation of PNJ is a not a resonance phenomenon and has been shown to be relatively insensitive to the deformations and surface corrugations [4, 5]. Therefore, PNJs can be observed for a wide range of size and shapes of the micro-particles and wavelength of the illumination, provided the ratio of the refractive index of the microsphere and the surrounding medium is less than 2:1 [6]. Because of their ability to confine the light to sub-wavelength spatial dimensions PNJ has emerged as a simple and cost effective approach for localized illuminations/collection of scattered light for high resolution imaging and spectroscopy [7-10]. For the effective utilization of PNJs for these applications it is desirable to be able to control the parameters of a PNJ like length, width, peak intensity and working distance [11]. While the PNJ with a shorter width are desirable for achieving better confinement and higher peak intensity, many high resolution far field applications require elongated PNJ with length extending up to several wavelengths along the direction of propagation [12,13]. There are two ways by which such a control can be exercised. One approach is to vary the size, shape and refractive index of the micro-particle [14-16] and the other is to vary the parameters of the excitation electromagnetic wave such as beam parameters, phase and polarization etc. [17, 18]. One of the objectives of the work reported in this thesis was to investigate different ways to control the parameters of PNJ. Studies carried out by us show that control of the geometry and refractive index contrast of a core-shell microsphere provides a relatively simpler approach for the generation of nanojet with controllable length and confinement. While the generation of a highly elongated PNJ is possible when refractive index of the core is less than that of the shell, better confinement is obtained when core has a higher refractive index than the host microsphere. Best lateral confinement was obtained when the inclusion microsphere touches the surface of the shell at the point of emission of nanojet forming a crescent shaped refractive index profile in the microsphere. These studies showed that by tuning the refractive indices of different layers in eccentric core-shell microsphere, it is possible to generate either extremely confined (FWHM ~ $\lambda/4.5$) or highly elongated (length ~27λ) photonic nanojet.

The sub-diffraction limit confinement of light in a PNJ makes it a promising candidate for optical super-resolution imaging. A micron sized transparent microsphere placed in contact with the sample directly or through a nanopipet attachment for raster scanning have been shown to be able to collect and relay high spatial frequency information and provide resolution beyond the diffraction limit [7, 9]. However, performance of the microsphere based nanoscope is highly sensitive to the relative refractive indices of the microsphere, sample and the surrounding medium. One of the most common optical techniques employed for super-resolution imaging is near field scanning optical microscope (NSOM). In a typical NSOM system either a metal coated pulled optical fiber probe or a cantilever with hollow pyramid-shaped tip having nano meter size aperture is used for confining the excitation light to sub-diffraction spot size. Because a large fraction of light launched in these probes is reflected back or lost as heat in the metal coating due to the sub-wavelength aperture size, throughput of these probes is low, typically $\sim 10^{-5}$–10^{-6} for pulled optical fiber probe and up to an order of magnitude better for the hollow pyramid probes. Increasing the power input to the probe is also not a solution because it may cause thermal damage to the probe or result in damage to the sample in contact with a heated probe. We have therefore investigated the feasibility of using dielectric microspheres to improve the coupling of light into the probe and thus enhance its throughput. For this we considered a modified NSOM probe with a microsphere of suitable size and refractive index inserted into the hollow pyramid shaped cantilever. The theoretical simulations and experimental results show that with an appropriate choice of the dielectric microsphere an order of magnitude enhancement in transmission of the probe is possible.

In conventional NSOM, refractive index contrast resulting in intensity variation from different regions of the sample is used to obtain image information. A large number of samples like magneto-optical material, anisotropic nano-structures and photosensitive polymers also produce distinct near field response to the optical polarization and provide improvement in the contrast and information content. We have developed a scheme for polarization sensitive near field imaging of nano-structured samples by making use of broadband polarized near field illumination and detection of polarization states of scattered light by spectrally encoded analyzer. The analyzer comprising a combination of polarizer, a multi-order waveplate and a broadband quarter waveplate allows analyzing the spectrally encoded polarization states of scattered light for characterization of the polarization properties of nano structures from a single image scan. The scheme was validated by measuring the near field polarization parameters of silver nanowires. The approach allows simultaneous measurement of polarization characteristics as well as spectral features of the nano materials.

The large enhancement in local field due to sub-wavelength confinement of light in PNJ can also be utilized for enhancing weak Raman signals. We investigated the use of PNJ for enhancement of Raman signal from different substrate materials of varying refractive index. The results of our study show that the degree of enhancement is strongly dependent on the refractive index contrast of the sample with respect to the microsphere and increases with an increase in the refractive index of the sample. This happens because for a given microsphere as the refractive index of the substrate is lowered the length of PNJ gets elongated. This not only leads to a reduction in the intensity of the excitation beam but the collection efficiency for the Raman signal from the elongated excitation volume in the confocal collection geometry used also gets reduced. We also showed experimentally that by decoupling the optical path for excitation and collection, Raman signal from sample with lower refractive index can be also be significantly enhanced.

The thesis has been organized as follows:

In **Chapter 1** we first discuss the fundamental aspects of the interaction of the electromagnetic waves with dielectric microscopic objects. A brief survey of literature on the generation and manipulation of PNJ is presented next. This is followed by a discussion on the use of PNJ for various nano-photonic applications. Finally an overview of the major objectives of the work reported in the thesis is provided.

In **Chapter 2** we discuss the computational tools available for numerical solution of the Maxwell equations. Both analytical approach for solving the Maxwell's equations (which are applicable for scatterers of regular shapes like microsphere, cylinders and ellipsoids) and numerical approaches that allow computation of the field for objects with arbitrary shape and refractive index profile are discussed. Particular emphasis is paid to the finite-element method (FEM) and the discrete dipole approximation (DDA) based approach for computing the field distribution in PNJ generated by dielectric micro-particles because these have been extensively used for the work reported in this thesis. Details of the near field scanning optical microscope used for performing the measurements presented in the thesis are also discussed.

In **Chapter 3** we describe the various approaches investigated by us for control of the characteristics of photonic nanojets. Results obtained on the controlled manipulation of axial and lateral dimensions of the PNJ by core shell microsphere and multilayer crescent shape refractive index profile are presented. We also discuss the results of numerical simulations which show that the flux emerging from microspheres can be tuned in angle by off-axis excitation using a tightly focused Gaussian beam.

In **Chapter 4** we describe the results of the experimental investigations carried out by us on the use of photonic nanojet for near field imaging application. The results show that apart from an order of magnitude enhancement in the throughput the approach also leads to an improved contrast in near field imaging as well as faster image acquisition. The approach offers several other advantages. Since the formation of photonic nanojet is a non-resonant phenomena the enhancement in transmission is independent of wavelength. Further, it was found that the coupling of light into the modified probe also gets considerably simplified as the transmission through such tip is relatively less sensitive to the axial and lateral offset between the beam waist and symmetry axis of the probe tip.

In **Chapter 5** we discuss the nanojet assisted imaging of near field polarization properties of the nano structure. The approach presented in this chapter allows simultaneous retrieval of the near field polarization properties and spectral characteristics of nano structure from single image scan.

In **Chapter 6** we describe the results of the investigations carried out on the use of PNJ for enhancement of Raman signal from different substrate material of varying refractive index contrast with respect to the microsphere. The reasons for the relatively low enhancement observed for samples with low refractive index are discussed and the approach we proposed and validated for improving the enhancement is discussed in detail.

In **Chapter 7** we provide a summary of the results of the work carried out as a part of this thesis and discuss future scope in the field.

References

[1]. Z. G. Chen, A. Taflove, and V. Backman, Photonic nanojet enhancement of backscattering of light by nanoparticles: a potential novel visible-light ultra-microscopy technique, Opt. Exp. 12, 1214 (2004).

[2]. S.C. Kong, A. V. Sahakian, A. Heifetz, A. Taflove, and V. Backman, Robust detection of deeply sub-wavelength pits in simulated optical data-storage disks using photonic jets, Appl. Phys. Lett. 92, 211102 (2008).

[3]. P. Ferrand, J. Wenger, A. Devilez, M. Pianta, B. Stout et al., Direct imaging of photonic nanojets, Opt. Exp. 16, 6930 (2008).

[4]. I. Mahariq and H. Kurt, On-and off-optical-resonance dynamics of dielectric micro-cylinders under plane wave illumination, J. Opt. Soc. Am. B 32, 1022 (2015).

[5]. I. Mahariq, V.N. Astratov and H. Kurt, Persistence of photonic nanojet formation under the deformation of circular boundary, J. Opt. Soc. Am. B 33, 535 (2015).

[6]. B. Lukyanchuk, R. P. Domínguez, I. Minin, O. Minin and Z. Wang, Refractive index less than two: photonic nanojets yesterday, today and tomorrow, Opt. Mat. Exp. 7, 1820 (2017).

[7]. Z. Wang, W. Guo, L. Li, B. Lukyanchuk, A. Khan et al. Optical virtual imaging at 50 nm lateral resolution with a white-light nanoscope, Nat. Comm. 2, 218 (2111).

[8]. D. Gérard, A. Devilez, H. Aouani, B. Stout, N. Bonod et al., Efficient excitation

and collection of single molecule fluorescence close to a dielectric microsphere, J. Opt. Soc. Am. B 26, 1473 (2009).

[9]. I. Alessandri and J. R. Lombardi, Enhanced Raman Scattering with Dielectrics, Chem. Rev. 116, 14921 (2016).

[10]. P. K. Upputuri, Z. Wu, L. Gong, C. K. Ong and H. Wang, Super-resolution coherent anti-Stokes Raman scattering microscopy with photonic nanojets, Opt. Exp. 22, 12890 (2014).

[11]. G. Gu, R. Zhou, Z. Chen, H. Xu, G. Cai et al., Super-long photonic nanojet generated from liquid-filled hollow micro-cylinder, Opt. Lett. 40, 625 (2015).

[12]. Y. Shen, L. Wang and J. Shen, Ultralong photonic nanojet formed by a two-layer dielectric microsphere, Opt. Lett. 39, 4120 (2014).

[13]. P. Wu, J. Li, K. Wei and W. Yue, Tunable and ultra-elongated photonic nanojet generated by a liquid-immersed core–shell, dielectric microsphere Appl. Phys. Exp. 8, 112001 (2015).

[14]. Y. Geints, E. Panina and A. Zemlyanov, Control over parameters of photonic nanojets of dielectric microspheres, Opt. Comm. 283, 4775(2010).

[15]. I. Minin, O. Minin and Y.Geints, Localized EM and photonic jets from non-spherical and non-symmetrical dielectric mesoscale objects: Brief review, Ann. Phys. Berlin 527, 491 (2015).

[16]. C. Y. Liu and F. C. Lin, Geometric effect on photonic nanojet generated by dielectric micro-cylinders with non-cylindrical cross-sections, Opt. Comm. 380, 287 (2016).

[17]. M. S. Kim, T. Scharf, S. Mühlig, C. Rockstuhl and H. P. Herzig, Engineering photonic nanojets, Opt. Exp. 19, 10206 (2011).

[18]. M. Wu, R. Chen, J. Soh, Y. Shen, L. Jiao, J. Wu, X. Chen, R. Ji and M. Hong, Super-focusing of center-covered engineered microsphere, Sci. Rep. 6, 31637 (2016).

Publications arising from the work presented in the thesis

Journals

1. Photonic nanojet assisted enhancement in transmission of light through hollow pyramid shaped near field probes.

   H. S. Patel, P. K. Kushwaha, M. K. Swami, and P. K. Gupta, Journal of Optics 17, 05500 (2015).

2. Wavelength encoded polarization measurements for simultaneous spectral and polarimetric characterization in near field.

   H. S. Patel, M. K. Swami, P. K. Kushwaha, A. Uppal and P. K. Gupta, Journal of Optics 18, 085002 (2016).

3. Photonic nanojet assisted enhancement of Raman signal: Effect of refractive index contrast.

   H. S. Patel, P. K. Kushwaha and M. K. Swami J. Appl. Phys. 123, 023102 (2018).

4. Generation of highly confined photonic nanojet using crescent-shape refractive index profile in microsphere.

   H. S. Patel, P. K. Kushwaha and M. K. Swami, Opt. Comm. 415, 140–145 (2018).

Conferences

1. Controlled shaping of photonic nanojets using core shell microspheres.

   P. K. Kushwaha, **H. S. Patel,** M. K. Swami and P. K. Gupta, SPIE 9654, 96541H 1-7 (2015). doi:10.1117/12.2182806

2. Spectrally encoded polarization sensitive near field optical microscopy.

   H. S. Patel, M. K. Swami, P. K. Kushwaha, A. Uppal and P. K. Gupta, Proceedings of International Conference on Optics and Photonics (ICOP 2015) held at University of Calcutta during February 20-22, 2015.

3. Controlled shaping of photonic nanojets using core shell microspheres.

   P. K. Kushwaha, **H. S. Patel,** M. K. Swami and P. K. Gupta, Proceedings of ICOP-2015 held at University of Calcutta during February 20-22, 2015. This paper was selected for publication in SPIE proceedings.

4. Interaction of Gaussian beam with microspheres: Effect of off-axis excitation.

   P. K. Kushwaha, C. P. K. Jayanath, M. K. Swami, A. Uppal, **H. S. Patel** and P. K. Gupta

   Proceeding of National Laser Symposium NLS22, held at Manipal University during January 8-11, 2014.

List of figures

List of tables

Chapter 1

Introduction

Rapid advancement in the field of nanotechnology has fuelled growth in the development of new techniques for fabrication, assembly and characterization of materials having nanometer scale dimensions. Research is warranted to explore newer tools having the ability to resolve objects at the nanometre scale. These should also be non-destructive, non-contact, user friendly and also capable of providing high throughput measurements with minimal sample preparation [1]. However, as one would expect it is nearly impossible to develop a method that will meet all these requirements in a single platform. This has prompted development of specialized advanced tools such as scanning electron microscopes (SEM & TEM), scanning probe microscopes (SPM), small-angle neutron scattering, X-ray scattering and absorption techniques, near field scanning optical microscope (NSOM) and structured-illumination microscopy etc. that allow visualization and quantitative characterization of structures as well as composition of materials at nanometre length scale. Among these, the devices that use optical methods allow probing nano-materials in noncontact and non-invasive manner and often require minimal sample preparation for measurement thereby preserving the native shape, size and composition. Other commonly employed optical techniques for characterization of nano-materials include dynamic light scattering, spectroscopic measurement of absorbance and/or transmittance, photoluminescence and Raman spectroscopy to infer about their average size and composition in colloidal suspensions or thin layer of nanostructures deposited or grown on a suitable substrate. However, using the conventional optical systems the ultimate resolution achievable is limited by the diffraction criteria. The resolution criterion is expressed in number of ways that differ only by the multiplication factor. The most common expression used in literature is:

$$d = \frac{0.61\lambda}{NA} \tag{1.1}$$

where λ and NA are wavelength of light and the numerical aperture of the objective lens respectively. The NA is related to the refractive index of the medium 'n' and cone angle 'θ' of the objective lens as

$$\mathrm{NA} = n \sin\theta \tag{1.2}$$

The requirement of high resolution imaging and high throughput processing of smaller feature size in nano-fabrication has led to tremendous efforts in developing techniques for circumventing the problem due to diffraction limit [2]. A number of far-field microscopy techniques have been developed that allow super-resolution imaging beyond the diffraction limit [3]. These include stimulated emission depletion microscopy [4], photo-activated localization microscopy [5], stochastic optical reconstruction microscopy [6] and the structured-illumination microscopy (SIM) [7] etc. However, these techniques require use of a suitable fluorescent labels with stringent characteristics to achieve the super resolution imaging. Near-field optics that deals with the non-propagating evanescent field that exists in the immediate vicinity of an object at distances less than a single wavelength of illumination light provides an alternative approach to achieve resolution much smaller than the wavelength. The near-field scanning optical microscope (NSOM) that uses optical near-field for the imaging and spectroscopy has emerged as one of the important optical tool for characterization of features having deep sub-wavelength dimensions [1]. One of the main problems in such near-field optical tools, however, is that the signal intensity in the near field is extremely weak. This is because of the fact that the tapered fibre probe or a hollow cantilever type probe used in a conventional NSOM for localizing the illumination to sub-diffraction spot has extremely low throughput that decreases rapidly with the decrease in aperture size [8]. Throughput of these probe for visible light illumination is ~ 10^{-4}, thus from 1 mW input power which is the typical power handling capacity of these probes one can expect to get only ~ 100 nW power at the tip apex. While it may be sufficient for high resolution imaging and near field photoluminescence measurements, many applications like near field Raman scattering, high density optical recording of data and nanolithography etc. require higher power at the sample. Further, the tightly confined field at sub-wavelength spot size is often associated with rapidly diverging beam as one move away from the focal spot. This has prompted researchers to develop alternative approaches to alleviate these problems associated with near field signal. One approach that has received considerable attention in the past decade is the use of photonic nanojet (PNJ) for generating highly confined electromagnetic field on the sub-wavelength scale. A PNJ is generated when a lossless dielectric micro-particle of appropriate size and refractive index is illuminated with electromagnetic wave. The term photonic nanojet was first used by Chen et al. [9] in 2004 to describe the results of numerical simulation of the electromagnetic field in and around the micrometre sized cylindrical dielectric object subjected to a plane wave illumination. Since then, objects of a variety of shapes, different sizes, and refractive indices have been explored for generating PNJ of desired characteristics. The first experimental evidence of the PNJ came from the study of Kong et al. [10], wherein reading of the data from sub-wavelength sized pits was demonstrated using nanojet of microwaves radiation. It was followed by experimental observation of PNJ generated by dielectric microsphere under visible light illumination using confocal imaging by Ferrand et al. [11]. Unlike the whispering gallery modes, generation of PNJ is not a resonance phenomenon and has been shown to be relatively insensitive to the deformation and surface corrugations [12], [13]. It is therefore possible to generate PNJ using micro-particles of varying sizes and wide range of illumination wavelength, provided the relative refractive index contrast between the micro-particle and the surrounding medium is approximately less than 2:1 [14]. Because of their ability to confine the light in sub-wavelength spatial dimension PNJ is rapidly emerging as a simple and cost effective approach for localized illumination/collection of scattered light with rich near field information for high resolution imaging and spectroscopy [15-19]. In the following sections we discuss the interaction of electromagnetic waves with dielectric microscopic objects and analytical approach for computing field distribution in PNJ generated by simple dielectric objects like microsphere and cylinder. Current state of the art of generation, manipulation and use of PNJ for various nano-photonic applications is discussed in the next chapter. The objective of the thesis and work carried out on use of PNJ in near field imaging and spectroscopy will be summarized.

1.1 Scattering of light by microscopic dielectric spheres

The field of light scattering has been the subject of scientific pursuit for centuries. Scattering of light by small particles having size much smaller than the wavelength of light ($a \ll \lambda$) was first investigated by Lord Rayleigh. Due to the small size of scatterers, phase of the electromagnetic field across the scatterer can be treated as constant.

Therefore, the light scattered by all the induced dipoles in the particle adds up in phase and give rise to a dipole like scattering pattern with symmetric angular distribution along the dipole axis independent of the azimuthal angle. The scattering intensity, is inversely

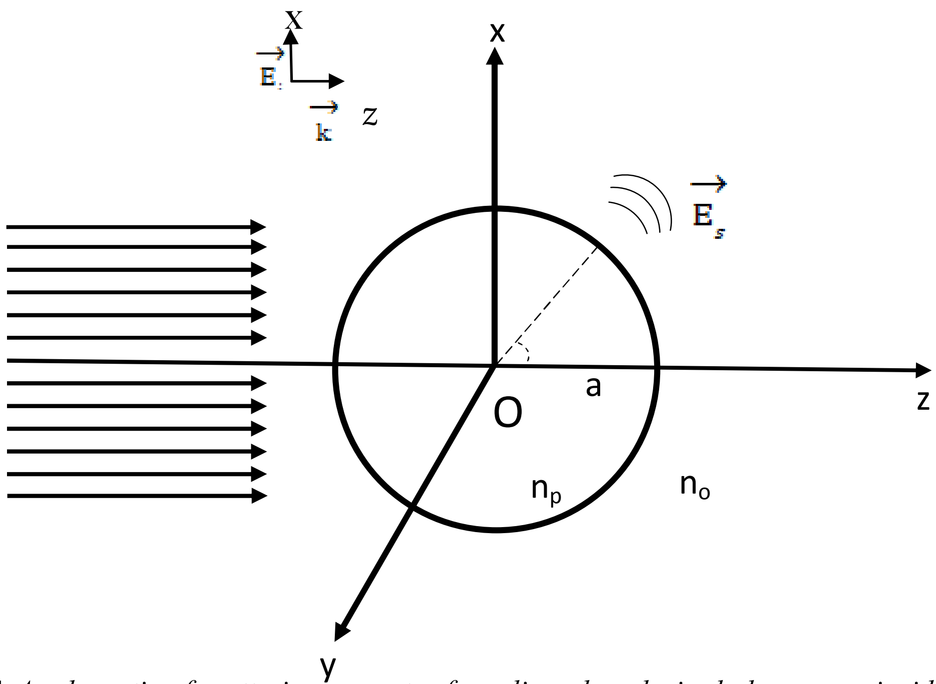

Figure 1-1 *A schematic of scattering geometry for a linearly polarized plane wave incident on a spherical particle of radius 'a'.*

proportional to the fourth power of the wavelength. For larger size scatterers (a >λ), light scattered by all the induced dipoles in the scatterer do not add up in phase except only in the forward direction making the angular distribution of the scattered light peak in the forward direction. The full description of light scattering by dielectric spherical particle in this size range was obtained by Mie in 1908, and it is known as Mie theory [20]. For a transparent dielectric particle (lossless particle) the scattering of light depends on the refractive index 'n_p' of the particle, refractive index 'n_o' of the surrounding medium and the size parameter defined as $x = 2\pi a/\lambda_m$. Here λ_m is the wavelength of light in surrounding medium. Detail description of the Mie theory is available in references [20]

[21-24], here we will only present a brief overview of the approach followed by Bohren and Huffman [22] in deriving the quantity of interest from the viewpoint of studying photonic nanojet.

Assuming a plane wave propagating along the z axis with electric field vibrations along the x axis (Figure 1.1), the electromagnetic field (**E, H**) of the monochromatic wave incident on a linear, isotropic, homogeneous sphere of radius ‘a’ satisfies the vector wave equations given by:

$$\nabla^2\boldsymbol{E} + k^2\boldsymbol{E} = 0, \qquad \nabla^2\boldsymbol{H} + k^2\boldsymbol{H} = 0 \tag{1.3}$$

where $k^2 = \omega^2\varepsilon\mu$, with ω being the frequency and ε and μ are the dielectric permittivity and permeability of the medium respectively. At the interface between the surrounding medium and the sphere the electric and magnetic fields satisfy following boundary conditions:

$$(E_i + E_s - E_1) \times \hat{e}_r = 0, \;\; (H_i + H_s - H_1) \times \hat{e}_r = 0 \tag{1.4}$$

where electric and magnetic field with subscripts ‘i’, ‘s’ and ‘1’ represent the incident field, scattered field and field inside the microsphere. In the most general form the Mie theory starts with expressing the electric and magnetic fields associated with incident plane wave in terms of vector spherical harmonics and Maxwell’s equations are solved subjected to the boundary conditions.

The incident, scattered and field inside the microsphere can be expressed as:

$$E_i \ = E_0 \sum_{l=1}^{\infty} i^l \frac{2l+1}{l(l+1)} (M_{olm}^1 - iN_{elm}^1) \tag{1.5}$$

$$E_s \ = \sum_{l=1}^{\infty} E_0 i^l \frac{2l+1}{l(l+1)} (ia_l N_{elm}^3 - b_l M_{olm}^3) \tag{1.6}$$

and

$$E_1 \ = \sum_{l=1}^{\infty} E_0 i^l \frac{2l+1}{l(l+1)} (c_l M_{olm}^1 - id_l N_{elm}^1) \tag{1.7}$$

where the subscripts 'o' and 'e' represent the odd and even vector spherical harmonics generating functions constructed using the Ψ_{olm} and Ψ_{elm} that satisfies the scalar wave equation in spherical polar coordinate as:

$$M_{elm} \ = \nabla \times (\boldsymbol{r}\psi_{elm}) \ and \ M_{olm} \ = \nabla \times (\boldsymbol{r}\psi_{olm}) \tag{1.8}$$

$$N_{elm} \ = \frac{\nabla \times M_{elm}}{k} \quad and \quad N_{olm} \ = \frac{\nabla \times M_{olm}}{k} \tag{1.9}$$

where

$$\psi_{elm} \ = \cos(m\phi) P_l^m(\cos\theta) z_l(kr) \tag{1.10}$$

$$\psi_{olm} \ = sin(m\phi) P_l^m(\cos\theta) z_l(kr) \tag{1.11}$$

with $z_l(kr)$ being any of the spherical Bessel function chosen appropriately to ensure the physical conditions are satisfied. For example, to meet the requirement of finite amplitude of wave function at the origin $j_l(kr)$ is used as generating function whereas $h_l^1(kr)$ is used for scattered field to correctly represent the outgoing spherical wave. These have been indicated with superscript '1' and '3' in equations (1.5-1.7). Orthogonality of the spherical harmonics requires that all expansion coefficients in these equations are identically zero except for m = 1. In the literature this fact has been used to reserve the notation 'm' to represent the relative refractive index of the sphere with respect to the surrounding medium which we will also use henceforth. The expansion coefficients for the field can be evaluated using:

$$a_l = \frac{\mathrm{m}^2 j_l(mx)[xj_l(x)]' - j_l(x)[mxj_l(mx)]'}{\mathrm{m}^2 j_l(mx)\left[xh_l^1(x)\right]' - h_l^1(x)[mxj_l(mx)]'} \tag{1.12}$$

$$b_l = \frac{j_l(mx)[xj_l(x)]' - j_l(x)[mxj_l(mx)]'}{j_l(mx)\left[xh_l^1(x)\right]' - h_l^1(x)[mxj_l(mx)]'} \tag{1.13}$$

$$c_l = \frac{j_l(x)\left[xh_l^1(x)\right]' - h_l^1(x)[xj_l(x)]'}{j_l(mx)\left[xh_l^1(x)\right]' - h_l^1(x)[mxj_l(mx)]'} \tag{1.14}$$

and $$d_l = \frac{mj_l(x)\left[xh_l^1(x)\right]' - mh_l^1(x)[xj_l(x)]'}{\mathrm{m}^2 j_l(mx)\left[xh_l^1(x)\right]' - h_l^1(x)[mxj_l(mx)]'} \tag{1.15}$$

Here prime has been used to denote first derivative. Using these coefficients it is possible to evaluate the field at any point inside or outside the microsphere. The scattering and extinction efficiency of the particle is given by:

$$Q_{sca} = \frac{2}{x^2}\sum_{l=1}^{\infty}(2l+1)\left[|a_l|^2 + |b_l|^2\right] \tag{1.16}$$

and $$Q_{ext} = \frac{2}{x^2}\sum_{l=1}^{\infty}(2l+1)\Re\{a_l + b_l\} \tag{1.17}$$

Similar analytical expression for infinite dielectric cylinders have also been worked out in the literature [21, 22].

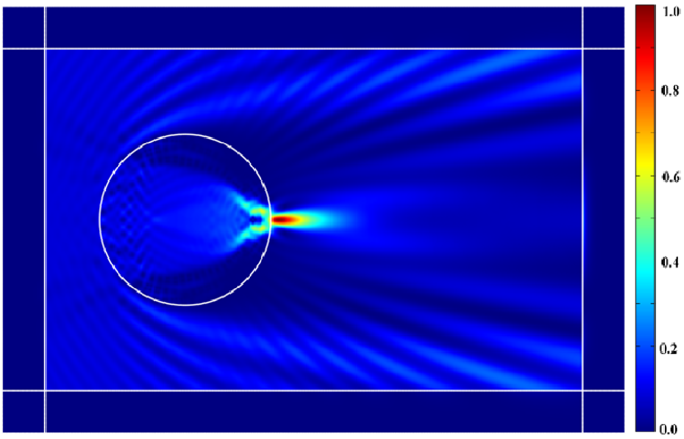

Figure 1-2 *Normalized intensity distribution in a typical photonic nanojet generated by microsphere of diameter 4 µm at incident wavelengths of 514 nm. Refractive index of the microsphere is* n_p *= 1. 45 and that of the surrounding medium is* n_o *= 1.0.*

Using the analytical results obtained from the Mie theory one can calculate the field in and around the microsphere to visualize transformation from a dipole like distribution for Rayleigh scatterer to a photonic nanojet like structure as the size of particle is gradually increased. Figure 1.2 shows the image of photonic nanojet generated by a dielectric microsphere of radius 4 µm and refractive index $n_p = 1.45$.

The scattering of light by particles of larger size when compared to the illuminating wavelength (r>> λ) are explained by ray tracing using the geometric scattering theories. It can be shown using Snell's law that under the thick lens approximation, the focus for a microsphere having radius 'a' placed in air is located at [25]

$$f = \frac{a}{2}\left(\frac{n_p}{n_p - 1}\right) \tag{1.19}$$

from the microsphere centre. It can be seen from the above expression that for refractive index $1 < n_p < 2$, the focus is located out of the microsphere on the shadow side. However, for $n_p = 2$, the focus point moves onto the surface of microsphere and inside the microsphere for $n_p > 2$ .The spot size at the focus position can be approximated by

$$w = a\sqrt{\frac{\left(4-n_p^2\right)^3}{27n_p^3}} \tag{1.20}$$

and the intensity of the field at the focal point with respect to the incident field intercepted by the microsphere is given by

$$\frac{I_{max}}{I_0} \approx \frac{a^2}{w^2} = \frac{27n_p^3}{\left(4-n_p^2\right)^3} \tag{1.21}$$

Similar expression for infinite cylinder of radius 'a' has been derived to obtain the enhancement of field which is given by [25]

$$\frac{I_{max}}{I_0} \approx \sqrt{\frac{27n_p^3}{\left(4-n_p^2\right)^3}} \tag{1.22}$$

1.2 Photonic nanojet

Photonic nanojet is the intense sub-wavelength confinement of the electromagnetic field due to near field focusing by dielectric microsphere. Though the field inside the microsphere illuminated by the plane wave was computed by number of researchers and the enhancement of the field was observed earlier [26-33], the term "photonic nanojet" was first introduced by Chen et al [9] to describe the phenomenon. Since then, important parameters of the photonic nanojet have been investigated both theoretically as well as experimentally to gain physical insight of the phenomena for controlling the characteristics of nanojet.

1.2.1 Photonic nanojet characteristics

The photonic nanojet with significant near field contribution show exquisite characteristics that enable potentially important applications covering a vast area of photonics including detection of nano-particles via enhanced back scattering, manipulation of nano-scale objects, optical data storage, mask less nano-patterning and nanolithography, single molecule detection, remote optical addressing with low loss and super-resolution imaging etc. The characteristics of PNJ generated by a micro-particle are governed by the optical properties and geometry of the particle, surrounding environment and illumination wavelength. Key parameters of PNJ that determine the choice of micro-particles for these applications are focal distance, jet length, jet width, peak intensity and the working distance etc. Figure 1.3 shows a pictorial depiction of these parameters for a typical PNJ. The length of a PNJ is defined as the distance from the edge of the sphere to a point along the optic axis where the intensity drops to twice that of the incident light. Typically with a homogeneous microsphere geometry PNJ length of ~ 3 λ can be realized. Further increase in the length has been demonstrated by immersing the microsphere in a liquid environment [34], using microsphere with concentric or axially eccentric shells of graded refractive indices [35-36] and via shaping of the incident wavefront [37]. However, it is important to note here that the longer PNJ are often accompanied with poor lateral confinement and reduced peak intensity. The width of a PNJ is defined as full width at half maxima (FWHM) of the transverse intensity profile measured at highest intensity along the optic axis. Typical width of PNJ is ~ 0.5 λ for microspheres having refractive index of 1.45 (Figure 1.3).

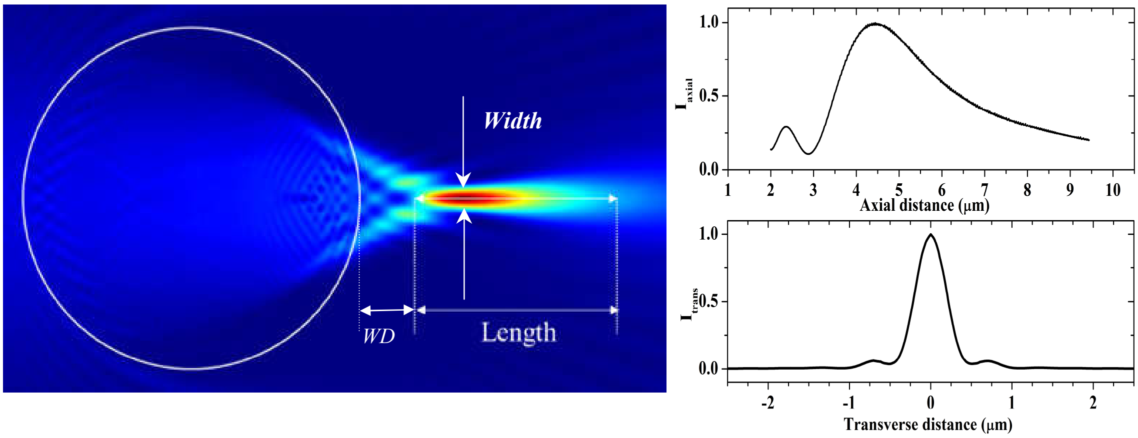

Figure 1-3 *Pictorial depiction of photonic nanojet parameters (left) and longitudinal and transverse intensity profile in PNJ (right).*

The width of PNJ depends strongly on the refractive index of the micro-particles and reduces with increase in the refractive index till its refractive index contrast with the surrounding is less than 2. Further increase in the refractive index of particle leads to focusing of light inside the micro-particle. It is for this reason that both the width and the length of a PNJ are measured at the point lying outside the shadow surface of micro-particle that generates the nanojet. The peak intensity of a PNJ is generally expressed in terms of the normalized intensity at the maxima in axial intensity profile of the PNJ with respect to the incident beam intensity and hence denotes enhancement in the intensity due to localization of field in the nanojet. The working distance of a PNJ is another parameter that plays an important role in enabling examination of samples through thicker interfaces such as nano-particles migrating inside the biological cell. The working distance of a PNJ is defined as the distance from micro-particle surface to the maximum intensity point in a PNJ from on shadow side of the particle.

1.2.2 Photonic nanojet applications

Owing to sub-wavelength confinement of light, PNJs have been explored for many interesting applications. In this subsection we will discuss some of the important applications of PNJ reported till date.

1.2.2.1 Detection and localization of nanoparticle

In the original article on PNJ, Chen et al [9] theoretically demonstrated that the nano-particles moving in the transverse direction through the field of nanojet lead to a significant enhancement in backscattering of light. This was utilized by Heifetz et al to experimentally demonstrate detection and localization of a 20-nm diameter gold nano-particle with a sub-diffraction transverse spatial resolution [38]. Theoretical simulation using perturbation approach show that gold nano-particles as small as 2 nm in diameter produce sufficient backscattering enhancement (~ 34 dB) compared to microsphere alone. The backscattering signal was found to increase linearly over a wide range of diameter (2 - 60 nm) of interest. The backscattered power for smaller sized nano-particles has been found to be proportional to the volume of nano-particle in contrast to the volume square dependence that is expected for Rayleigh scattering. This has a potential bio-photonics application in detection of nano-particles attached to the membrane of living cells in an aqueous environment.

1.2.2.2 Enhancement of Raman scattering

High local intensity in the photonic nanojets generated by dielectric microsphere has been used experimentally by several groups to enhance the Raman signal from different substrates. An order of magnitude intense Raman signal was reported by making use of self-assembled silica and polystyrene microspheres on silicon substrate [39, 40]. Apart from being a cost effective approach PNJ assisted enhancement of Raman signal can also be coupled with other approaches like coherent anti-stokes Raman scattering (CARS) and surface enhanced Raman scattering (SERS) etc. for a synergistic enhancement of signal. Chang et al. [41] have reported Raman enhancement factor of ~ 3.6×10^{10} by making use of photonic nanojet assisted Marangoni convection to increase the turnover of analytes in SERS hotspots in liquid environment. The combined PNJ-SERS based Raman spectroscopy may therefore be a potentially useful approach for alleviating the problems associated with reproducibility of signal in SERS.

1.2.2.3 Ultrahigh density optical data storage

Heat-assisted magnetic recording is capable of writing data in excess of 1 Tb/in^2 density by temporarily heating the area of a single bit on the hard disk to its Curie temperature using a near field transducer. Challenar et al have explored use of PNJ for coupling of light into the near field transducer [42]. While the theoretical simulation show that nanojet-illuminated pits having lateral dimensions of only 50 nm×80 nm can give up to 27 dB better contrast than using a conventional lens based system, experimental results on scaled up model show that high density optical storage with individual bit stored in ~ $0.025\lambda^2$, can be robustly detected. To put this perspective it should be noted here that the current commercial Blu-Ray disks have pit size of about $\lambda/4$ and track pitch of $\lambda/1.25$.

1.2.2.4 Maskless nano-patterning and nanolithography

PNJ generated by self-assembled planar structure of silica microsphere upon illumination with a 400 nm centred ultraviolet (UV) broad band light source was used successfully by Wu et al. [43] to demonstrate mask-less lithography with a feature size down to 250 nm. Mask-less lithography using microsphere allows nano-writing even at lower fluence and provides better control of the hole or pillar diameter by varying the exposure time. McLeod and Arnold [44] have shown nano-lithography using photonic nano jet generated by optically trapped sub-micron size polystyrene microspheres. Microsphere was trapped using 532 nm continuous-wave laser Bessel beam and simultaneously illuminated with a 355 nm pulsed Gaussian beam to generate the nanojet which was used for writing on the substrate. A resolution of 102 nm (~λ/3.5) and 130 nm (~λ/2.7), was achieved using the optically trapped microsphere of 0.5 μm and 0.8 μm sized polystyrene microspheres.

1.2.2.5 Near field trapping and manipulation of nanoparticles

Optical forces on metallic nano-particles induced by a photonic nanojet was first calculated by Cui et al to demonstrate stable trapping of metallic sub-wavelength nano-particle using the optical forces acting on it in the electromagnetic field of PNJ. Force acting on the particles was shown to be sensitive to polarization and reverses the sign upon changing polarization. Optical forces on dielectric particles near sub-wavelength slits illuminated by a PNJ have been investigated by Valdivia-Valero et al. [45]. Numerical simulation have also been carried out to show that the hook shaped curve nanojet generated by asymmetric micro cuboids can be used for nano-particle manipulation along a specific path thereby allowing better manoeuvring of particles around the obstacles [46]. The exquisite control over the particle's motion offered by photonic hook may enable sorting and manipulation of particle in micro-fluidic devices and 'lab-on-a-chip' platforms without the need for multiple trapping beam. On the experimental front trapping and manipulation of nano-particles using the standing wave formed by two counter propagating photonic nanojet was demonstrated by Wang et al [47]. More recently, trapping of cells and macromolecules has also been reported using photonic nanojet array.

1.2.2.6 Low loss optical waveguide

Remote addressing of the optical nano-devices is important for selective and high throughput delivery of signal at desired port. Photonic nanojet induced modes in chain of optical microsphere has been shown to be an experimentally efficient approach for low loss (< 0.08 dB/ microsphere) delivery of visible light at exit point of the microsphere chain [48]. PNJ induced coupling offers significant advantages over the commonly used coupling technique based on whispering gallery mode. This is because the formation of nanojet is a non-resonant phenomenon and has been shown to be relatively insensitive to the deformation and surface corrugations in the microspheres. Therefore, polydispersity in the microsphere diameter do not adversely affect the waveguiding characteristics.

1.2.2.7 Super-resolution optical imaging

The ability to confine electromagnetic field to sub-diffraction spot size makes the photonic nanojet a good candidate for collecting information from confined region of sub-wavelength size. This follows the principle of reciprocity consideration which states that reverse process of collecting optical information from sub-diffraction region should also be possible by just time reversal. It is therefore expected that microsphere can help relay the near-fields in a similar way as in collection mode NSOM to break the diffraction limit. Indeed the microsphere based nanoscopy has been demonstrated to achieve deep sub-wavelength resolution down to ~ $\lambda/17$ [15-16]. Hao et al. [49] were first to demonstrate wide field super resolution imaging using microspheres. Super resolution imaging with microspheres has also been demonstrated in aqueous environments suitable for imaging of biological samples using high refractive index microsphere. The choice of microsphere refractive index is guided by the fact that increase in refractive index of background liquid medium causes the nanojet peak to shift in the far field and needs to be compensated for bringing it closer to the surface for effectively relaying the high spatial frequency information. Imaging of sub-cellular structures in biological samples, like centrioles, mitochondria and chromosomes etc. [50] and single adenovirus [51] have also been demonstrated using microsphere nanoscope. While the microsphere nanoscopy provides wide field image of the features under the microsphere, it is desirable for many practical applications to precisely control the positioning of microspheres over the sample. Krivitsky et al. [16] demonstrated that attaching a glass micropipette near equatorial plane of microsphere has minimal effect on its PNJ characteristics and used it for moving the particle to perform scanning over the sample area. It was followed by successful demonstration of super resolution imaging by using a microsphere mounted on

AFM cantilever for precise scanning over the sample [15, 52]. Since the generation of nanojet is a non-resonance phenomenon, microsphere nanoscopy can also be performed using white light. Detailed evaluation of the performance of microsphere nanoscopy vis-à-vis solid immersion lens and confocal microscopy has been carried out by Darafsheh et al. [53]. More recently, assembly of 3D cluster of meta-materials have been proposed for generating periodic near field nanojet that may find applications in nanoscopy and nano-patterning with resolution down to ~ 15-30 nm [54].

1.2.2.8 Single molecule spectroscopy

Fluorescence correlation spectroscopy (FCS) is one of the most powerful single molecule detection techniques for analysis of molecules at extremely low concentration. However, the basic principle of FCS requires that the concentration of molecules and the excitation volumes should be such that only few molecules are simultaneously present in the focal volume. This requires a complicated optical instrumentation which is limited by diffraction criteria as far as the detection volume is concerned. PNJ generated by dielectric microspheres under focused Gaussian illumination were used by Wagnear et al [17, 18], to achieve optical confinement of the detection volume below the diffraction limit. While the reduced observation volume allows measurements at significantly higher concentration, using planner array of microsphere it is also possible to create multi-focus FCS with photonic nanojets arrays to enable single molecule sensitivity at pico-molar concentration. More recently PNJ has also been coupled with surface enhanced Raman spectroscopy (SERS) to utilize Marangoni convection set in by the nanojet to enhance the turnover of analytes into the hotspot region [41]. This approach allows detection and chemical analysis of the analytes with a single molecule sensitivity and nanometer scale spatial resolution in a label free manner.

1.3 Summary and scope of the thesis

The present thesis deals with investigation of the generation, manipulation and use of PNJ from dielectric microsphere illuminated with visible light. In Chapter 2 we provide details of the computational tools for solving problem of electromagnetic scattering by arbitrary shaped objects with particular emphasis on the finite element method based approach and the discrete dipole approximation which has been used for the numerical simulations presented in this work. Details of the experimental setup used for performing the measurements presented in the thesis have also been described. Generating PNJ of desired characteristics is of paramount importance for various applications. Different approaches investigated for manipulating PNJ characteristics have been presented in Chapter 3. The results of these studies show that axially offset core shell microsphere can be used for tuning PNJ characteristics over wide range, covering extremely narrow (FWHM ~ $\lambda/4.5$) to highly elongated (length ~27λ) photonic nanojet. It was also demonstrated that by using off axis illumination with a tightly focused beam it is possible to achieve angular tuning of PNJ emission. In Chapter 4 we discuss the use of PNJ for enhancing the transmission through nano-aperture tip used in near field imaging. It was experimentally demonstrated that throughput of a pyramid shaped hollow cantilever probe can be increased by an order of magnitude using PNJ generated by microsphere inserted in the probe. The enhanced throughput of the near field probe allows coupling of light at several wavelengths without crossing the damage threshold. This not only allows spectral near field imaging of the sample but also enables measurement of polarization properties of the nano structure by suitably varying the polarization state of different wavelengths. In Chapter 5 details of the experimental scheme developed to achieve simultaneous spectral and polarization sensitive near field imaging have been presented. Chapter 6 covers the application of PNJ for enhancement of Raman signal from different substrate materials of varying refractive index. The experimental data presented in the chapter show that the degree of enhancement is strongly dependent on relative refractive index contrast (RIC) between the microsphere and the substrate. While an order of magnitude enhancement in Raman signal is common for substrate having high RIC, the enhancement factor drastically reduces with decrease in RIC. An approach based on decoupled excitation and collection path has been shown to achieve a better enhancement from sample with lower RIC.

Chapter 7 provides summary of the important results presented in this thesis. The thesis concludes with a discussion on possible future work that might improve and advance the techniques presented in this thesis.

Chapter 2

Theory and experimental details

In this chapter we provide an overview of the techniques commonly employed for solving the Maxwell equations for objects with arbitrary shape and refractive index profile. Particular attention is paid to the discrete dipole approximation (DDA) and finite-element method (FEM) based approach for computing the field distribution in (Photonic Nano-Jet) PNJ generated by dielectric micro-particles because these have been extensively used for the work reported in this thesis. Details of the near field scanning optical microscope used for performing the measurements presented in the thesis are also discussed in this chapter.

2.1 Numerical solution of Maxwell's equation in light scattering

Analytical solutions for scattering of electromagnetic waves by dielectric objects are available only for objects having simple geometries like spheres, infinite circular cylinders, spheroids and coated spheres etc. However, for particles with complex geometrical shape or refractive index distribution it becomes very difficult to keep track of and impose boundary conditions at the particle surface and interfaces. This has led to the development of numerical approaches for solving electromagnetic scattering problems involving complicated geometries. Most prominent among these include T-matrix method [55], the method of moments [56] the discrete-dipole approximation [57-59] the finite difference time domain method, the integral equation technique and the finite element method [60, 61]. A vast variety of these methods based either on differential formulation or an integro-differential formalism use partitioning of the region occupied by the scatterer into may sub-regions [62]. Among these the Finite Difference Time Domain Method (FDTD) is the most popular technique for solving the partial differential equations because of ease with which numerical difference equations can be formulated over regular grids. However, due to regular shape of grids (square/cubic element in 2D/3D) used in FDTD, it requires extremely large number of elements to capture the details of object with sharp or irregular feature particularly in handling the curved boundaries for the purpose of defining the boundary conditions. The FEM on the other hand is most flexible in terms of handling complex geometry and boundary conditions at the curved interfaces. In the present work we have used DDA based open source software DDSCAT 7.1 and finite element method (FEM) based software package COMSOL® Multiphysics 4.2 for solving the Maxwell's equation. Conceptual basis of these two approaches are presented in the following section.

2.2 Discrete dipole approximation

The discrete dipole approximation (DDA) sometimes also referred to as coupled dipole method is powerful tool for modelling light scattering by objects of arbitrary geometrical shape. In the discrete dipole approximation the scatterer is represented as a collection of point dipole each of which interacts with the field of incident electromagnetic wave and the field induced by neighbouring dipoles to give rise to the scattered field. Since each dipole in the collection can be assigned dipole moment independent of others the DDA can also be used for modelling inhomogeneous as well as anisotropic scatterers. The method of DDA was first proposed by Purcell and Pennypacker [57] and developed for wide variety of scatterers by Draine and Flatau [58]. Applicability of DDA was further extended by including the magnetic dipole terms [63], surface interaction terms [64] and periodic dielectric structures [65].

Let us consider a dielectric scatterer represented by a collection of N dipoles. The dipole ‘j’ located at the coordinate r_j with reference to the origin experiences electric field $E_{loc,\,j}$ which is sum of the field due to the incident wave $E_{inc,\,j}$ and the contributions from remaining dipoles.

$$E_{loc,j} = E_{inc,j} + \sum_{\substack{n=1 \\ n\neq j}}^{N} E_n \tag{1}$$

For a time harmonic incident plane wave

$$E_{inc,j} = E_0 e^{i(kr_j - \omega t)} \tag{2}$$

and

$$E_n = -A_{jn} P_n \tag{3}$$

where A_{jn} represents the interaction term between dipole pair ‘j’ and ‘n’ and is given by

$$A_{jn} = \frac{e^{ikr_{jn}}}{r_{jn}} \left[k^2 \left(\hat{r}_{jn}\hat{r}_{jn} - \mathrm{I} \right) + \frac{ikr_{jn}-1}{r_{jn}^2} \left(3\hat{r}_{jn}\hat{r}_{jn} - \mathrm{I} \right) \right]_{j\neq n} \tag{4}$$

In response to the local electric field each dipole in the array representing scatterer acquires an induced dipole moment

$$P_j = \alpha_j E_{loc,j} \tag{5}$$

Where α_j is polarizability of the material associated with the dipole element. Therefore, local electric field can be expressed in terms of polarizability as

$$E_{loc,j} = \alpha_j^{-1} P_j \tag{6}$$

Defining the diagonal interaction matrix terms as $A_{jj} = \alpha_j^{-1}$ and substituting eq. (3) and (4) in eq. (1) we can write

$$E_{inc,j} = A_{jj} P_j + \sum_{\substack{n=1 \\ n \neq j}}^{N} A_{jn} P_n \tag{7}$$

Solving this set of 3N linear equation unknown dipole moments P_j can be computed numerically. The scattered field, Poynting vector, Mueller matrix, scattering cross section and phase function etc. can be calculated using the knowledge of dipole moment.

2.2.1 Applicability of DDA

In a standard DDA computation the dipoles representing the scatterer are placed in regular cubic lattice (Figure 2.1). Statistical analysis of the computation results show DDA calculation for standard objects like microsphere and infinite cylinders match with the analytical solutions provided the inter-dipole separation 'd' is small compared to (i) smallest structural feature in the scatterer and (ii) the excitation wavelength 'λ'.The latter criteria has been shown to be satisfied [58] if the inter dipole distance is such that

$$d \leq \frac{1}{k|m|} \tag{8}$$

where 'm' is relative refractive index of the scatterer with respect to surrounding and κ is wave vector.

The practical limit on scatterer size depends on various parameters including the value of the dielectric function, the detailed target shape and the "dimensionality" of the problem. For isolated targets, practical consideration on requirement of memory and run time limits the size parameter of the scatterer to ~20. The number of dipoles ‘N’ required to represent the scatterer and the inter dipole spacing ‘d’ are related by the volume of scatterer as:

$$Nd^3 = \frac{4}{3}\pi a^3 \tag{8}$$

The effective radius of the equivalent spherical scatterer is thus given by

$$a = d\left(\frac{3N}{4\pi}\right)^{1/3} \tag{8}$$

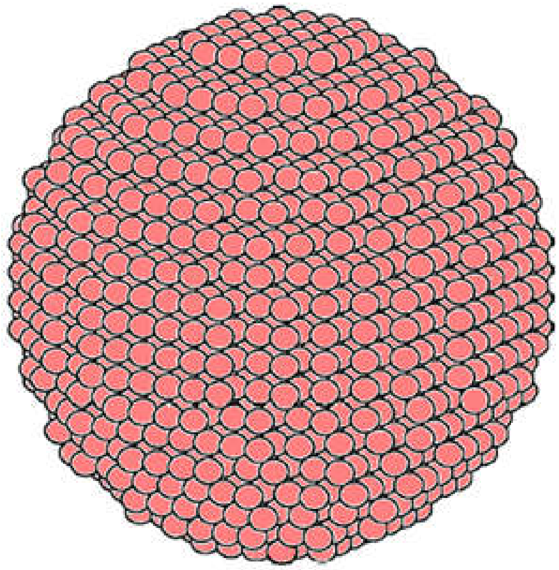

Figure 2-1 *A typical sphere represented by dipoles arranged in regular cubic lattice [adapted from Ref. 58].*

2.2.2 DDSCAT code based on DDA

DDSCAT is an open-source code based on the discrete dipole approximation to compute the optical response of scatterers. It is implemented using Fortran 90 and the version DDSCAT 7.1 has been used for simulating the field in and around the microspheres. The main program in DDSCAT 7.1 computes the dipole moments P_j at each dipole coordinate by solving the system of linear equations (7). It is equipped with variety of options to choose from, for solving the matrix equations in efficient manner. Routine for generating dipole distribution and input parameters for target geometry and compositions and post processing of the near field electric and magnetic field data from the output file are also one among the important pre- and post-processing tools available with DDSCAT. A typical input parameter file and the output file generated by the DDSCAT 7.1 are given in Appendix A

While the DDA works well for computing far-field scattering properties of arbitrarily shaped particles, accurate modelling of the near-field requires exceedingly large number of dipoles making the memory requirement and computation time prohibitively high [62].

2.3 Finite-Element Method

The finite-element method (FEM) is used for solving partial differential equations within a finite space that contains an object of arbitrary geometry and composition. In a typical FEM formulation the entire domain of interest is divided into sub domains in which local solution is expressed in terms of suitable basis function and unknown coefficients. By applying method of Galerkin’s or Ritz variational approach a system of algebraic equations is obtained which can be solved to obtain the solution of differential equation. The FEM based approach can therefore be decomposed in four steps (i) discretization of the domain (ii) selection of basis function (iii) assembly of system of linear equations and (iv) solution of the system of equations [66]. In the following paragraph we will present a brief conceptual basis of FEM formulation.

Let us consider a general form of differential equation defined over domain Ω together with the associated boundary conditions on the domain boundary

$$\mathcal{L}\phi = f \tag{9}$$

Here $\mathcal{L}$ is differential operator, 'f' is reinforcing term and 'ϕ' is the desired solution. If the

operator $\mathcal{L}$ is self adjoint and positive definite then the solution to the equation (2.9) can be obtained by minimizing the functional [66]

$$F(\tilde{\phi}) = \frac{1}{2}\langle \mathcal{L}\tilde{\phi}, \tilde{\phi}\rangle - \langle f, \tilde{\phi}\rangle \tag{10}$$

where $\tilde{\phi}$ is trial solution and angular bracket denotes the inner product. If the trial solution is constructed using linear combination of the local solution in individual elements in the discretised domain than $\tilde{\phi}$ can be written as

$$\tilde{\phi} = \sum_{j=1}^{N} N_j \phi_j \tag{11}$$

where N is the total number of nodes in the computational domain. Substituting the value of $\tilde{\phi}$ from eq. (11) in eq. (10) and taking the derivative with respect to nodal variable ϕ_j one gets:

$$\frac{\partial F(\tilde{\phi})}{\partial \phi_i} = \sum_{j=1}^{N} \phi_j \langle \mathcal{L}N_j, N_i\rangle - \langle f, N_i\rangle \tag{12}$$

The desired solution of the differential equation is obtained by demanding this derivative to be zero. Thus, finding the solution of differential equation using FEM formulation eventually reduces to solving the set of linear equations

$$[K]\{\phi\} = \{b\} \tag{13}$$

where $$K_{ij} = \langle \mathcal{L}N_j, N_i \rangle \tag{14}$$

and $$b_i = \langle f, N_i \rangle \tag{15}$$

To compute the field distribution in PNJ generated by dielectric micro particles Maxwell's wave equation is solved. The general form of the vector wave equation is given by:

$$\nabla \times (\nabla \times \boldsymbol{E}) - k^2\boldsymbol{E} = -i\omega\mu\boldsymbol{J} \tag{16}$$

and $$\nabla \times (\nabla \times \boldsymbol{H}) - k^2\boldsymbol{H} = \nabla \times \boldsymbol{J} \tag{17}$$

at the interface between microsphere and the surrounding medium the electromagnetic field satisfies the continuity conditions which are defined as:

$$\hat{n} \times (E_2 - E_1) = 0 \tag{18}$$

$$\hat{n}.(D_2 - D_1) = 0 \tag{19}$$

$$\hat{n} \times (H_2 - H_1) = 0 \tag{20}$$

$$\hat{n}.(B_2 - B_1) = 0 \tag{21}$$

where subscripts '2' and '1' denote the microsphere and the surrounding medium and $\hat{n}$ is outward normal unit vector from microsphere surface.

In order to obtain physical solution for scattering by an isolated micro-particles which we deal with extensively in this thesis, it is necessary for the electric and magnetic field components to satisfy Sommerfeld radiation condition i.e.

$$\lim_{r\to\infty} r(\boldsymbol{\nabla} \times \boldsymbol{E} + ik_0\hat{\boldsymbol{r}} \times \boldsymbol{E}) = 0 \tag{22}$$

In practice it is not possible to solve the Maxwell's equation over the entire domain because of computational limitation. Therefore, simulation domain is restricted within a boundary that is sufficiently (of the order of several wavelengths) away from the scatterer. The truncated computational domain however leads to significant artifacts in the simulation results, because of reflections from the boundaries. One of the most common approaches followed in computational electrodynamics to avoid this problem is to use perfectly matched layers (PML) that absorb all outgoing wave striking domain boundaries at arbitrary angle and polarization without any reflection [67].

We have used commercial software package COMSOL® MultiPhysics 4.2 [68], which makes use of the finite element method. The Multiphysics module has several built-in sub modules like transverse electric, transverse magnetic and hybrid wave propagation, scattered harmonic propagation, Eigen frequency modes etc. can be used to solve the Maxwell's equations for computing optical response of the system with arbitrary geometrical shape and wide range of dielectric properties. The basic steps involved in solving the scattering problem are to define the simulation geometry, meshing of the computational domain into smaller elements, defining the physical parameters of the particles and surrounding and solving the Maxwell's equations on each mesh element. Since most of the geometries considered in this thesis involve axi-symmetric problems which are a 3D problem with no azimuthal angle dependence we used the geometry tool of COMSOL to draw the object and simulation region though it is possible to import geometry details from variety of other standard CAD tools. Figure 2.2 shows a schematic of computational domain and mesh structure for 2D simulation of nanojet generated by a dielectric microsphere. More details about the modelling steps involved in 3D simulation is given Appendix B.

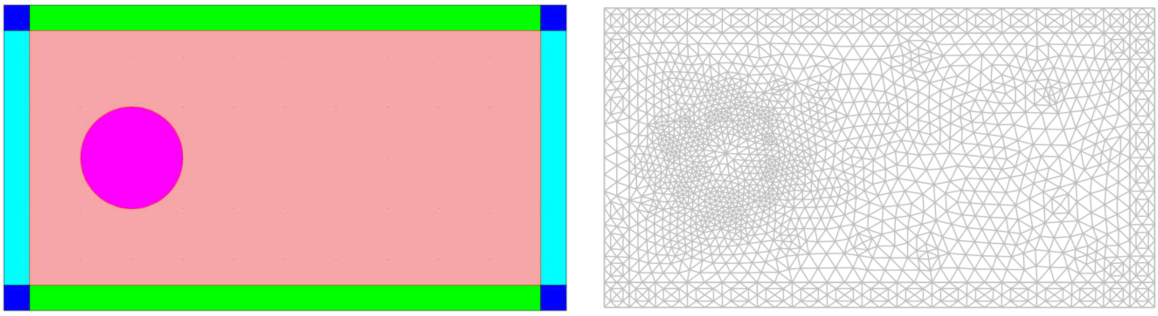

Figure 2-2 *Schematic representation of 2D computational domain (left) and a typical mesh structure (right) for simulating photonic nanojet by dielectric microsphere.*

COMSOL is capable of handling objects with arbitrary geometries, and hence can simulate particle agglomerates well as layered particles [69] However, for particles with sharp features or regions of high curvature, requirement of finer mesh leads to increased memory requirement and computation time. One of the most important benefits that FEM offers as compared to other numerical techniques is that the mesh elements do not need to be of the same size and shape. This allows modelling of the regions of varying features sizes with variable mesh size without the need of finer mesh over entire computational domain which may lead to a prohibitively large computational cost.

Table 2-1 *Comparison of computation time, advantages and disadvantages computational techniques used to simulate the scattering of electromagnetic radiation [reproduced with permission from Ref. 62]*

Method	Computation time for Au sphere radius << λ	Advantages	Disadvantages
Mie Theory	*Rapid:* a few milliseconds per individual frequency	• Rapid computation time. • Can also be used to compute the optical response of coated spheres.	• Applicable only to spherically symmetric particles. • Not possible to include a substrate interaction.
T-Matrix	*Rapid:* a few milliseconds - per individual frequency.	• Rapid computation time. • Wide range of geometries supported. • Also possible to include a substrate interaction	• Computations are numerically unstable for elongated or flattened objects.
DDA	*Moderate:* depends on number of dipoles, and separation. Typically 50s per individual frequency.	• Can be used to evaluate any arbitrary shaped particle by specifying a tabulated list of dipole locations	• Convergence criterion: $\|m\|\ kd < 1$ prevents solving problems with high aspect ratio / elongated objects or those having a large refractive index
FEM	*Lengthy:* typically 150s per individual frequency when using an element length of 3nm. A compromise is made between the computation time and element length.	• Can be used to evaluate the scattered field-distribution of any arbitrary shaped particle. • The use of a non-regular tetrahedral adaptive mesh for the FEM simulation allows for a more accurate approximation of curved surfaces.	• Computation time is lengthy.
FDTD	*Lengthy:* a broadband response is computed across a wide frequency range, typically taking ≈ 3 hours to cover visible frequencies. A compromise is made between the computation time and element length.	• Can be used to evaluate scattering parameters from any arbitrary shaped particle.	• Computation time is lengthy. • Permittivity values have to be specified over much wider frequency range than just the range of interest. The Drude-Lorentz model may not be an accurate representation of experimental data.

This is particularly important when considering distribution of near-field components in the photonic nanojet. Table 2.1 summarizes the performance of different algorithms for computation of electromagnetic field in and around the metallic nanoparticle with personal computer having a. 2.19 GHz dual-core processor and 2 GB of RAM [62].

2.4 The experimental setup

Figure 2.3 shows a schematic of the near field scanning optical microscope Alpha300SR (Witec Instruments GmbH, Germany) system that has been used for performing measurements reported in this work. The Alpha300SR is a dual microscope based modular system that can be configured as near field scanning optical microscope (NSOM), Atomic force microscope (AFM) and confocal Raman microscope and various combinations thereof. The upright microscope that is used for sample inspection and confocal measurement has a special SPM objective holder for AFM and NSOM measurement. The SPM objective holder has provision for holding a common microscope objective and an inertial drive assembly to magnetically hold the cantilever. The objective in SPM holder is used to focus the feedback laser onto the cantilever and collect the deflected beam. It is also used for coupling the excitation light for NSOM measurements. The inverted microscope uses a fixed objective which can be positioned manually along Z direction to bring the sample in focus coarsely. Finer adjustment is done by stepped motor controlled positioning with a step size of 0.1μm in X and Y direction and 0.05μm in Z direction. A CCD camera and SMA fiber connector feed-through unit are placed in perpendicular beam paths at the image plane of inverted objective. A flip mirror allows directing the light to either CCD for viewing the sample or to a photon counting unit/spectrometer for transmission mode measurements.

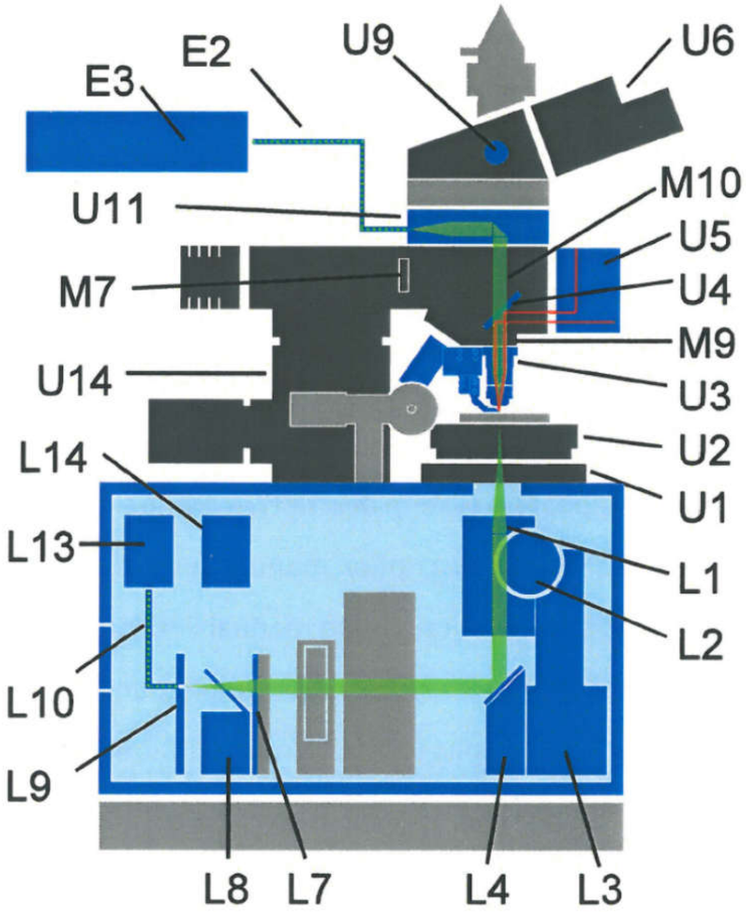

Figure 2-3 *A Schematic of experimental setup used and illustration of the beam path for near field scanning optical microscopy measurement in transmission mode. Different components of the system are Upright microscope: U1- XY positioner; U2- Piezo scanner; U3-Objective with cantilever holder; U4-dichroic mirror for feedback laser; U5-Quadrant photodiode; U6-binocular unit with colour camera; U9-flip-mirror; U11-Laser coupling unit; U14-Microscope Z stage; Lower microscope: L1-Objective holder; L2- Manual Z positioning stage; L3-motorized X,Y,Z positioner; L4-Deflection mirror; L7-Tubelens; L8 flip-mirror; L9-Pinhole with SMA adapter; L10 Multimode optical fiber; L13 Single photon counting PMT; L14 viewing camera for bottomport; M7-Luminous field diaphragm; M9-Objective Turret; M10-Bright field reflector; E2-Polarization maintaining single mode fiber for beam delivery and E3- Laser unit* [70].

2.4.1 Operating principle

At the heart of the system is AFM system built around Zeiss 1100 microscope. Atomic Force Microscopy performs high resolution imaging of the topography of samples by recording the interaction forces between the surface and a sharp tip mounted on a cantilever. Using AFM, it is possible to image ultra-structures on the surfaces with topographic resolution down to the level of molecular structures. In addition to the imaging of small topographic features AFM is also capable of imaging variety of other surface properties such as adhesion, stiffness, magnetization, conductivity etc. using different interactions between tip and the sample. The operating principle of an AFM module in Alpha300SR is schematically illustrated in figure 2.4. It makes use of cantilever type probe and optical feedback mechanism for controlling the separation between probe and the sample.

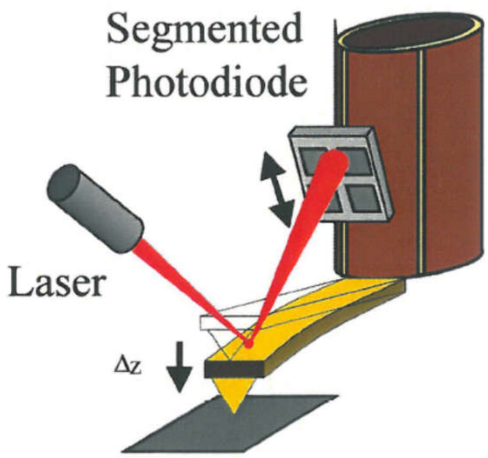

Figure 2-4 *A Schematic representation of principle of operation of Atomic Force Microscope [adapted from Ref. 70].*

At the free end of the cantilever (~ 100 – 200 μm long) a sharp tip (radius< 10nm) is mounted. When the tip approaches the sample initially it experiences a net attractive force due to long range Van der Waals forces. Beyond the contact position, repulsive force between tip and the sample leads to bending of the cantilever which can be sensitively measured using the deflection of laser beam falling on the cantilever as shown in figure 2.4. By keeping the bending of the cantilever constant, a constant force between the tip and sample can be ensured. Since the Van der Waals interaction has well known distance dependence it is possible to obtain topographic information by scanning the sample under the tip using a piezo driven scanning stage while maintaining a constant feedback signal. Topography is recorded as distance moved by the scan stage to maintain the set feedback signal while performing raster scanning of sample.

A typical force distance curve in an AFM measurement is shown in figure 2.5. The dependence of the Van der Waals force upon the distance between tip and sample is described by a Lennard Jones potential V which can be written as

$$V_s(z) = Az^{-12} - Bz^{-6} \tag{23}$$

where z is the tip sample distance and A and B are attractive and repulsive interaction parameters. In an AFM, the tip attached to the cantilever is bent upon interaction with sample according to the Hook's law:

$$V_c(z) = k\frac{(z-z_0)^2}{2} \tag{24}$$

where k is spring constant of the cantilever and z_0 is the minimum tip sample distance for an unbent cantilever. The force distance curve is a result of this coupled system of potential and varies as shown in figure 2.5.

The contact mode operation discussed above has disadvantage for sample that are soft or weakly bound to the substrate because the tip can damage the sample or drag it along while performing the scanning. To overcome this problem AC mode operation of AFM is used which operates in the intermittent contact regime. In the AC mode of operation, cantilever is mounted on a piezo driven cantilever holder and oscillated at its resonance frequency. When there is no interaction between sample and the tip, cantilever oscillated at free space amplitude'A_0'. Upon approaching the sample the oscillation gets damped because of interaction between tip and sample and amplitude of oscillation 'A' depends on the tip sample distance. The damping of amplitude which is ratio A_0/A can be used as feedback signal to record topography image of the sample. AC mode operation also facilitates imaging of the sample using phase of the oscillation. It has been shown that change in the phase of oscillation when tip is interacting with sample compared to phase in free space oscillation of cantilever is sensitive to the viscoelastic properties of the sample and can provide additional information about the material properties.

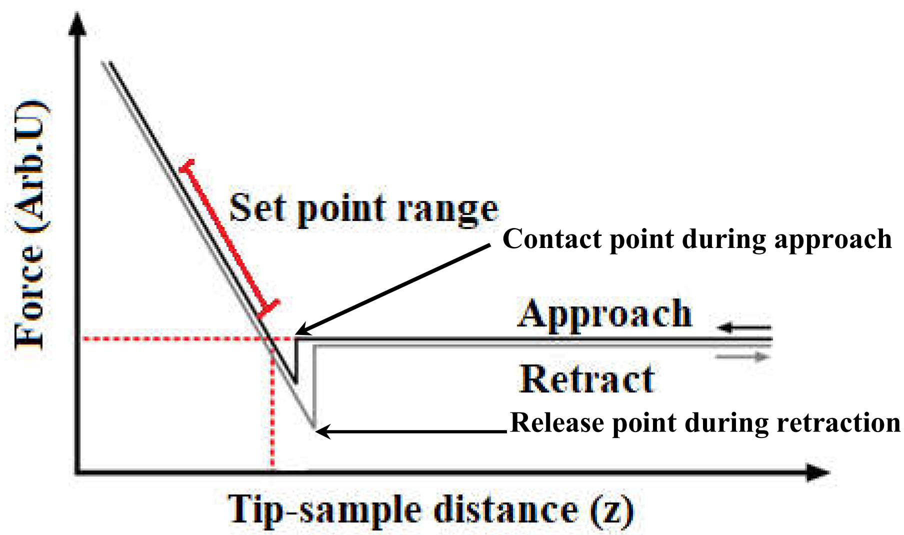

Figure 2-5 *Typical force-distance curve and set point selection for atomic force microscopy measurements [adapted from Ref. 70].*

The Alpha300SR system takes advantage of cantilever probe and beam deflection based feedback system for controlling the distance between sample and tip to fulfil the important requirement proposed by Synge in 1928 [71] to beat the diffraction limit of optical resolution. The NSOM system makes use of an aperture cantilever to illuminate the sample with evanescent field emanating from the probe tip (diameter ~50 – 100 nm). Scanning the sample in close proximity allows optical interrogation of the sample that is limited by the diameter of light source (aperture) rather than the wavelength of illumination. The Alpha300SR is equipped with multiple laser unit coupled to the microscope through a polarization maintaining single mode fiber.

2.4.2 Light Sources

The Aplha300SR requires at least three type of light sources together for operation in NSOM mode. (i) a white light LED system in combination with a diffuser is used for viewing and bright field imaging of the sample; (ii) a 980 nm laser for beam deflection based feedback control system and (iii) laser for near field excitation of the sample. The excitation lasers used for measurement reported in this work include 442 nm He-Cd laser (Kimon Koha, Tokyo, Japan) , 488 and 514.5 nm Ar-ion laser (Males Griot, USA) , 785 nm diode laser (Toptica Photonics AG, Graefelfing, Germany) and a super continuum source (Fianium, UK).

2.4.3 Detectors

The Alpha300SR is equipped with Hamamatsu H8259-01 (Hamamatsu Photonics K.K. Shizuoka, Japan) photon counting photomultiplier tube (PMT) with dark count of $54.2s^{-1}$.

This detector has good spectral response over the spectral range of 200nm to 800 nm and offer counting linearity of up to ~2.5 Mcps. For spectral measurements the multimode fiber coupled output is delivered to Actor Spectra pro 250i spectrometer (Princeton Instruments USA). The spectrograph allows use of 600, 1200 and 2400 line per mm grating blazed at 500 nm to record spectra using a Peltier cooled DU401-BR-DD (Andor, UK) deep depletion CCD camera with enhanced near infrared (NIR) sensitivity. Spectrometer also allows measurement of fast Raman image centred at the selected Raman shift with the help of photon counting avalanche photodiode.

2.5 Conclusion

Several numerical simulation tools like T-matrix method, the method of moments the discrete-dipole approximation the finite difference time domain method, the integral equation technique and the finite element method have been developed for solving Maxwell's equation for objects with arbitrary shape and refractive index profile. Of these FEM based simulation using COMSOL Multiphysics module is most user friendly and best suited for computing the field distribution in PNJ generated by dielectric micro-particles as it allows modelling of the particles with arbitrary shape and ease of visualization with standard softwares like Matlab with the live link feature. Details of these have been presented. We have also described the setup used for performing experimental measurements discussed in subsequent Chapters.

Chapter 3

Manipulation of photonic nanojet characteristics

Interaction of a dielectric microsphere with electromagnetic wave leads to many interesting phenomenon such as excitation of whispering gallery modes and sub-wavelength confinement of transmitted beam on shadow side which is often referred as photonic nanojet (PNJ). These are finding numerous applications in developing efficient photonic devices with improved performance. Compared to whispering gallery mode, efficient excitation of PNJ is a much simpler process and its characteristics can also be controlled in an easier manner. Further, being a non-resonant phenomenon PNJs are observed for a wide range of microsphere size and refractive index. In this chapter, we present the results of our investigations on different approaches for controlled manipulation of PNJ characteristics. We have shown that a simple core shell microsphere geometry allows generation of PNJs with vastly different characteristics by suitably selecting the refractive indices of core and shell microsphere as well as by changing centre to centre distance between the two microspheres. With careful choice of geometry and optical parameters highly elongated PNJ with length of up to 27λ or PNJ with free space confinement down to ~ λ/4.5 can be generated. Further, the flux emerging from microspheres can also be tuned in angle by making use of off-axis excitation with a focused Gaussian beam.

3.1 Introduction

Owing to their sub-wavelength near-field features PNJs are finding numerous applications in areas like Raman signal enhancement [39, 72], single molecule spectroscopy [18], fluorescence correlation spectroscopy [73], nano-photo-lithography [43, 44, 74] and nanoscopy [15, 16] etc. Effective utilization of PNJ for many of these applications requires precise control over its characteristics to achieve optimal performance. Therefore, over the period of time a considerable effort has been put in for tailoring of PNJs either for better confinement and thus higher peak intensity or for elongation of nanojet for high resolution far field applications. Several approaches have been proposed for manipulating the length and confinement of photonic jet. The results reported in literature show that the length and full width at half maxima (FWHM) of photonic nanojet depend on size and shape of micro particle, refractive index of particle and that of the surrounding medium, wavelength, polarization and beam profile of the excitation light etc. [37, 75]. Apart from conventional shapes like sphere and cylinder, particles of other shapes such as axicon [76], micro cuboids [77, 78], micro disks [79], concentric graded index microsphere or ellipsoids [35, 36], core-shell microspheres [80] [81] and truncated microspheres [82, 83] etc. have also been explored in various studies to investigate tuning of PNJ characteristics. More recently Eti et al. have demonstrated controlled manipulation of photonic nanojet by tuning the refractive index in liquid crystals filled micro shells [84].

In this chapter, we present the results of our studies on the variation of FWHM and length of PNJ generated from micro-spheres having crescent shape refractive index profile (CSRP). The results show that PNJ with FWHM down to ~λ/4.5 can be achieved in free space with multilayer CSRP lossless dielectric microsphere of 3 μm diameter. In the presence of commonly used substrates with higher refractive index this would enable writing feature as small as ~ λ/6. It has also been demonstrated that by using off axis illumination with a tightly focused beam it is also possible to achieve angular tuning of PNJ emission.

3.2 Theory and simulations

The analytical and numerical approaches developed and applied to study the near as well as far field distribution of electromagnetic field in the photonic nanojet generated by microscopic dielectric objects have been described in Chapter 2. Analytical approach based on Mie theory and its suitable extension have been used to analyse the field distribution inside and outside the microsphere for concentric as well as eccentric inclusions [80, 85-87]. However, with increasing number of inclusions, the number of interfaces and boundary conditions make the derivation of analytical solution intractable. Among the numerical The Finite Difference Time Domain Method (FDTD) is a popular technique that was used to demonstrate the existence of photonic nanojet by Chen et al [9]. However, due to regular shape of grids (square/cubic element in 2D/3D) used in FDTD, it requires extensively large number of elements to capture the details of object with sharp or irregular feature such as at the apex of crescent in the present work. Discrete dipole approximation, multiple multipole method and FEM based approaches have also been explored to study the generation and characteristics of nanojet from dielectric objects [88-90]. FEM based computation in particular has an advantage that it enables handing the geometries with varying feature sizes and hence allows better representation of sharp crescent tips. We have used finite element method (FEM) based software package COMSOL Multiphysics 4.2 for solving the Maxwell's equations in our simulations. The entire computational domain was meshed with triangular elements of varying sizes using the built-in non-uniform mesh option. It is important to note here that the maximum mesh size used must be sufficiently smaller than the typically recommended element size of ~ λ/10 to ensure numerical accuracy of the simulation results. The maximum elemental size of the triangle used in our simulation was restricted to 20 nm and finer meshes were used near the interfaces. Further refinement in the mesh size did not lead to any significant change in the results. All simulations were carried out with perfectly matched layer (PML) surrounding the region of interest to ensure that no back-reflection takes place at the finite boundaries of computational domain. We used direct solver SPOOLES (Sparse Object Oriented Linear Equations Solver) which ensures the convergence of simulation with relatively lesser memory requirement. Since the experimental measurements involve illumination with focused Gaussian beam, the standard plane wave illumination used in COMSOL script was suitably modified. Following the convention used in Multi-physics module, we take the x-axis as direction of propagation and electric field oscillations were taken along z-axis. The variation of electric field as a function of propagation distance is given by the following definitions [81]:

$$E(x,y) = E_0\sqrt{\frac{\omega_0}{\omega(x)}}e^{-(y/\omega(x))^2}\cos\left(-kx+\eta(x)-\frac{ky^2}{2R(x)}\right) \tag{3.1}$$

where $\omega(x)$, $\eta(x)$ and $R(x)$ are the beam radius as a function of x, the Gouy phase and the radius of curvature of the wave front respectively and are defined as:

$$\omega(x) = \omega_0\sqrt{1+\left(\frac{x}{x_0}\right)^2}; \quad \eta(x) = \frac{1}{2}atan\left(\frac{x}{x_0}\right)$$

and $R(x) = x\left(1+\left(\frac{x_0}{x}\right)^2\right)$; with$x_0 = \frac{\pi\omega_0^2}{\lambda}$ being the Rayleigh range

The beam waist was taken as ω_0 =2 μm to ensure that the microsphere is fully illuminated. All simulations were carried out using direct solver for computing the field. To ensure convergence, the mesh size was refined till the variation in computed field at any given point is $<10^{-5}$.

3.3 Results and Discussion

In order to device a suitable strategy for manipulation of PNJ, we first investigated the effect of different parameter of microsphere on nanojet characteristics. Figure 3.1 shows the effect of microsphere size on the axial length and lateral confinement of PNJ generated by silica microsphere (n_p = 1.45) placed in air (n_o = 1.0) under plane wave illumination with 500 nm wavelength. It can be seen from figure that sub-diffraction (~ λ/2) lateral confinement is maintained for microspheres of sizes less than ~3μm. As the size of microsphere reduces, both the length and the width of PNJ decrease resulting in higher peak intensity of the nanojet. For microsphere of size smaller than 0.5μm radius, the peak intensity in the nanojet lies inside the microsphere due to higher curvature seen by the photon falling on the microsphere surface. This effectively leads to an increase in the width of PNJ emerging on the shadow side of the microsphere.

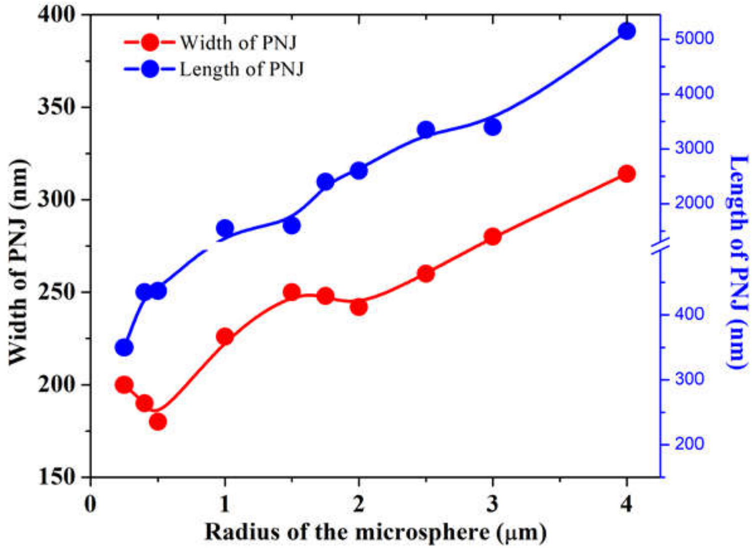

Figure 3-1 *Length and width of PNJ as a function of radius of the microsphere. Illumination wavelength is 500 nm, microsphere having refractive index n_p = 1.45 was placed in air.*

The effect of excitation wavelength on the length and width of PNJ is shown in figure 3.2 for a fixed size and refractive index of microsphere. As noted earlier, better confinement of PNJ is obtained for longer wavelength since for a fixed size of microsphere the size parameter reduces with increase in the wavelength.

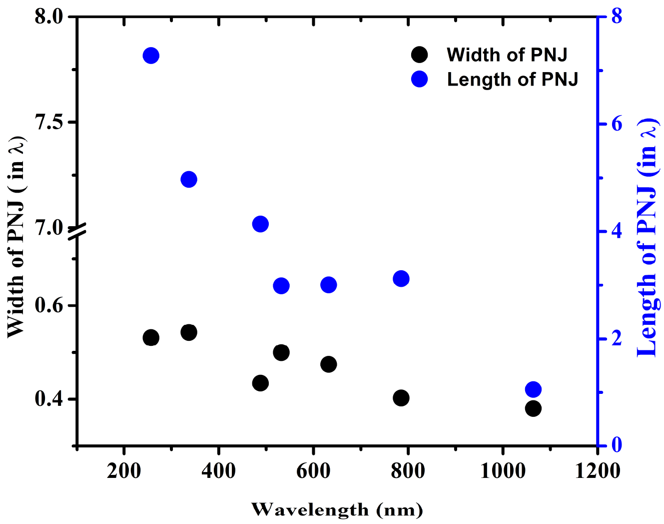

Figure 3-2 *Wavelength dependence of length and width of PNJ generated by 3μm diameter microsphere. Refractive index of microsphere was taken as n_p = 1.45 in air surrounding.*

In the next step we carried out numerical simulations for microsphere of 3 μm diameter while varying the refractive index 'n_p' of microsphere from 1.3 to 2.0. A typical intensity distribution in the photonic nanojet and the variation of FWHM as a function of refractive index of micro-sphere is shown in figure 3.3. As the refractive index of microsphere (n_p) increases, the FWHM of photonic nanojet generated by microsphere decreases due to sharper bending of the photons at curved surfaces of microsphere resulting in a better confinement. The smallest FWHM of 204 nm was achieved for n_p = 1.7. Further increase in n_p leads to the formation of PNJ that has peak intensity inside the microsphere. Thus the usable PNJ protruding outside the microsphere have larger FWHM. The transverse profile of nanojet (along the y-axis) for microsphere having refractive index 1.7 is shown in the inset plot. It may noted that the results shown here correspond to non-resonant cases so as to avoid unusual narrowing/contraction of the PNJ.

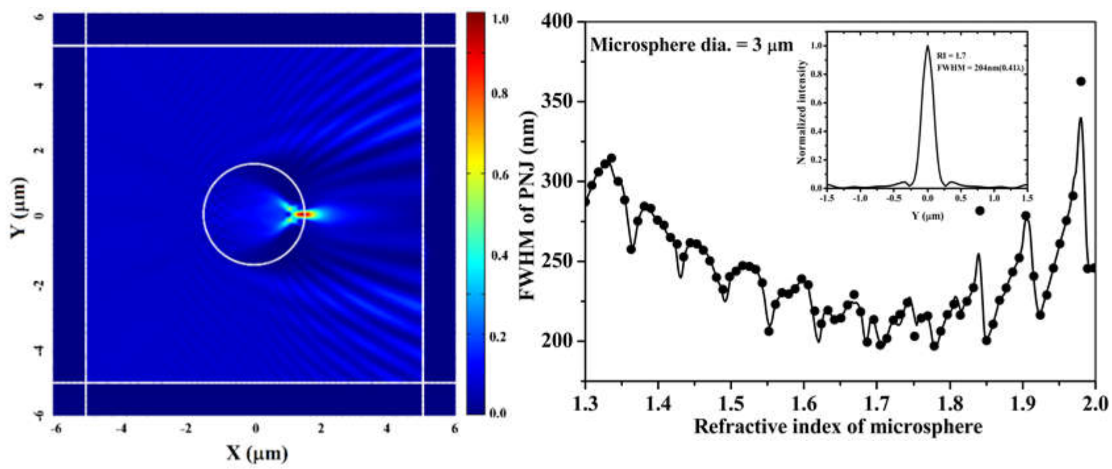

Figure 3-3 *A typical intensity distribution generated by 3 μm microsphere (n_p = 1.7) illuminated with 500 nm excitation wavelength (left) and variation of FWHM of PNJ as a function of refractive index of microsphere (right). The inset on right panel shows the transverse intensity profile of the nanojet formed by microsphere having refractive index 1.7.*

3.3.1 Manipulation of PNJ using core-shell microsphere

Though the characteristics of PNJ generated by dielectric microsphere can be altered by changing size, shape, refractive index and parameters of illuminating beam, this allows tuning in PNJ parameters only over a limited range. A core-shell structure comprising two layer microspheres can provide additional control for manipulation of nanojet characteristics through change in refractive indices and separation between the centres of constituent microspheres. We have, therefore, explored the possibility of using core-shell microsphere for manipulation of PNJ characteristics. A schematic of the core shell microsphere geometry considered in simulation is shown in figure 3.4. The diameter of the core and shell were taken as 3µm and 2µm respectively. The core (n_c) and shell (n_s) refractive index was taken as 1.7 and 1.3 and the separation between core and shell centre was varied from -0.5µm to + 0.5µm in steps of 0.05µm along the direction of propagation which is also the symmetry axis.

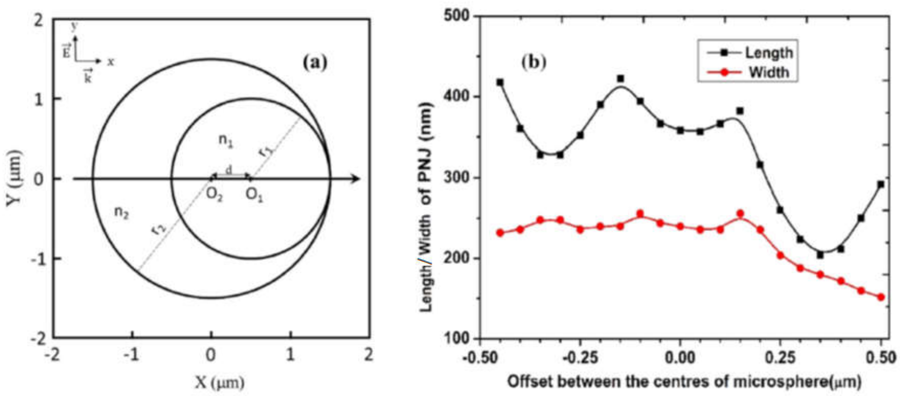

Figure 3-4 *The geometry of micro-sphere used in the simulation (a) and the FWHM (redline with circle symbol) and length (black line with square symbol) of PNJ (b) generated by two eccentric microspheres having refractive index 1.7 (inner microsphere) and 1.3 (outer microsphere)*

The incident plane wave was considered to be propagating in the ‘x’ direction with TM polarization as shown in figure 3.4a. The origin of the coordinate system was chosen to be at the centre of the shell microsphere. The length of nanojet for different offset positions are shown figure 3.4b. It can be seen that the length of nanojet increases when core is moved away from the centre along the direction opposite to the incident beam (-x axis). Moving the core centre in beam direction leads to shortening of the nanojet length. The maximum elongation in the length of the nanojet is obtained when the core centre is offset by approximately –0.5µm from the shell centre whereas best confinement is achieved when the core centre is offset by +0.5µm forming a crescent structure as shown in figure 3.4a.

Simulations were also carried out to investigate the effect of interchanging refractive index of core and shell microsphere on characteristics of PNJ. While the lateral confinement of nanojet and peak intensity was found to be higher when core refractive index is higher than the shell refractive index ($n_c > n_s$), the length of nanojet was found to be longer when $n_s > n_c$.

3.3.2 Manipulation of PNJ width using multi-layer crescent shape refractive index profile

The simulation results for simple core shell microsphere show that it is possible to generate photonic nanojet with controllable length and confinement. While the generation of highly elongated PNJs is relatively easy, generating a highly confined PNJ is challenging. The core-shell microsphere was found to provide best lateral confinement when the inclusion microsphere touches the surface of the shell at the point of emission of nanojet forming a crescent shaped refractive index profile in the microsphere i.e. when the centres of two microspheres are separated by d ~ r_2-r_1. We carried out systematic investigation of the effect of multi-layer crescent shape refractive index profile (CSRP) with a goal to generate PNJ with best possible lateral confinement. Numerical simulations were performed by introducing microsphere of varying refractive indices in the range 1.3 to 2.1 into the crescent shape microsphere. The constraint that is applied to the refractive indices of different layer is that outer microsphere should have lower refractive index than the inclusion microsphere as shown in figure 3.5.

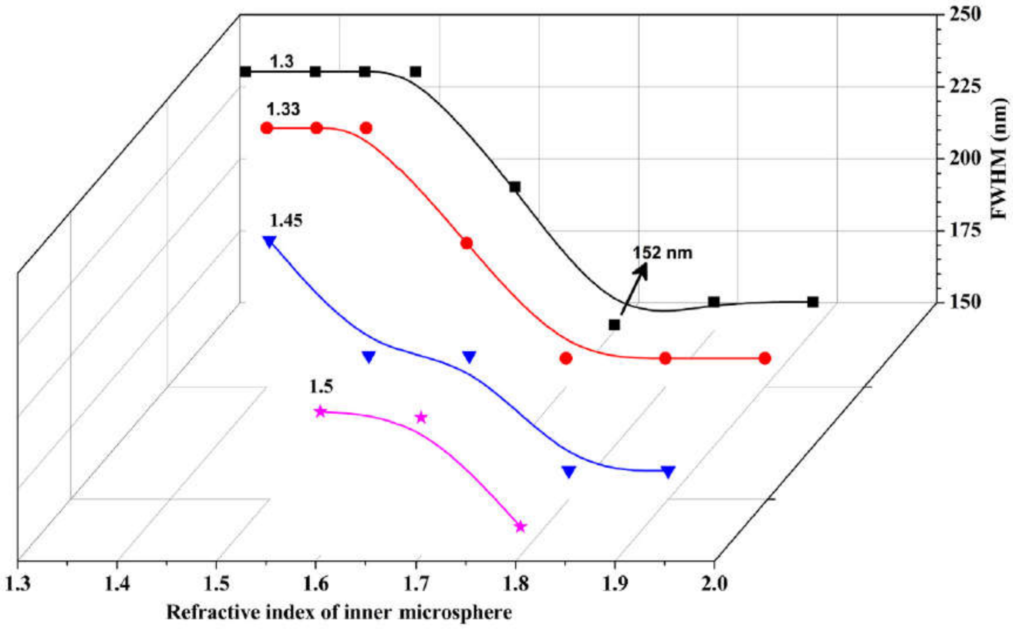

Figure 3-5 *Variation of the FWHM of nanojet with refractive index of two layer crescent shaped microsphere. Refractive index of the outer layer is shown along each graph while the refractive index of the inner microsphere is varied in the range 1.3 - 2.0. The inner layer is constrained to have higher refractive index than the outer microsphere. For each case, optimization is stopped when the peak intensity in nanojet is formed inside the microsphere.*

For a chosen refractive index of the outer microsphere, the refractive index of inner layer is varied in the above mentioned range of refractive index as long as the peak intensity region in nanojet is outside the microsphere surface. Note that the nanojet with peak intensity inside the microsphere will be of no interest for many applications. The optimum combination of refractive index obtained was 1.3 and 1.7 for the outer and inclusion microspheres respectively which leads to a PNJ with FWHM of 152 nm. The intensity distribution corresponding to this configuration is shown in figure 3.6 (a).

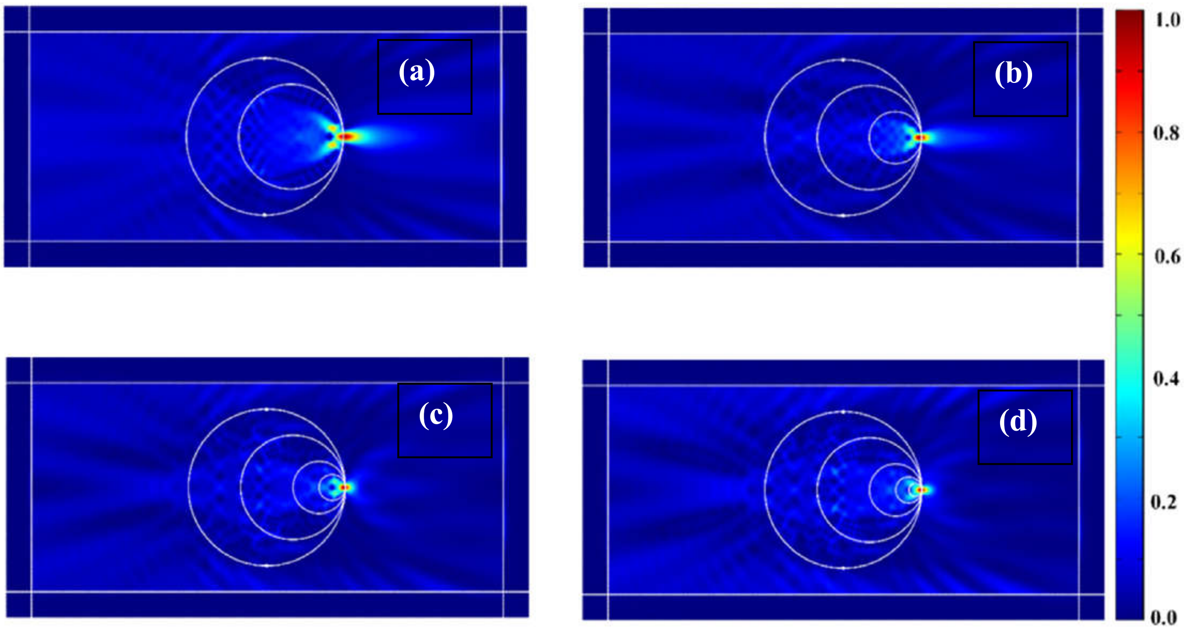

Figure 3-6 *Map of normalized power flow in photonic nanojet for multilayer CSRP microspheres with 2, 3, 4 and 5 layers (a-d). Refractive index of different layers were optimized to achieve best lateral confinement i.e. minimum FWHM (Please refer to Table 3-1 for the refractive index values).*

Introducing a second microsphere with refractive index higher than the first inclusion leads to further narrowing of lateral dimension of the PNJ. For this, a microsphere with diameter 1μm was placed inside the two layered CSRP structure discussed above and the refractive index of all three layers were varied from 1.3 to 2.1, keeping refractive index of innermost inclusion layer higher than that of the immediate overlaying crescent shaped layer and so forth. The smallest FHWM obtained for this geometry was ~140 nm (λ/3.6) for refractive index of different layers being 1.9, 1.6 and 1.3 starting from the innermost inclusion to the outer microsphere respectively. The intensity distribution for this geometry is shown in figure 3.6(b).

We investigated the effect of further increase in the number of inclusions by introducing microspheres of diameter 0.5 μm and 0.25 μm, resulting in up to five crescent shaped layers. The optimized refractive index of different layers and corresponding FWHM and length of the PNJ have been presented in Table 3.1. The smallest FWHM obtained is 110 nm (~ λ/4.5) for five layered CSRP microsphere with refractive index of layers being 2.1, 1.8, 1.7, 1.6 and 1.3 starting from the innermost inclusion. The intensity map for the PNJ generated in this geometry are shown in figure 3.6 (c) & (d).

The width and length of PNJ generated by these CSRP microspheres are shown in figure 3.7. It can be seen from the figure that with increasing number of layers in CSRP microsphere, the FWHM of the photonic nanojet reduces progressively from 204 to 110 nm. However the change in FWHM becomes quite small after four to five layers of crescent shaped refractive index profile.

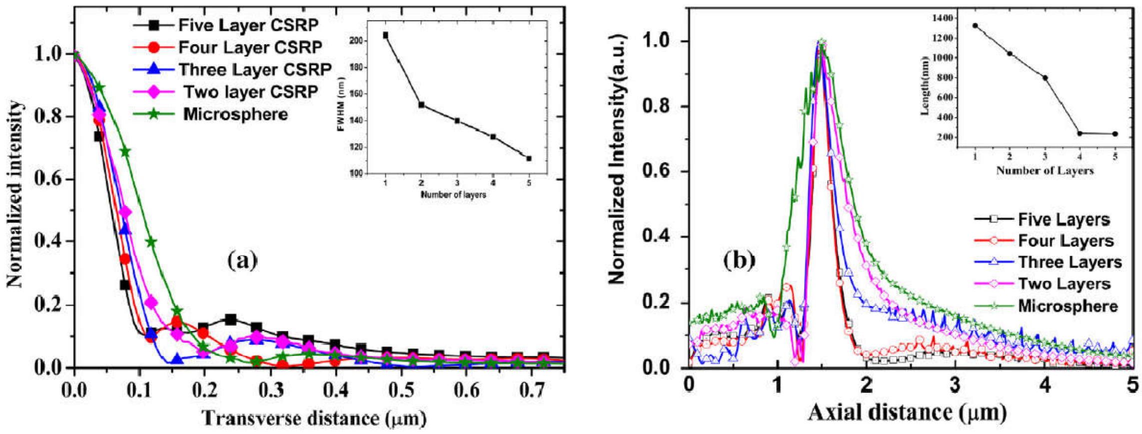

Figure 3-7 *(a) Transverse and (b) longitudinal normalized intensity profile of the nanojet generated by multilayer microsphere with crescent shape refractive index profile. Refractive indices of different layers were optimized for generating nanojet with best confinement. Inset in the graph shows FWHM and length as a function of number of layers.*

To study the effect of underlying substrate on the PNJ we performed simulations considering CSRP microsphere over a substrate of thickness 0.5 μm. The refractive index of the substrate was varied in the range 1.3 to 2.4 and illumination wavelength kept fixed at 500 nm. A typical intensity distribution of the photonic nanojet generated by such configuration (design corresponding to fifth row in table 1) is shown in figure 3.8 for a substrate of refractive index 1.5. The FWHM of the PNJ inside the substrate was found to be 108 nm (0.216λ) which is only marginally better than the FWHM obtained in air. It should be noted that the observed reduction in spot size is much smaller compared to what is expected from reduction in wavelength of light in the substrate. We have therefore carried out further optimization of the refractive index in different layers of CSRP taking the refractive index of substrate into account. The result show that for substrates with different refractive index it is possible to improve the confinement by factor of approximately 1.25 beyond what is obtained by CSRP profile optimized for air as surrounding medium.

Table 3-1 *Properties of PNJ generated by CSRP microspheres upon illumination with 500 nm wavelength in free space.*

No. of layers	Design of microsphere	Refractive indices of different layers	Diameter (μm) of different layers	FWHM(nm) of PNJ
1	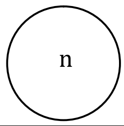	n = 1.7	3.0	204
2	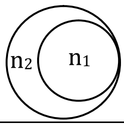	$n_1 = 1.7, n_2 = 1.3,$	d1 = 2.0, d2 = 3.0,	152
3	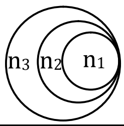	$n_1 = 1.9, n_2 = 1.6, n_3 = 1.3,$	d1 = 1.0, d2 = 2.0, d3 = 3.0,	140
4	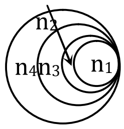	$n_1 = 2.0, n_2 = 1.7, n_3 = 1.6, n_4 = 1.3,$	d1 = 0.5, d2 = 1.0, d3 = 2.0, d4 = 3.0,	128
5	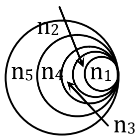	$n_1 = 2.1, n_2 = 1.8, n_3 = 1.7, n_4 = 1.6, n_5 = 1.3,$	d1=0.25, d2 = 0.5, d3 = 1.0, d4 = 2.0, d5 = 3.0,	110

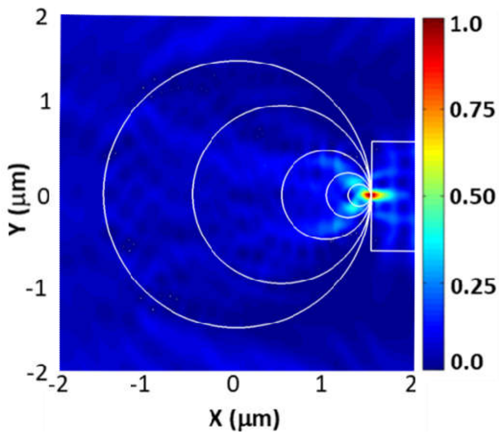

Figure 3-8 *Intensity profile of a five layered CSRP microsphere placed on substrate of refractive index 1.5. Excitation wavelength is 500 nm. FWHM of the nanojet in substrate is 108 nm.*

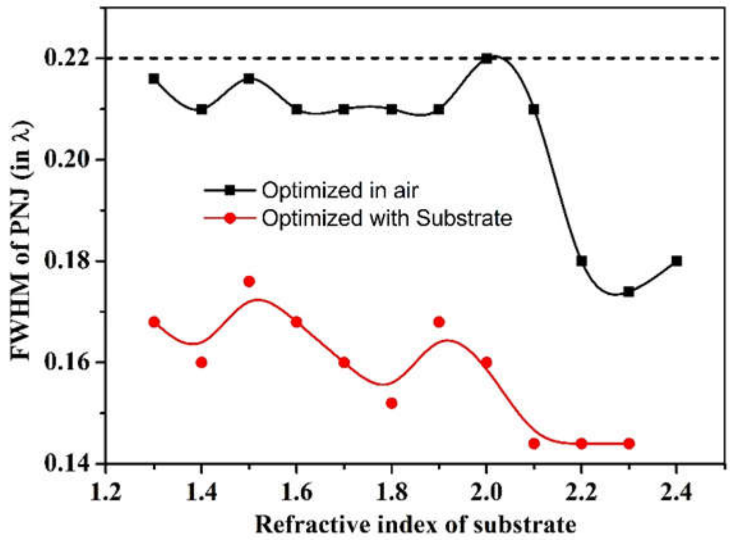

Figure 3-9 *Size of spot on the substrate of refractive index (1.3 to 2.4) created by a five layered CSRP micro-sphere, optimized for Air as surrounding medium (black squares) and optimized considering the refractive index of substrate (red circles). The dotted line represents the FWHM of the nanojet in air. Line through the data is spline curve to guide the eye.*

Figure 3.9 shows the transverse width of PNJ when a multilayer CSRP microsphere is placed on a substrate. The spot size obtained was 87 nm (~λ/5.7) for CSRP optimized considering only air in surrounding medium. The spot size could be further reduced by tweaking the refractive index of different layers of CSRP microspheres considering effect of the underneath substrate in contact with microsphere. The smallest spot size obtained was ~ 72.5 nm (~ λ/6.7) corresponding to substrate refractive index of 2.12. Although the fabrication of CSRP microsphere with desired index profile is technologically challenging but there is no fundamental physical limitation which might restrict its realization. Note that with growing sophistication and maturity in manufacturing technology it is possible to fabricate micro-cylinders with arbitrary refractive index profile with stack and pull method wherein stack can be prepared either by additive manufacturing technology or by rolling successive layers of low index materials around the core layer in eccentric fashion. For spherical structures, layer-by-layer growth technique can be used to fabricate microsphere with crescent shaped refractive index profile [91-94]. Alternatively controlled doping of microsphere via thermal diffusion of a suitable dopant with high refractive index can be used to achieve the desired profile. It is pertinent to note here that microsphere with eccentric inclusions are also of immense importance for various applications including plasmonic light harvesting and high-efficiency solar up-conversion [95, 96], enhancement of multipolar resonances for improving the efficacy of sensing and the nonlinear optical response in plasmonic materials [97] etc. which is driving the effort to fabricate such structures.

3.4 Angular tuning of PNJ

PNJs are primarily generated using symmetric optical systems such as dielectric spheres, cylinders, ellipsoids etc. under illumination with either plane wave or a focused Gaussian beam. Symmetry in the system leads to generation of PNJ propagating in a straight line, often collinear with the direction of illumination. It has been recently shown that due to different phases acquired by the wavefront propagating through different regions of dielectric corner and asymmetric optical elements, PNJs with curved intensity profile can be generated [46]. These type of electromagnetic fields can be of immense application for nano-particle manipulation along a curved path for getting around the obstructions thereby enhancing the transport and control over the particle’s motion [98]. We investigated the use of off axis illumination with focused Gaussian beam to achieve angular tuning and generation of curved PNJ. Time averaged power flows for symmetric (on-axis) and offset illumination are shown in figures 3.10 a and b respectively. As one would expect, symmetric illumination such that the beam waist coincides with the microsphere centre leads to a PNJ propagating in the direction of illumination. As the beam waist position is moved away from microsphere centre, PNJ with curved intensity profile are generated. Bending angle of the PNJ is defined as angle between the lines joining peak intensity point in PNJ to the exit point on shadow side of microsphere and point where intensity the of the PNJ reduces to half of the peak intensity in tail region (figure 3.10 b). The bending angle for beam waist offset from the microsphere centre by 3 μm along positive y axis was found to be 22^{o}. Similar results were obtained by Yue et al. [46] for asymmetric dielectric particle comprising a wedge prism attached with a cuboids illuminated by plane wave. Detailed analysis of the evolution of wavefront in asymmetric object reveals that the observed bending can be attributed to the interference of scattered wave from different regions of the beam that experience different phase changes on propagation through the microsphere.

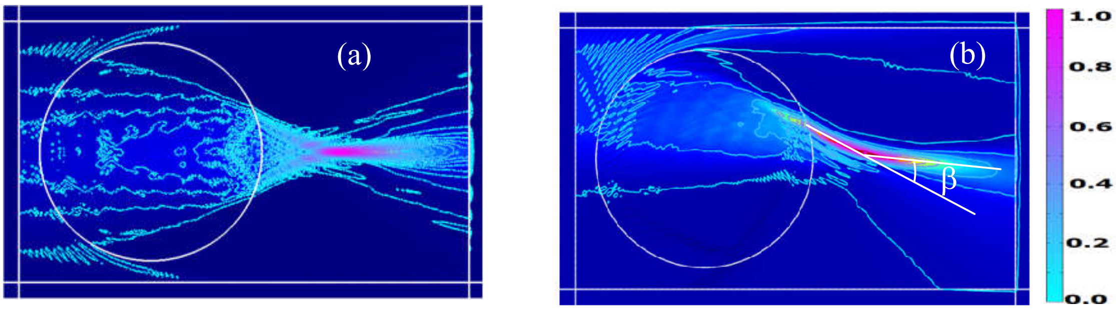

Figure 3-10 *Intensity map of PNJ generated using on axis illumination (a) and off-axis excitation of microsphere (r = 4 μm; n_p = 1.45) with focused Gaussian beam (λ = 500 nm, ω_o = 4 μm). Beam waist was offset from the microsphere centre by 3μm (b).*

Simulation results obtained using COMSOL were also validated with the generalized Lorentz Mie theory for computing the electromagnetic field and scattering efficiency plot for microspheres illuminated with Gaussian beam. For large size microsphere (diameter ~ 50 μm) angular tuning of the PNJ emission up to 70^{o} with respect to the illumination axis could be achieved.

3.5 Summary

To conclude we have shown that extremely narrow PNJ with FWHM down to ~λ/4.5 in free space can be generated using the microspheres having multi-layer crescent shape refractive index profile. The multi-layer CSRP microsphere allows confining PNJ well below the dimension that can be achieved using sub-micron sized microspheres and offer significant advantage in terms of ease in handling for various applications. For the applications requiring direct contact with microsphere the substrate refractive index was also taken into account to demonstrate lateral dimension of ~λ/6.7. Further, we could control the direction of flux emerging from microspheres to generate curved PNJ using off-axis excitation with a focused Gaussian beam.

Chapter 4

Use of photonic nanojet for enhancement of transmission through nano aperture

In this chapter, we present the results of our studies on use of PNJ s for enhancing the throughput of the cantilever based hollow probes used in Near Field Scanning Optical Microscope (NSOM). Our studies showed that with an appropriate choice of the dielectric microsphere an order of magnitude enhancement could be achieved in transmission through the probe. In addition with the use of PNJ the transmission through the NSOM tip was found to be less sensitive to the axial and lateral offset between the beam waist and symmetry axis of the probe tip.

Work discussed in this chapter has resulted in the following publications:

1. "Photonic nanojet assisted enhancement in transmission of light through hollow pyramid shaped near field probes'. S. Patel, P. K. Kushwaha, M. K. Swami, and P. K. Gupta, Journal of Optics 17, 05500 (2015).

4.1 Introduction

Near-field Scanning Optical Microscopy (NSOM) has become a very valuable tool for optical characterization of nano-materials and devices [99, 100] because it allows optical spectroscopic measurement on materials with resolution beyond the diffraction limit. NSOM systems mostly use either a metal coated pulled optical fiber probe or a cantilever with hollow pyramid-shaped tip having nanometer size aperture for confining the excitation light to a sub-diffraction spot size [101]. Because of the sub-wavelength aperture size a large fraction of light launched in the probe is either reflected back or lost as heat in the metal coating. The throughput of these probes is therefore rather low, typically ~10^{-5}–10^{-6} for pulled optical fiber probe [102, 103] and up to an order of magnitude better for the hollow pyramid probes [104-106]. It is not possible to increase the power available at the sample by increasing the power input to the probe because of the thermal damage to the probe or the damage caused to the sample in contact with a heated probe [107, 108]. Apertureless NSOM probes that utilize the plasmonic properties of metal thin films coated on an AFM tip for strong field localization have also been explored for improving the power available at the sample and thus improve the signal to noise ratio. Unlike the aperture probe for which the maximum input power is limited to 1–2 mW, the apertureless NSOM probe allows use of higher input power for illuminating the tip thereby increasing the near field signal at tip apex. Since the apertureless NSOM probes utilize sharp tips for achieving strong local field enhancement it offers both improved signal to noise ratio as well as higher resolution. However, a drawback with this approach is the requirement of illumination with appropriately polarized light to exploit the plasmonic enhancement of field. Further, these probes require elaborate detection schemes to eliminate the large background arising due to scattering of the far field illumination and these can be used for a limited spectral range [109, 110].

Novel nano-aperture shapes such as bowtie [111], triangular [112], C-shaped, fractal structures [113,114] or use of wave-front modulation [37] etc. have also been explored to improve the throughput of the probes by selective confinement of light depending on the symmetry of the tip and polarization of the source. More recently campanile tips that are capable of efficient coupling of far-field light to the near field and vice-versa over a broad spectral range has been developed and used for background free hyper-spectral imaging with resolution down to 40 nm [115]. However, practical implementations employing these probes have been limited due to difficulties involved in the fabrication of such tips. Further, the use of such probes might also complicate the interpretation of the data due to complex nature of the field at the tip apex. A simpler approach to improve the throughput of the probe would be to increase the cone angle of the probe and use a high numerical aperture (NA) objective for focusing the light at the tip apex. The maximum usable NA in an NSOM system is also limited because of the requirement of the working distance to accommodate the cantilever holder between objective and the sample. For a typical aperture probe having cone angle of 60-70 degree the usable NA is thus limited to ~ 0.5. We have therefore investigated the use of sub-wavelength confinement of light via photonic nanojet (PNJ) to improve the coupling of light into the probe and thus enhance its throughput. For this we considered a modified NSOM probe with a microsphere of suitable size and refractive index inserted into the hollow pyramid shaped cantilever. The theoretical simulations and experimental results show that with an appropriate choice of the dielectric microsphere an order of magnitude enhancement in transmission of the probe is feasible.

4.2 Theory and calculations

4.2.1 Photonic nanojet

We first investigated the effect of the microsphere size and refractive index on the characteristics of the PNJ considering plane wave illumination. Photonic nanojet formed by two commonly used microspheres namely silica (n = 1.45) and polystyrene (n = 1.59) of size varying from 1 -10 µm were simulated using Finite Element Method (FEM) based software COMSOL. The results of simulations for microspheres of diameter 3 µm, 5 µm and 10 µm illuminated with plane wave are shown in shown in figure 4.1.

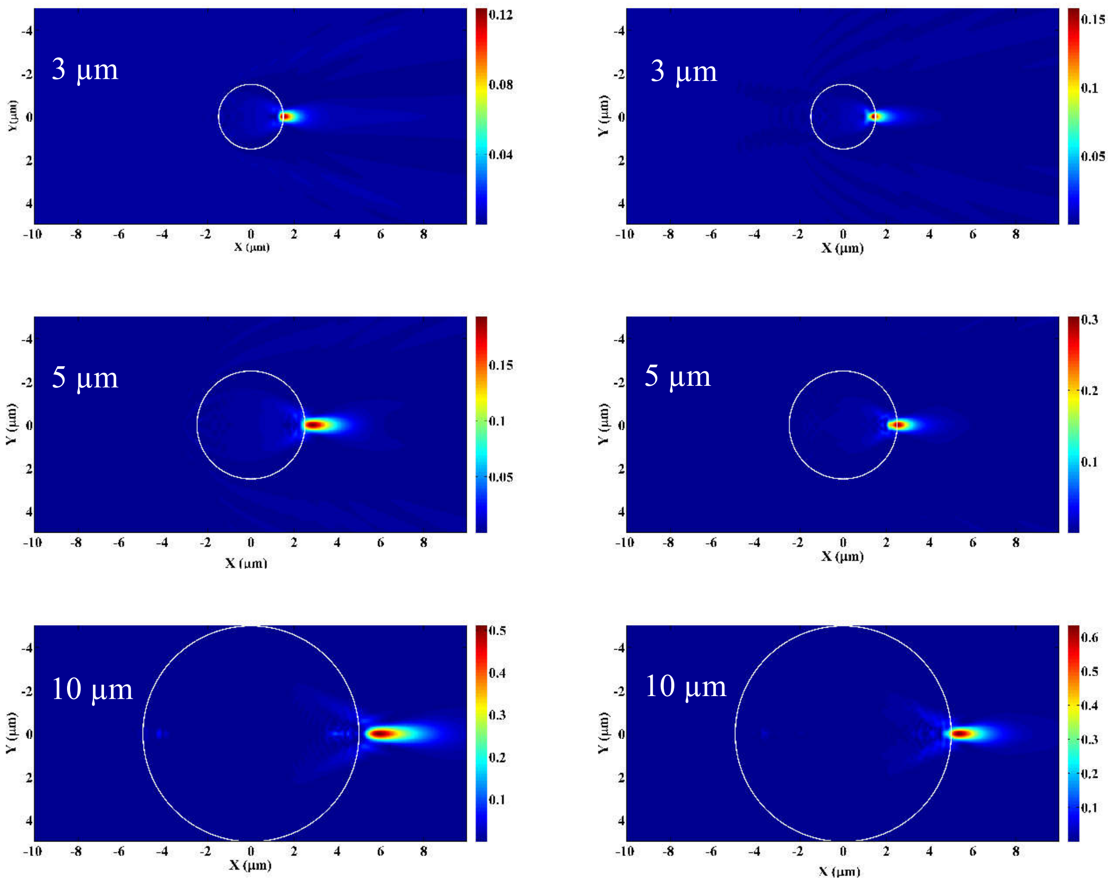

Silica (n = 1.45) **Polystyrene (n = 1.59)**

Figure 4-1 *Effect of size and refractive index on the characteristics of photonic nanojet.*

It can be seen from the figure that for a given size, length of the PNJ is shorter for polystyrene microspheres compared to that of silica microsphere. This is to be expected as the larger refractive index contrast with the surrounding leads to a sharper bending of the light at the interface resulting in better confinement but with reduced length of the PNJ. The results of simulations also show that the length of nanojet increases with increasing diameter of the microsphere. However, it should be noted here that in the modified probe the distance between aperture tip and microsphere surface also increases linearly with the increase in the size. In addition the transverse dimension of the PNJ also increases with size of the microsphere. Since with silica microsphere the length of the PNJ can be large even for smaller sized microsphere we considered silica microspheres for further optimization.

4.2.2 Simulation of transmission through cantilever type hollow NSOM probe

Simulations were carried out to estimate the optimal transmission that can be achieved through an NSOM probe having a pyramidal shaped tip with aperture of approximately 100 nm by insertion of silica microspheres of different size. In addition to size of the microsphere we also considered the effect of illumination with focused Gaussian beam which can also influence the length of PNJ [116, 117]. The result of these studies show that length of nanojet generated with diverging beam (beam waist located before the microsphere) is longer compared to that with the converging beam. A schematic of the probe geometry used for both, experiments as well as numerical simulations is shown in figure 4.2. The probe consists of a rectangular silicon cantilever with an integrated hollow silicon oxide tip (tip height ~ 18 μm) which was coated with a layer stack of Cr, Ti and Al to prevent leakage of light from side of the probe. The aperture size at tip apex and full cone angle of the probe was taken as 100 nm and 70 degree respectively. The transmission was calculated using power flow through a square aperture of size 250 nm × 250 nm placed immediately after the tip apex.

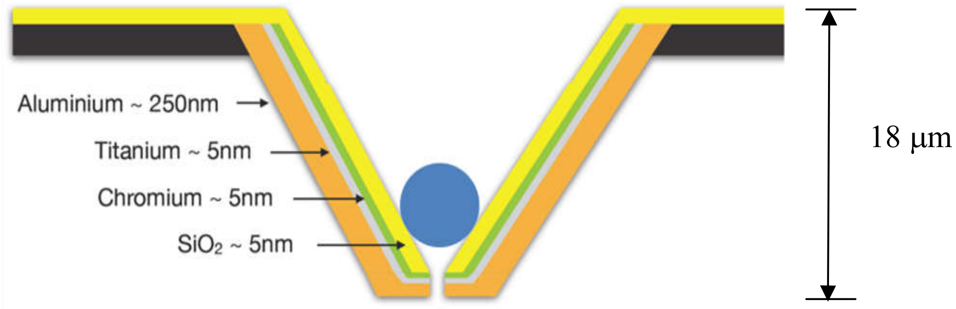

Figure 4-2 *Schematic of the geometry of NSOM probe used for the simulations of near field transmission.*

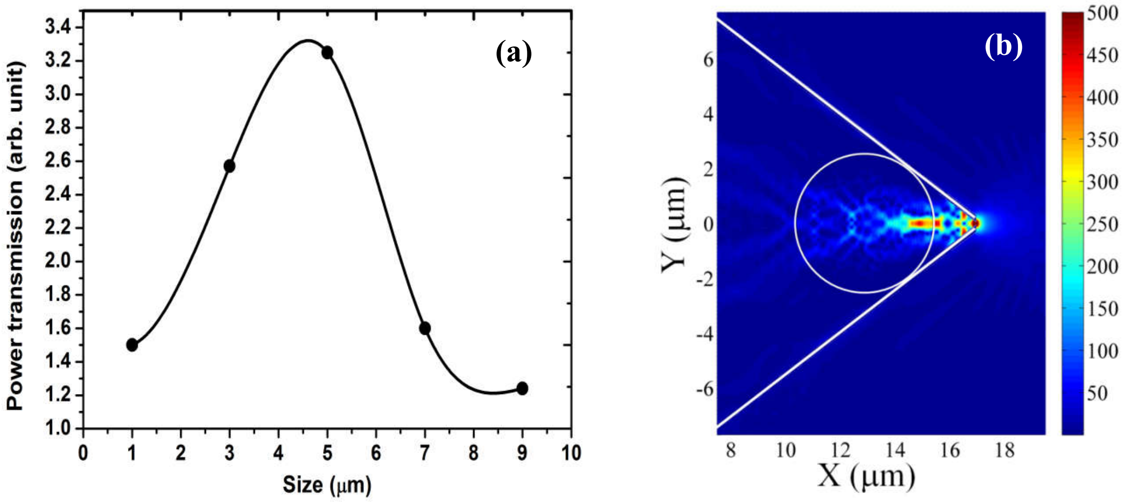

Figure 4-3 *(a) Variation of probe transmission as a function of the size of silica microsphere; filled circles are the results of numerical simulation and solid line has been drawn to guide the eye (b) simulated distribution of power flow for a probe with 5 µm silica microsphere. The source for excitation was 850 nm TM polarized (H_0 = 1 A/m) Gaussian beam focused at 8.25 µm inside the tip.*

Dependence of probe transmission as a function of the size of silica microsphere insert (1-9 µm) is shown in figure 4.3 (a). The results suggested that a silica microsphere having diameter ~ 5µm would be a good choice. Typical field distribution for such a probe is shown in figure 4.3 (b). It was also observed that best transmission is obtained when the beam waist of illuminating Gaussian beam is kept before (excitation with diverging beam) the microsphere such that it is focused at 8.25 µm inside the tip.

4.3 Experimental results and discussion

4.3.1 Preparation of modified probe

To insert a microsphere in the hollow cantilever NSOM probe a drop of aqueous suspension of the 5 µm silica microspheres (Polysciences, Inc. USA)) was placed on the base of cantilever and allowed to dry in air.

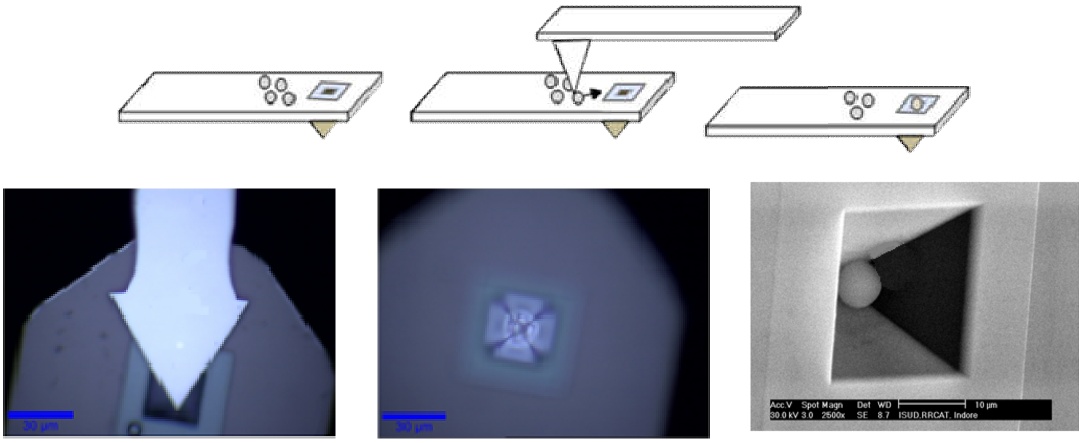

Figure 4-4 *Schematic of the steps involved in the preparation of modified NSOM tip with microsphere incorporated in the probe (top) and optical micrograph of AFM tip over NSOM probe, along with SEM image of probe with microsphere in it (bottom).*

The microsphere closest to the aperture base was then dragged into the hole using a contact mode atomic force microscopy tip landed on the NSOM cantilever. Figure 4.4 shows the schematic of the different steps involved in preparation of modified tip.

4.3.2 Measurement of enhancement

To test the concept, light from a broad band super luminescent diode source (λ_0 = 850 nm, FWHM ~ 40 nm) was launched into a single mode fiber and coupled to the NSOM microscope (Alpha300SR, WiTec, GmbH, Germany). A schematic of the experimental setup is shown in figure 4.5. The NSOM probe was illuminated with Nikon 20 X, 0.4 NA microscope objective and the light transmitted through the tip apex was collected in far field using a high-NA objective (60 X, 0.75 NA). The incident beam power used for these measurements was < 1 mW and there was no apparent degradation of the tip due to photo-thermal damage.

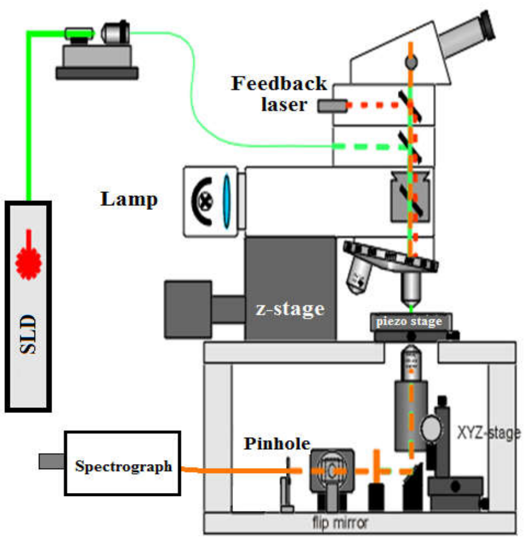

Figure 4-5 *Schematic diagram of the near field scanning optical microscope used in experiment.*

In figure 4.6 we show the far field transmission spectra of the cantilever aperture probe before and after inserting a 5 μm silica microsphere in to the hollow probe. While the throughput of aperture probe used in our experiments was measured to be ~ 10^{-5}, the transmitted intensity of the modified probe showed an order of magnitude enhancement as compared to the bare probe. It is also important to note here that being a non-resonant phenomenon, PNJ can provide the enhancement over a large wavelength range. This can be seen more clearly from the inset of figure 4.6.

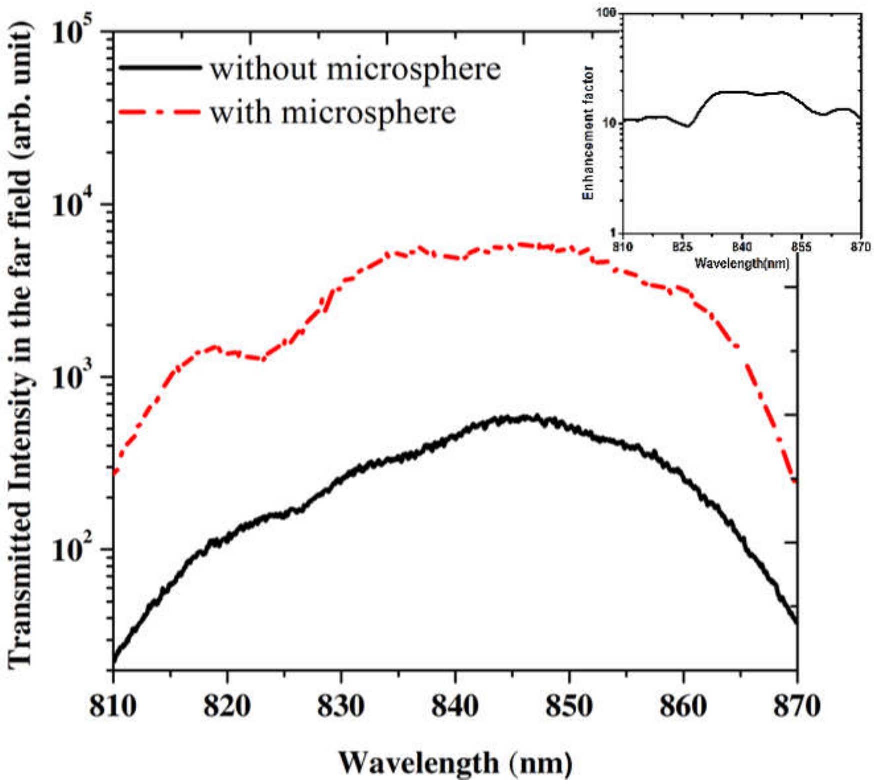

Figure 4-6 *Transmission spectra recorded from hollow pyramid shaped probe (black line) and from the probe with 5μm silica microsphere inserted. Inset shows the enhancement factor.*

The effect of axial and lateral displacement of the position of the beam waist with respect to the center of aperture probe on the throughput of the probe is shown in figure 4.7.

These results show that the modified probe not only shows enhanced transmission but the transmission through such tip is also relatively less sensitive to the axial and lateral offset between the beam waist and symmetry axis of the probe tip. Both of these advantages accrue from strong sub-diffraction confinement of electromagnetic field from dielectric microspheres in the form of photonic nanojet.

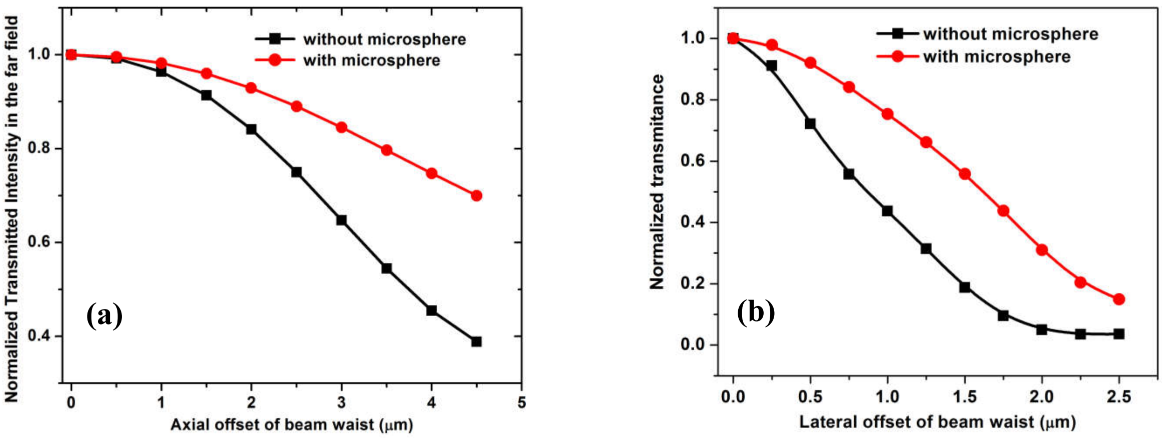

Figure 4-7 *Effect of axial (a) and lateral (b) position of beam waist on transmission through nano aperture with and without silica microsphere. Co-ordinate of the beam waist corresponding to maximum transmission was taken as origin of the abscissa. Filled circles are results of numerical simulation and solid lines have been drawn to guide the eye*

In figure 4.8 we show the near field optical transmission image of silver nanowire acquired using hollow cantilever based NSOM probe both with and without the 5 μm silica microsphere insert. The measurements were performed using a constant input power to probe as well as constant output intensity through the probe. The cross-sectional profiles of the corresponding transmitted intensity are also shown in the figures (Figure 4.8c, d). It can be seen from figure that while the resolution remain largely unaffected, there is a significant improvement in the contrast for the modified probe.

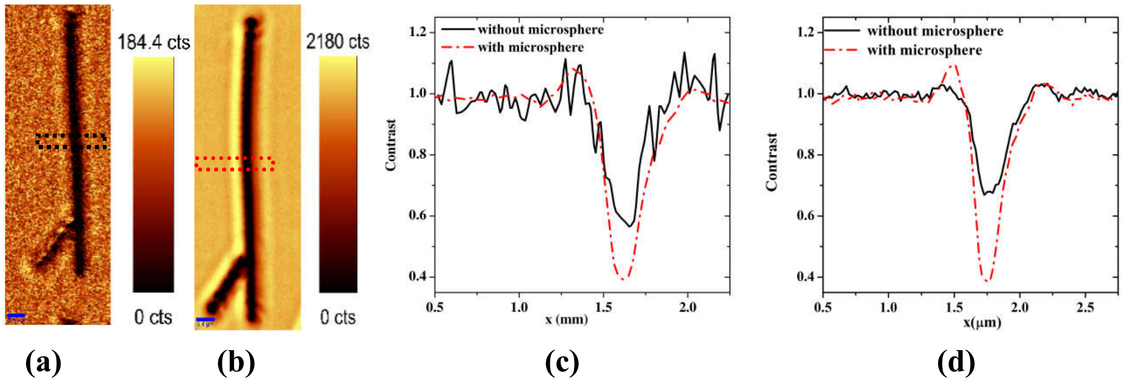

Figure 4-8 *Near field optical transmission image of silver nanowires acquired using hollow cantilever probe (a) without microsphere and (b) with 5 μm silica microsphere. The background normalized line profiles of the transmission through the marked area are shown in (c). The background normalized line profile in case of same intensity at detector is shown in (d). Scale bar: 400 nm*

Because the background light contribution due to leakage from probe, scattered light etc. reduce with a decrease in input intensity the observed improvement in the contrast can be attributed to the fact that for achieving same intensity at the detector for NSOM probe with no microsphere the input intensity has to be increased by a factor of ~ 10.

4.4 Conclusion

We have shown that the photonic nanojet formed by a microsphere inserted in the hollow probe of NSOM cantilever leads to an order of magnitude enhancement in the probe transmission. Further, the transmission through modified probe was also found to be less sensitive to the axial and lateral offset between the beam waist and symmetry axis of the probe tip. Such high throughput probes that can generate intense field at the apex of nano-apertures using the photonic nanojet may find applications in variety of near-field applications including nanolithography, imaging and spectroscopy with nano meter resolution, ultrahigh density data storage etc.

Chapter 5

High throughput polarization sensitive near field imaging using photonic nanojet

Polarization sensitive measurements in near field optical microscopy are required to gather information about plasmonic properties or the polarization response of metal nanostructures and meta-materials. Because near field imaging measurements are performed by raster scanning, polarization sensitive measurements would in general require imaging with multiple input polarization states to segregate different polarization effects. This approach suffers from large imaging time, probe degradation and system drift related errors that compromise the image quality and because of these issues making wavelength dependent measurements on polarization becomes even more difficult. In this chapter, we present a scheme for polarization sensitive near field imaging of nano-structured samples by making use of broadband polarized near field illumination and detection of polarization states of scattered light by spectrally encoded analyzer. The approach allows simultaneous measurement of polarization characteristics as well as spectral features of the nano-materials. The scheme was validated by measuring the near field polarization parameters of silver nanowires.

Work discussed in this chapter has resulted in the following publication:

1. *"Wavelength encoded polarization measurements for simultaneous spectral and polarimetric characterization in near field", H. S. Patel, M. K. Swami, P. K. Kushwaha, A. Uppal and P. K. Gupta, Journal of Optics 18, 085002 (2016).*

Introduction

Wavelength dependent measurements on polarization characteristics of nanostructures are required for studying polarization-sensitive mapping of the orientation of molecules and molecular aggregates on surfaces, magneto-optical Kerr effect, and optical reading and writing of information on photosensitive polymers with nanometer scale resolution. Near field scanning optical microscopy (NSOM) with hollow cantilever probes which are known to have a well-defined polarization state at probe tip are used for polarization sensitive imaging over a wide wavelength range. Because the near field imaging measurements are performed by raster scanning, these measurements require multiple image scan with different input polarization states to segregate the polarization effects [118]. Alternately a polarization modulator is used for continuously varying the input polarization state and lock-in detection of the scattered light to obtain polarization information at each pixel of the image [119, 120]. Both of these techniques suffer from large imaging time, probe degradation and system drift related errors that compromises the image quality.

To address this issue we have developed a simple approach utilizing wavelength encoding of polarization state to obtain simultaneous imaging of spectroscopic and polarization information from plasmonic nano-structures in a single image scan. The approach makes use of a linearly polarized broadband illumination from a super-continuum/super-luminescent diode source for excitation through the NSOM probe. The analyzer (comprising of a combination of a polarizer with pass axis oriented perpendicular to the input linear polarization, a multi-order waveplate and a broadband quarter waveplate) generates wavelength dependent analyzer states and functions like a linear analyzer with orientation varying with wavelength. The working of the scheme for near field polarization sensitive measurements has been demonstrated by imaging of silver nanowires. The scheme has potential for simultaneous characterization of plasmon resonance and polarization properties. The experimental results and theoretical simulations to comprehend these experimental findings are described in this chapter.

5.1 Materials and methods

5.1.1 Theory

The wavelength encoding of polarization can be implemented in two different ways. One of the approaches can be to use wavelength dependent input polarization states. In this case two combinations of polarization optics are possible (Figure. 5.1)

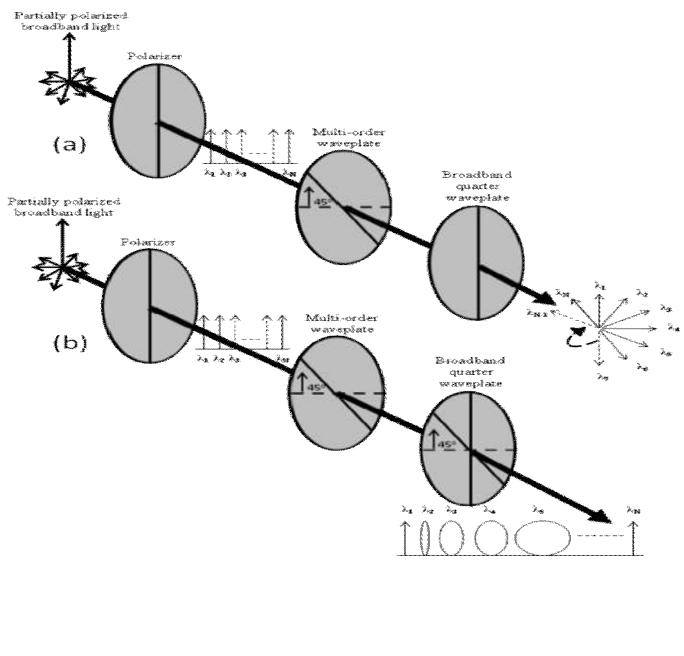

Figure 5-1 *Schematic arrangement of polarization optics used to generate different polarization states as a function of wavelength (a) linear polarization states with different orientations at different wavelength and (b) elliptical polarization states with at different wavelength.*

Mathematically the arrangement in figure 5.1(a) can be represented as:

$$S_o = M_{BQWP}(\delta = \pi/2, \theta = 0) M_{MWP}(\delta_1(\lambda), \theta_1 = \pi/4) M_{VP} S_I \tag{5.1}$$

where MBQWP is broadband quarter wave plate, MMWP is the multi-order waveplate (MWP) and MVP is the vertical polarizer. By solving the equation using the standard forms of the Mueller matrices the output stokes vector can be obtained in terms of wavelength dependent retardance of the MWP

$$S_o = \begin{bmatrix} 1 \\ \cos(\pi + \delta(\lambda)) \\ \sin(\pi + \delta(\lambda)) \\ 0 \end{bmatrix} \tag{5.2}$$

The Stokes vector represents a linear polarization state with an orientation given as

$$S_o = M_{BQWP}(\delta = \pi/2, \theta = \pi/4) M_{MWP}(\delta_1(\lambda), \theta_1 = \pi/4) M_{VP} S_I \tag{5.3}$$

Similarly for figure 5.1(b) the output stokes vector is given as:

$$S_o = \begin{bmatrix} 1 \\ \sin(\pi - \delta(\lambda)) \\ 0 \\ \cos(\pi - \delta(\lambda)) \end{bmatrix} \tag{5.4}$$

The Stokes vector in this case represents elliptically polarized light with its major axis along vertical or horizontal direction. While this approach allows exciting with different polarization states, a major difficulty is due to the polarization distortions caused by the NSOM cantilever which allow only the polarization states oriented along the edges of pyramid shaped tip to be maintained. To minimize this artifact we used wavelength encode analyzer combination. The Mueller matrix for the analyzer consisting of a broadband quarter waveplate followed by a 10 mm thick multi-order quartz waveplate and a liner polarizer with pass axis orthogonal to the input polarization state can be written as:

$$\boldsymbol{M_A} = \frac{1}{2}\begin{bmatrix} 1 & -1 & 0 & 0 \\ -1 & 1 & 0 & 0 \\ 0 & 0 & 0 & 0 \\ 0 & 0 & 0 & 0 \end{bmatrix}\begin{bmatrix} 1 & 0 & 0 & 0 \\ 0 & \cos\delta(\lambda) & 0 & -\sin\delta(\lambda) \\ 0 & 0 & 1 & 0 \\ 0 & \sin\delta(\lambda) & 0 & \cos\delta(\lambda) \end{bmatrix}\begin{bmatrix} 1 & 0 & 0 & 0 \\ 0 & 1 & 0 & 0 \\ 0 & 0 & 0 & 1 \\ 0 & 0 & -1 & 0 \end{bmatrix} \tag{5.5}$$

The analyzer state which is first row of the analyzer matrix M_A than becomes

$$\boldsymbol{S_A} = \frac{1}{2}[1 \quad -\cos\delta(\lambda) \quad -\sin\delta(\lambda) \quad 0] \tag{5.6}$$

This analyzer state corresponds to the linear polarization state given by following Stokes vector

$$\boldsymbol{S_I} = \begin{bmatrix} 1 \\ \cos\delta(\lambda) \\ \sin\delta(\lambda) \\ 0 \end{bmatrix} \tag{5.7}$$

i.e. $\mathbf{S_A . S_I = 0}$

It is interesting to note here that the orientation of the analyzer state generated by the combination of polarization optics is δ/2 which is a function of wavelength. A birefringent quartz crystal of thickness 10 mm was used in the analyzer optics for which the measured variation of retardance 'δ' with wavelength is shown in figure 5.2a. For a given input linear polarization state the spectral variation of the transmitted signal measured after the analyzer is shown in figure 5.2b. As expected, for linearly polarized light incident on the analyzer, the detector signal shows a periodic oscillations as a function of wavelength. It should be noted here that the envelope of the graph shown in figure 5.2b represents the transmission characteristics of the NSOM probe which is a convolution of the source spectrum and transmittance of the probe.

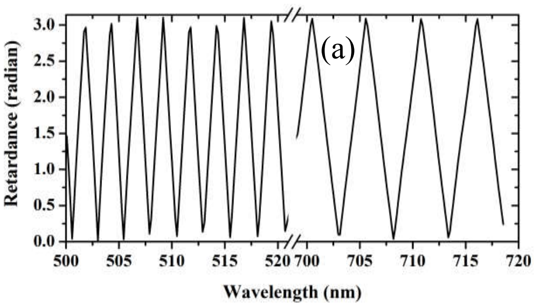

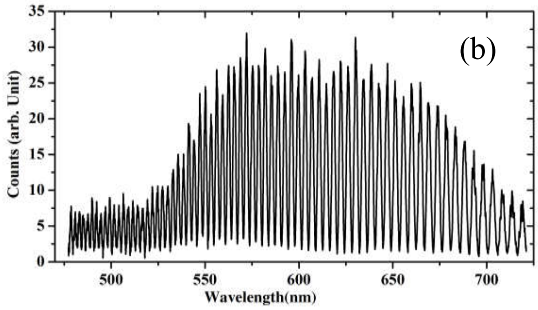

Figure 5-2 *(a) Variation of retardance δ of birefringent quartz crystal as a function of wavelength. (b) Measured signal at the detector for linearly polarized incident light at the back surface of hollow probe.*

The wavelength dependence of the intensity at the detector can be written as:

$$\boldsymbol{I}_{\mathbf{d}}(\lambda) = \boldsymbol{S}_A . \boldsymbol{S}_I = \frac{1}{2}\begin{bmatrix} 1 & -\cos\delta(\lambda) & -\sin\delta(\lambda) & 0 \end{bmatrix} . \begin{bmatrix} 1 \\ \cos\theta \\ \sin\theta \\ 0 \end{bmatrix} = \frac{1}{2}\left(1-\cos(\delta(\lambda)-\theta)\right)$$

(5.8)

It can be seen from equation 5.4 that the frequency of the oscillation in the measured signal follows the wavelength dependence of the retardance ‘δ’ of multi-order waveplate whereas the phase of the oscillations is determined by the orientation ‘θ’ of linear polarization at the output after the sample. For the more general case of an elliptically polarized light falling on the analyzer with stokes vector

$$\boldsymbol{S_I} = \begin{bmatrix} \mathbf{1} \\ \boldsymbol{a} \\ \boldsymbol{b} \\ \boldsymbol{c} \end{bmatrix}; \qquad \boldsymbol{a^2 + b^2 + c^2 = 1} \tag{5.9}$$

The intensity at the detector is given as:

$$\boldsymbol{I_d}(\lambda) = \boldsymbol{S_A}.\boldsymbol{S_I} = \frac{1}{2}\begin{bmatrix} 1 & -\cos\delta(\lambda) & -\sin\delta(\lambda) & 0 \end{bmatrix}.\begin{bmatrix} \mathbf{1} \\ \boldsymbol{a} \\ \boldsymbol{b} \\ \boldsymbol{c} \end{bmatrix}$$

$$= \frac{1}{2}\left(1 - \sqrt{(1-c^2)} * \cos(\delta(\lambda) - \varphi)\right)$$

where $\varphi = \tan^{-1}\left(\frac{b}{a}\right)$, (5.10)

In this case the depth of modulation at a given wavelength in the measured signal defined as reduces to:

$$\alpha = \frac{\sqrt{(1-c^2)}}{2 - \sqrt{(1-c^2)}} \tag{5.11}$$

The retardance of the sample can be determined from the measured depth of modulation using the following expression

$$\delta(\lambda)_{sample} = \cos^{-1}\left(\sqrt{1 - \frac{4\alpha^2}{1+\alpha}}\right) \tag{5.12}$$

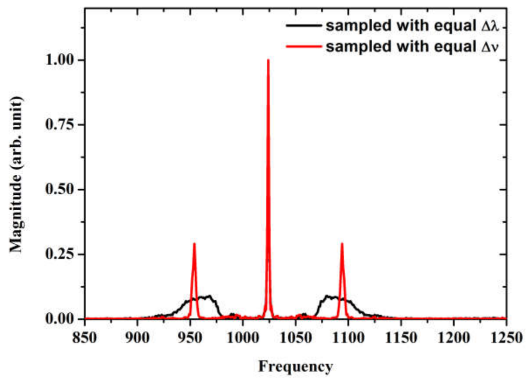

Figure 5-3 *Fourier transform of spectral data sampled at equal interval of wavelength (dashed line) and equal interval of wave-number (solid line).*

Further when intensity is plotted as a function of wavelength (equation 5.6) the frequency of the oscillation decrease with increase in wavelength. The varying frequency content of the signal results in a broad peak in Fourier transform spectra (Figure 5.3). Hence the accurate estimation of phase becomes difficult. To avoid this we first converted the data to wave-number space by re-sampling the data to make it equidistant in k-domain before performing the Fourier transformation.

It is pertinent to note that a rigorous analysis of the polarimetric properties of the sample using near field illumination would require development of appropriate methodologies for describing the three-dimensional nature of the near field excitation. Interpretation of the far field measurement would also require use of generalized Stokes-Mueller algebra that is valid for analyzing polarization response using near field illumination [121, 122]. Further, care has to be taken of the fact that the metal coated probe in proximity to the plasmonic sample can also modify the near field polarization. While these limitations are common to all near field polarimetric imaging techniques [118-120], the proposed approach offers the advantage that simultaneous spectral and polarization information can be acquired in single image scan.

5.1.2 Experimental

A schematic of the experimental setup used is shown in figure 5.4. Linearly polarized light from a super continuum source (WhiteLase, Short Wavelength Super-continuum Systems, Fianium, UK) was coupled to the NSOM system using single mode photonic crystal fiber. A combination of polarizer and half waveplate was used to control the polarization at the input. A 50X (0.55 NA) objective was used to couple the light to the NSOM probe. The light transmitted through the sample was collected using a 60X (0.6 NA) objective. The collimated output of the collection objective is than passed through a set of polarization optics for analyzing the polarization properties of transmitted light. The analyzer consists of a broad-band quarter wave-plate followed by a multi-order wave-plate (retardance of the wave-plate varying rapidly with the wavelength as shown in figure 5.2) and a polarizer crossed with respect to the input polarization state at the sample. The silver nanowires (AgNWs) used in the experiments were prepared using method described by Shobin et al [123]. For near field imaging, nanowire sample were prepared by drop casting ~20 μl sample from the AgNW solution on a cleaned microscopy cover glass.

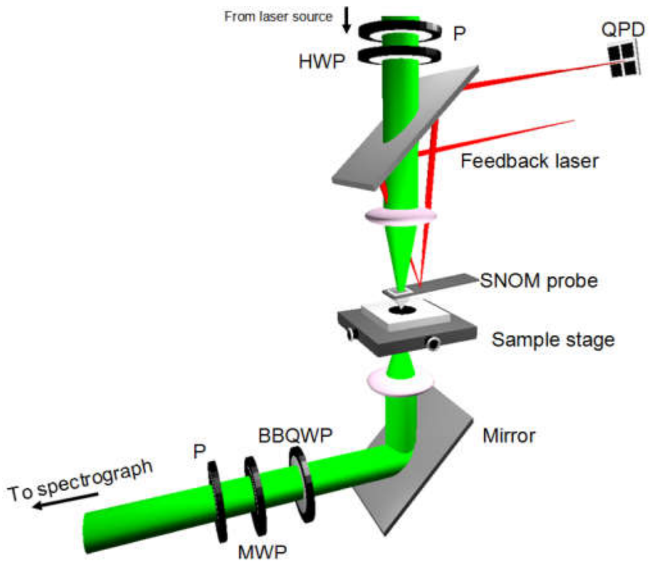

Figure 5-4 *A Schematic of the experimental setup. HWP: Half wave plate, P: Polarizer, QPD: Quadrant photo diode, MWP: Multi-order wave-plate and BBQWP: Broad-band quarter wave-plate.*

5.2 Results and discussion

To demonstrate working of the scheme for near field imaging we used silver nanowires as sample. In figure 5.5 we show the AFM image of silver nanowires. Near Field images were acquired from a number of regions in the sample. The images containing three nanowires in contact with each other but having different orientations were selected for further analysis. Nanowires are strongly di-attenuating due highly anisotropic shape. While the polarization perpendicular to the length (long axis) of the wires suffers no loss, the light with polarization parallel to their length is strongly attenuated [124]. Therefore choosing different orientations of nanowires would allow probing the effect of orientation dependent change in the phase of oscillations in the transmitted spectra. The retardance from metallic nano-structures usually originate as a consequence of interaction between multiple plasmon resonances excited by orthogonal polarizations [125,126]. While the large size of the wires ensures presence of multiple resonances, they are more pronounced at the joints.

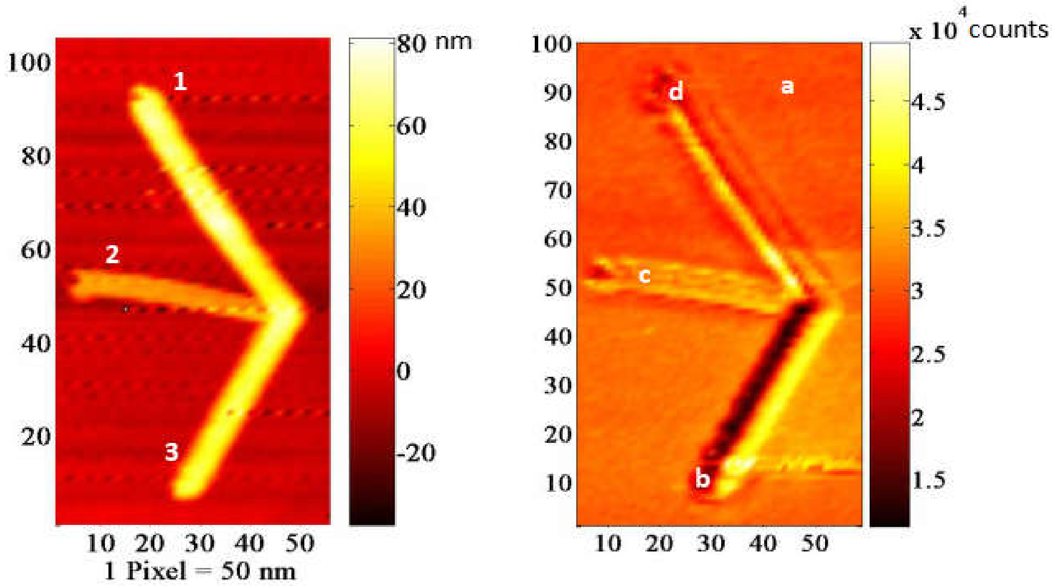

Figure 5-5 *AFM image of nanowire cluster (left) and corresponding integrated intensity NSOM image (right).*

From the atomic force microscopy image acquired for nanowire cluster (left panel of figure 5.5) the average height of the nanowire marked as '1' and '3' was estimated to be about 60nm and 70 nm respectively and for the wire marked as '2' the value was about 30 nm. The wires were ~ 2-3 µm in length and 250 nm wide. The corresponding integrated intensity NSOM image is shown in right panel of the figure 5.5.

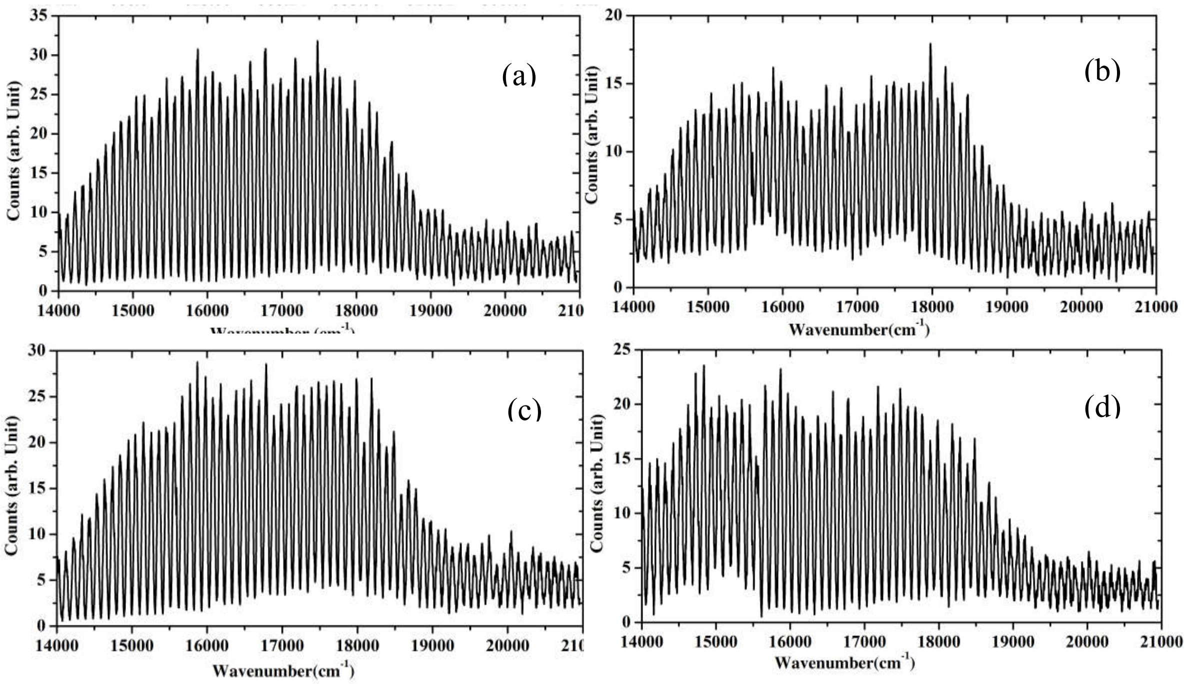

Figure 5-6 *Transmission spectra from different locations of the sample marked as 'a – d' in right panel of figure 5.5. The spectra were re-sampled with equal spacing in wave vector domain.*

Transmitted spectra recorded from different location marked 'a –d' in NSOM image are shown in figure 5.6. The transmission spectra from the wire cluster can be seen to show a strong wavelength dependence. The spectra for wire marked as '2' (Figure. 5.6c) is very similar to the source spectra (Figure. 5.6a). This may be due to the fact that because the thickness of the wire is small the transmission spectrum has a large contribution from the un-scattered light of the broad band illumination source. The lower contrast of the oscillations observed in the wavelength range of (~ 525-575 nm) is a signature of the retardance effect due to nanowire. The low contrast region shifts towards red as the height of the wires increases figure 5.6b and 5.6d. The spatial variation of retardance was computed (using equation 5.8) from the measured depth of modulation of the oscillation in the transmitted spectra at each location. The results are shown in figure 5.7. The retardation values shown for different wavelengths of scattered light were computed in narrow spectral range (± 2nm) around the central wavelength that is marked in the figure. Since the thicknesses of all three wires are different, it is expected that their SPR as well as polarization property will also show different wavelength dependence [127]. The wire denoted '2' in AFM image (Figure. 5.5) shows high retardance at ~ 540 nm and with increasing wavelength the retardance was observed to decrease (except near the tip and other isolated hot spots). In contrast the retardance value for wire '3' increases with wavelength and reaches to maximum around 670nm. For wire '1' which has the largest thickness the retardance values becomes significant only for wavelengths beyond ~700 nm. These observations are consistent with the reports in literature that the plasmon resonance in gold and silver nanowires shifts to lower energies with increase in the nanowire height [127, 128].

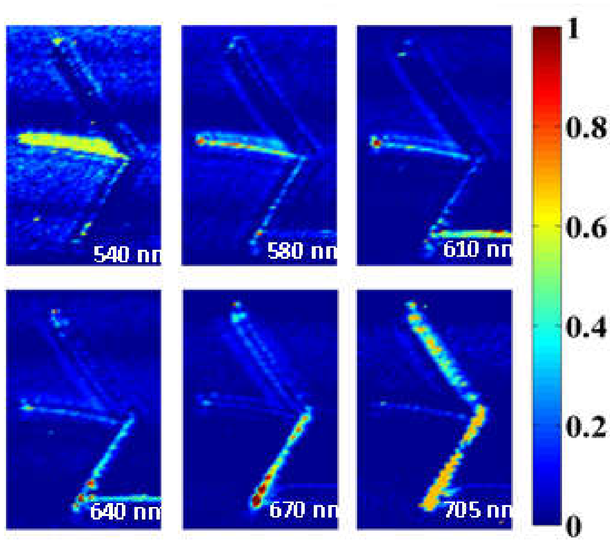

Figure 5-7 *Retardation maps computed for different wavelengths of scattered light.(Color bar is in unit of Radian).*

It is also pertinent to note that while interaction between different spectrally overlapping plasmonic modes of the sample would influence its polarization properties, previous work has shown that contribution of the normal dipole modes of plasmonic structures dominates and the effect of higher order modes is weak [129].

The measured phase change in spectral oscillations with respect to the glass substrate is shown in the figure 5.8. The orientation of the diattenuator could be calculated by computing the difference in the phase for point lying on the nanowires and the region containing only glass substrate. The blue region in figure 5.8 indicates the rod aligned to the incident polarization, while the red color indicates orientation closer to perpendicular.

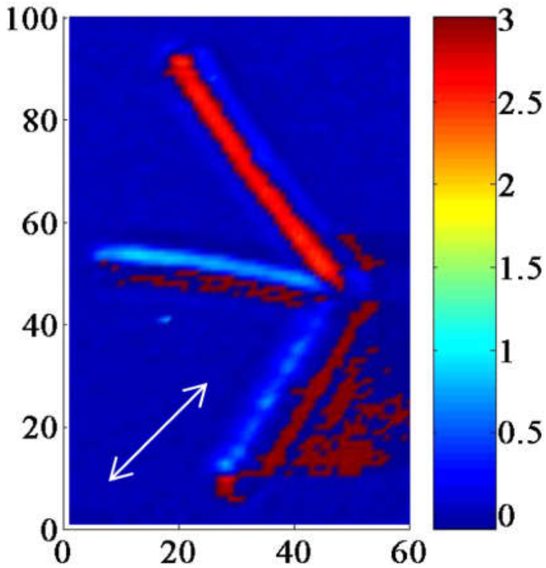

Figure 5-8 *Image of phase variation calculated from the measured transmitted signal from silver nanowire sample. The arrow indicates the polarization axis of the illumination source. (Color bars are in unit of Radian).*

5.3 Conclusion

A simple scheme for simultaneous measurement of spectral as well as polarization characteristics of nano structures using NSOM has been presented. The approach uses a broadband source for excitation of the sample and a multi-order waveplate followed by a polarizer for analyzing the scattered light transmitted through the sample. It has been shown that the oscillation in the measured spectra can be used to obtain the near field diattenuation and retardance properties of the nano structures from a single NSOM image scan. The scheme has been validated by demonstrating the imaging of retardance and diattenuation properties of silver nanowires.

Chapter 6

Photonic nanojet for enhancement of Raman signal

Several approaches are in use for the enhancement of the weak Raman signals. These include use of non-linear techniques like stimulated Raman scattering, coherent anti stokes Raman scattering (CARS), etc. or the use of local field enhancement using plasmonic processes. The use of local field enhancement in PNJ due to sub-wavelength confinement of light is also receiving much attention as it provides a much simpler and cost effective approach as compared to other techniques. Moreover, it can also be coupled with other approaches like CARS and SERS etc. for a synergistic enhancement of signal. In this chapter we present the results of our studies on the enhancement of Raman signal using photonic nanojet generated by a dielectric microsphere The enhancement was observed to strongly depend on the size of microsphere as well as the refractive index contrast between the sample and microsphere Higher the refractive index of sample vis-a-vis the microsphere, larger is the enhancement. The enhancement factor falls rapidly as the sample refractive index approaches that of the microsphere.

Work discussed in this chapter has resulted in the following publication:

1. *"Photonic nanojet assisted enhancement of Raman signal: Effect of refractive index contrast".*
   H. S. Patel, P. K. Kushwaha and M. K. Swami, J. Appl. Phys. 123, 023102 (2018).

6.1 Introduction

Raman spectroscopy is a powerful technique for the characterization of materials and provides molecular fingerprint of the analytes under investigation. However, due to poor cross-section (~10^{-30} - 10^{-28} cm^2) in visible and near infrared wavelength range Raman scattering is very weak. Several approaches have been investigated for enhancement of Raman signal. These include use of resonant Raman scattering, stimulated Raman scattering, coherent anti stokes Raman scattering (CARS), surface-enhanced Raman scattering (SERS), tip enhanced Raman scattering and photonic nanojet (PNJ) assisted Raman scattering etc. [130-138]. These techniques allow measurement of Raman signal from sample in different environments with varying degree of enhancement in signal and associated complexity in the instrumentation required. Among these, the enhancement of Raman signal obtained using PNJ generated by dielectric microsphere has received considerable attention since it provides the simplest and cost effective approach as compared to other techniques. Moreover, it can also be coupled with other approaches like CARS and SERS etc. for a synergistic enhancement of signal [135,139-141]. PNJ have been used to enhance the fluorescence signal for single molecule detection as well as to improve the axial and lateral resolution of the confocal imaging systems [17, 18, 142]. In case of bulk Si and other samples, the enhanced intensity in PNJ has also been exploited for Raman spectroscopy where an order of magnitude intense Raman signal have been reported by making use of self-assembled silica and polystyrene microspheres [39, 40, 143-145]. The microsphere assisted enhancement of Raman signal from ultra-thin film (thickness down to 5nm) of anatase and sub-nanomolar concentration of Methylene Blue has been reported by Alessandri et al. [146]. Chang et al. [41] reported a Raman enhancement factor of ~ 3.6×10^{10} by making use of photonic nanojet assisted Marangoni convection to increase the turnover of analytes in SERS hotspots. The confinement of light in photonic nanojet generated by dielectric microspheres is known to depend on refractive index and diameter of microsphere, the excitation wavelength etc. This has been investigated by Dantham et al [72] to understand the effect of refractive index and diameter of microspheres, numerical aperture of the objectives and excitation wavelength. A maximum enhancement by a factor of ~ 16 was reported for Si wafers by optimizing the laser spot size for illumination to match the diameter of sphere for 488 nm excitation wavelength. Though these studies demonstrated an order of magnitude enhancement of Raman signal from Si substrate and other high refractive index materials, no data exists on sample with lower refractive indices.

In this Chapter we present the results of our study on the use of PNJ generated by silica microsphere for enhancing Raman signal with varying refractive index contrast between the microsphere and substrate. The results show that the degree of enhancement is strongly dependent on the refractive index contrast between the microsphere and substrate. For a given size of microsphere, the enhancement was found to reduce with the refractive index of sample. Numerical simulations show that lower value of enhancement for substrate with low refractive index can be attributed to the elongation of PNJ in those samples. Elongation of PNJ leads to a lower enhancement value due to two factors (i) a reduction in the intensity of nanojet and (ii) poor collection of Raman signal from the elongated excitation volume in the back scattering confocal collection geometry. Based on these observations, we propose that PNJ assisted enhancement of Raman signal for samples with lower refractive index can be achieved by decoupling the optical path for excitation and collection to achieve better collection efficiency. The same has been validated experimentally by demonstrating an order of magnitude enhancement of Raman signal from low refractive index samples like Ru: LiNbO3, Sapphire and PMMA. This approach may find applications in enhancing Raman signal from biological samples for rapid identification of pathogens and tissue classification for early diagnosis of cancer etc.

6.2 Experimental details

6.2.1 Experimental methods

A schematic of the micro-Raman setup used in our experiments is shown in figure 6.1. Raman spectra of different samples were recorded using WiTec Alpha300SR Raman microscope (WiTec Instruments Germany) attached with Acton 2500i, (Princeton Instruments, USA) spectrograph with 600 line per mm grating. The laser lines used for excitation of samples were 442 nm He-Cd laser, 488 and 514.5 nm Ar-ion laser and 785 nm diode laser. Raman signal was collected in backscattering confocal geometry using a 20X; 0.4 NA objective unless stated otherwise. The backscattered light was passed through a notch filter to remove the contribution from Rayleigh scattering and was coupled to a CCD-spectrograph using a 100 μm diameter multimode fiber which also served as confocal pinhole. A TE cooled (- 72^{o}C) CCD (ANDOR 420BR DD) was used for recording the spectra. Dilute suspension of silica microspheres (Duke scientific, USA) was drop casted on the sample surface and allowed to dry in ambient environment. Raman spectra was recorded from at least 10 microspheres for each sample.

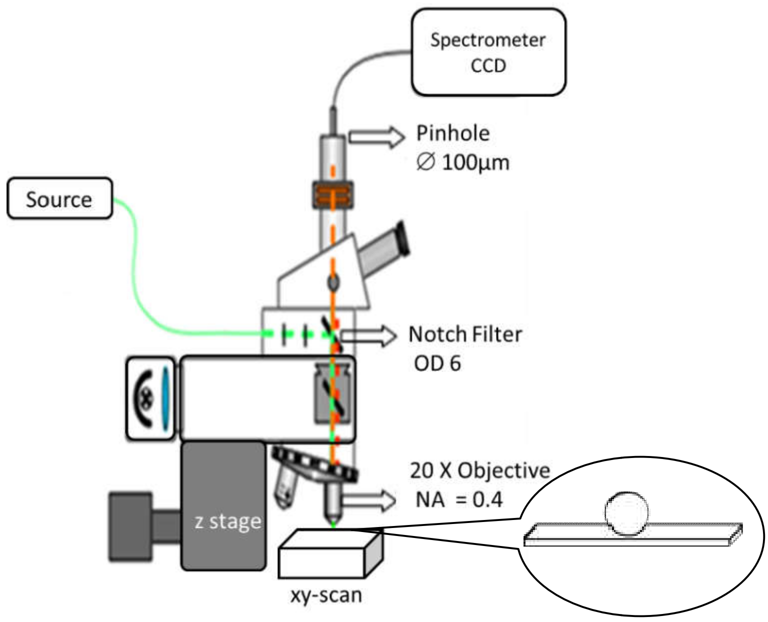

Figure 6-1 *A schematic of the experimental setup.*

Numerical simulations were performed by solving Maxwell's equation using the finite element method based commercial software COMSOL Multiphysics 4.2. Since the experimental measurements involve illumination with focused Gaussian beam the standard plane wave illumination used in COMSOL script for solving scattered harmonic propagation was suitably modified [81]. The propagation direction was taken to be along the 'x' axis of coordinate system and electric field vibration of the incident polarized light was along 'z' axis. Spatial evolution of electric field was modelled using standard Gaussian beam propagation as

$$E(x,y) = E_0\sqrt{\frac{\omega_0}{\omega(x)}}\, e^{-(y/\omega(x))^2}\cos\left(-kx+\eta(x)-\frac{ky^2}{2R(x)}\right) \quad (6.1)$$

where $\omega(x)$, $\eta(x)$ and $R(x)$ are the beam radius as a function of x, the Gouy phase and the radius of curvature of the wavefront respectively and defined as:

$$\omega(x) = \omega_0\sqrt{1+\left(\frac{x}{x_0}\right)^2}\ ;\ \eta(x) = \frac{1}{2}atan\left(\frac{x}{x_0}\right)\ and\ R(x) = x\left(1+\left(\frac{x_0}{x}\right)^2\right);$$

with $x_0 = \frac{\pi\omega_0^2}{\lambda}$ being the Rayleigh range

All simulations were carried out using direct solver for computing the field. To ensure convergence, the mesh size was refined until variation in the computed field at any given point is $<10^{-5}$.

6.3 Results and discussion

Raman imaging of different samples was carried out with the microspheres of varying size placed on the sample surface. In figure 6.2 we show typical Raman image and Raman spectra recorded from different locations of silicon substrate which had a monolayer of 5µm diameter SiO_2 microspheres dispersed on its surface. It can be seen from the figure that intensity of the Raman peaks in spectra recorded through the microsphere is about an order of magnitude higher as compare to that from the direct excitation of the substrate

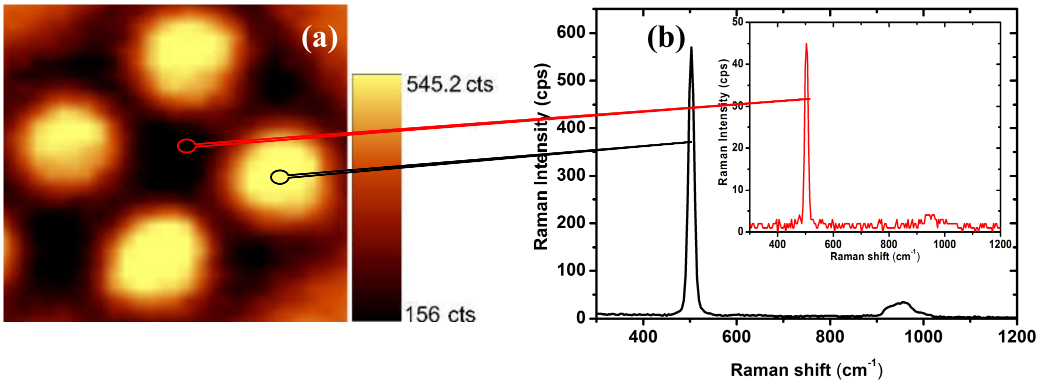

Figure 6-2 *Raman signal enhancement using photonic nanojet from a 5μm SiO_2 microsphere placed on Si substrate. (a) Raman image corresponding to 520 cm^{-1} Raman shift of Si, and (b) Raman spectra of Si substrate from regions marked in Raman image. The measurements were performed with 442nm He-Cd laser.*

In figure 6.3a, we show size dependence of the enhancement ratio (ER) defined as the ratio of Raman intensity from Si substrate with and without silica microsphere. The measurements were carried out with 50X; 0.55 NA objective using 488 nm excitation. The maximum enhancement was obtained for microsphere of the size ~ 3 - 4 μm. This is consistent with the simulated field distribution of PNJ which shows highest intensity at the microsphere-sample interface for microspheres with size in the range 3 - 4 μm (Figure 6.3 b-d). It is pertinent to note here that this observation is in contrast with the results reported by Dantham et al [72] where the ER has been shown to increase with microsphere diameter. This discrepancy can be understood by realizing the fact that in their experiment the measurements were performed by varying the distance between microscope objective and sample such that the microsphere is fully illuminated.

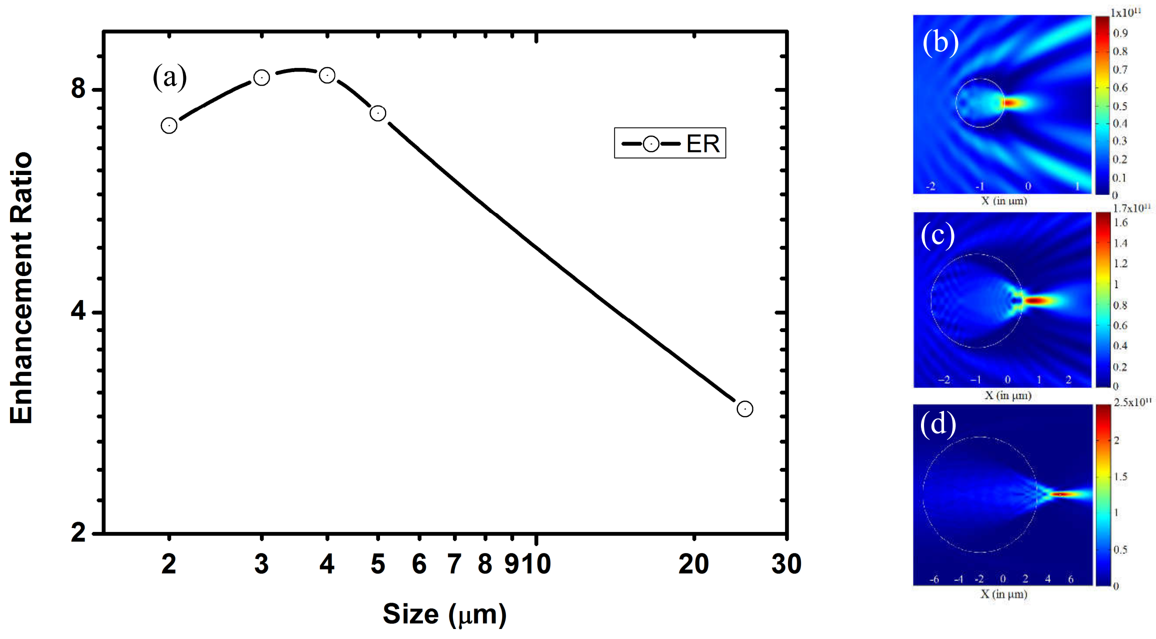

Figure 6-3 *(a) Dependence of Raman signal enhancement ratio on the size and the simulated field of photonic nanojet for 1 μm, 3 μm and 10 μm size of silica (n = 1.46) microspheres (b, c & d respectively). The excitation wavelength was 488 nm.*

Therefore, as the size of microsphere increases the focus of the microscope objective/lens needs to be moved farther away from sample to ensure that microsphere is fully immersed in the diverging beam. This leads to a reduction in the collection of Raman signal from microsphere free region thereby leading to an artificial increase in the enhancement ratio. In our study we have varied the sample to objective distance in such a manner that the maximum signal is recorded in both the cases i.e. with and without microspheres.

We have also carried out investigations on the dependence of enhancement ratio on the refractive index contrast (RIC) between the microsphere and sample. For a given microsphere, this can be studied either by making measurements on different substrate material with a fixed excitation wavelength or by varying the excitation wavelength to utilize the material dispersion of the substrate. The latter approach allows measurement with the same microsphere and sample in addition to the investigation of wavelength dependence of enhancement factor. It should be noted here that while the refractive index of silica microsphere varies marginally (1.46 - 1.45), the refractive index of silicon changes significantly (4.8-3.7) on varying the excitation wavelength from 442 nm to 785 nm. Figure 6.4a shows the measured Raman spectra from silicon substrate for different excitation wavelength. It can be seen from the figure that the observed ER decrease monotonically with decrease in refractive index contrast i.e. with increase in the excitation wavelength. The dependence of the enhanced ratio on refractive index contrast measured using silicon (Si), Ruthenium doped Lithium Niobate (Ru:LN) and Poly(methyl methacrylate) (PMMA) substrates is shown in figure 6.4b.

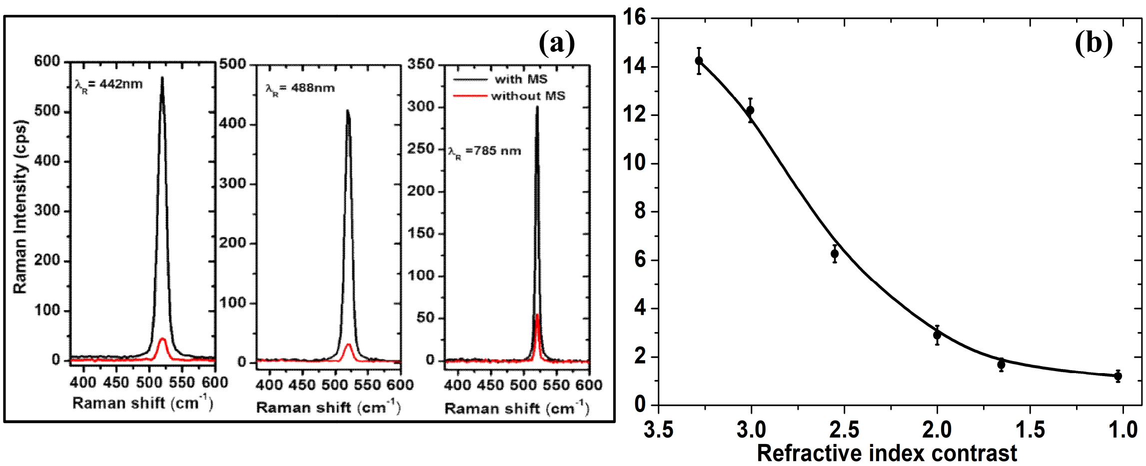

Figure 6-4 *(a) Wavelength dependence of the Raman signal enhancement from silicon substrate. (b) Variation of enhancement factor with change in refractive index contrast between microsphere and substrate.*

It is important to note here that the effective volume of photonic nanojet exhibits $(\lambda_0/n)^3$ dependence on the wavelength in the substrate medium [75], where λ_0 is free space wavelength and 'n' is the refractive index of medium. One would therefore expect that the excitation with shorter wavelength will lead to a higher ER because of better confinement of light with a commensurate increase in the intensity of photonic nanojet. Further, for a given confocal pinhole, shorter wavelengths will allow better collection of Raman signal due to smaller excitation volume. The measured enhancement ratios for silicon substrate upon excitation with different wavelengths are presented in table 6.1. It can be seen from the table that contrary to the expected λ^{-3} dependence the relative enhancement roughly scales linearly with inverse of the ratio of the corresponding wavelengths in substrate medium.

Table 6-1 *Dependence of the relative enhancement of Raman signal on the wavelength in silicon substrate.*

Free space wavelength and refractive index of Si [147]	**Enhancement Ratio**	**Ratio of wavelengths in substrate (Si)**	**Relative enhancement (Experimental)**
λ_1 = 442nm, n_1= 4.7639; k_1 = 0.16509	$ER_{\lambda 1}$= 14.28	$\frac{\lambda_2}{n_2} \times \frac{n_1}{\lambda_1} = 1.20$	$\frac{ER_{\lambda 1}}{ER_{\lambda 2}}$ =1.17
λ_2 = 488nm, n_2 = 4.3707; k_2 = 0.08007	$ER_{\lambda 2}$ = 12.20	$\frac{\lambda_3}{n_3} \times \frac{n_2}{\lambda_2} = 1.90$	$\frac{ER_{\lambda 2}}{ER_{\lambda 3}}$ =1.95
λ3 = 785nm, n3=3.7060; k_3 = 0.00741	$ER_{\lambda 3}$ = 6.27	$\frac{\lambda_3}{n_3} \times \frac{n_1}{\lambda_1} = 2.28$	$\frac{ER_{\lambda 1}}{ER_{\lambda 3}}$ =2.28

To understand this intriguing observation, we carried out detailed simulations for field distribution of PNJ excited with different wavelengths (Figure 6.5 a-c). It can be seen from figure 6.5 that the length of PNJ increases with wavelength. The elongated PNJ for a given substrate leads to a lower enhancement value due to two factors (i) a reduction in the intensity of nanojet at microsphere - sample interface and (ii) poor collection of Raman signal from the elongated excitation volume in the back scattering confocal geometry.

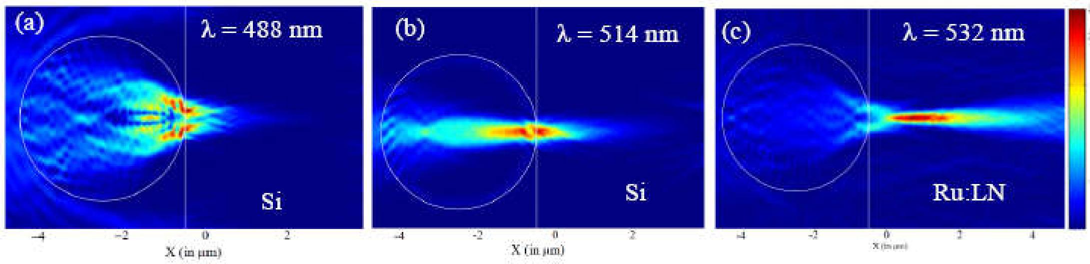

Figure 6-5 *The simulated field of photonic nanojet generated by 4 μm SiO2 microsphere placed on silicon substrate (a and b) and on z-cut Ruthenium doped Lithium Niobate (Ru:LN) crystal (c). Refractive index values for Si and Ru:LN were taken from references 147 and 148 respectively.*

While the microsphere placed on the substrate helps in efficiently concentrating the light to sub-wavelength dimensions, it should also efficiently collect the scattered signal by the virtue of reciprocity. However because of the isotropic angular distribution, only a small fraction of Raman scattered light is collected. When the peak intensity in PNJ moves to a larger depth inside the sample, which is the case with substrates having smaller RIC, this fraction is further reduced resulting in an overall reduction of the enhancement factor due to confocal geometry [149, 150].

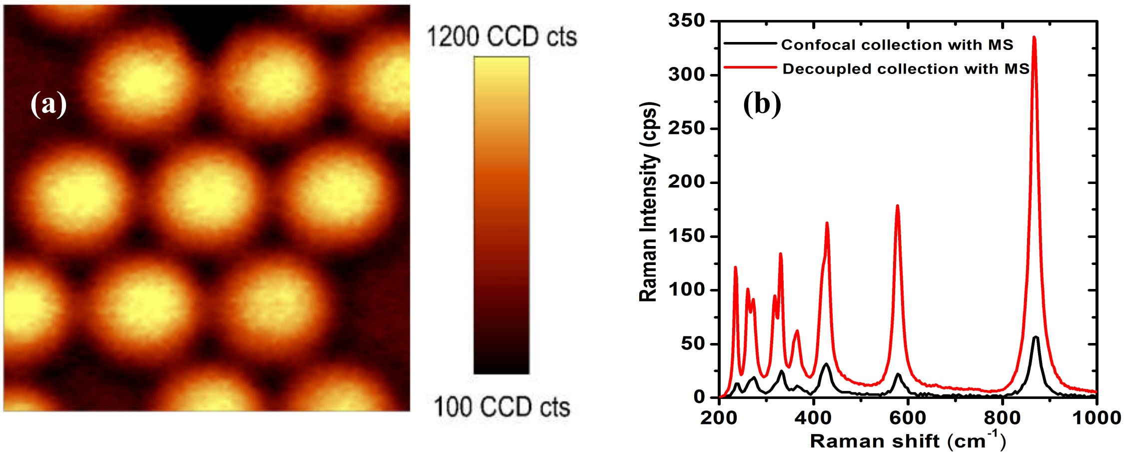

Figure 6-6 *Raman image of Ru: $LiNbO_3$ crystal corresponding to 872 cm^{-1} (a) and Raman spectra recorded in decoupled excitation collection geometry (b). The PNJ was generated by 10 μm silica microsphere dispersed on the top surface and illuminated with 514.5 nm Ar ion laser.*

We explored the possibility of decoupled excitation and collection geometry to collect the Raman signal from the peak intensity region of photonic nanojet in low index samples like Ru doped Lithium Niobate (Ru:LN) crystal (n_o ~2.33) [148], Sapphire (n =1.7) and PMMA (n = 1.49) samples. Raman spectra recorded from z-cut Ru:LN crystal in confocal collection geometry and the decoupled excitation-collection geometry are shown in Figure 6.6a. Raman image corresponding to 872 cm^{-1} line of the Ru:LN crystal recorded in decoupled geometry is shown in figure 6.6b. It can be seen from the figure that under identical illumination conditions the decoupled geometry leads to a higher enhancement ratio. This was achieved by mounting the confocal pinhole on a micro-positioner that allows moving the pinhole along the beam path to enable optimal collection from the peak intensity region of photonic nanojet. Similar results were obtained with sapphire and

PMMA samples. These results show that in the decoupled excitation-collection geometry, it is possible to achieve an order of magnitude enhancement of Raman signal from low index substrates.

6.4 Conclusion

To conclude, the results of our studies on the enhancement of Raman signal using PNJ show that the enhancement is strongly dependent not only on the size of microsphere but also on the refractive index contrast between the sample and microsphere. The maximum enhancement is obtained when the peak intensity in PNJ is near the sample-microsphere interface. The enhancement falls with a reduction in the refractive index contrast between the sample and microsphere. We have further shown that by decoupling the excitation and collection, it is possible to achieve an order of magnitude enhancement of Raman signal even from the samples having lower refractive where PNJ are quite elongated. The use of microsphere assisted enhancement of Raman signal can therefore be a useful aid in label free analysis of the biological samples. It may also permit recording spectra selectively from the different regions of cell by controlling the nanojet characteristics. The nanojet assisted enhancement of Raman signal can also be coupled with other technique like SRS, CARS and plasmonic enhancement of the field for possible single molecule detection and imaging.

Chapter 7

Conclusion

We have presented in this thesis, results of the studies carried out by us on ways to control the characteristics of PNJs and the use of these for near field imaging and spectroscopy applications. The numerical simulations carried out by us showed that using eccentric core-shell microsphere and with appropriate choice of the size and refractive index of the core and shell it is possible to generate either highly elongated nanojet (length ~27λ) or a very narrow (FWHM ~ λ/6) nanojet. The crescent structure formed when core and shell microsphere centres are offset by the difference between their radiuses has been shown to have the most prominent effect on PNJ characteristics. Our studies on the use of PNJ for near field imaging and spectroscopy applications have shown that PNJ generated by the placement of a dielectric microsphere in the NSOM aperture probe leads to an order of magnitude enhanced in its transmission and thus allows imaging near field imaging with better signal to noise ratio. The enhanced transmission also allowed us to couple multiple laser lines with different polarization states to probe the spectral and polarization response of nano-structures simultaneously. We also investigated the use of highly confined field in photonic nanojet for the enhancement of Raman signal from the substrate underneath. The enhancement was observed to strongly depend on the size of microsphere as well as the refractive index contrast between the sample and microsphere. Under optimum conditions an enhancement by an order of magnitude was observed.

7.1 Future Perspectives:

The range of applications of PNJ is expanding. Over the last few years several interesting applications of PNJ have emerged in the field as diverse as inspection and cleaning of the wafers for nano-fabrication to nanoscopy of ultra-structures in biological cells. So far the generation of PNJs was limited to the use of dielectric materials of relative refractive index less than 2 compared with surrounding medium. In a recent report it has been shown that materials with refractive index contrast beyond 2:1 between the micro-particles and surrounding medium can also be used with structured beam illumination. This should allow even more control on the characteristics of PNJs and thus help in expanding their range of applications. In particular it would appear worthwhile to investigate their use for super resolution imaging and spectroscopy.

Appendix A

```
' ========= Parameter file for v7.1 ==================='

'NOTORQ' = CMTORQ*6 (NOTORQ, DOTORQ) -- either do or skip torque
calculations
'PBCGS2' = CMDSOL*6 (PBCGS2, PBCGST, PETRKP) -- select solution
method
'GPFAFT' = CMDFFT*6 (GPFAFT, FFTMKL) -- select FFT method
'GKDLDR' = CALPHA*6 (GKDLDR, LATTDR) -- select prescription for
polarizabilities
'NOTBIN' = CBINFLAG (NOTBIN, ORIBIN, ALLBIN) -- specify binary
output
'**** Initial Memory Allocation ****'
180 180 180 = dimensioning allowance for target generation
'**** Target Geometry and Composition ****'
'FROM_FILE' = CSHAPE*9 shape directive
30 30 30  = shape parameters 1 - 3
1         = NCOMP = number of dielectric materials
'/home2/harish/ddscat301/diel/DEFORMEDSPH5.txt' = file with
refractive index 1'
'**** Error Tolerance ****'
1.00e-5 = TOL = MAX ALLOWED (NORM OF |G>=AC|E>-ACA|X>)/(NORM OF
AC|E>)
'**** Interaction cutoff parameter for PBC calculations ****'
1.00e-2 = GAMMA (1e-2 is normal, 3e-3 for greater accuracy)
'**** Angular resolution for calculation of <cos>, etc. ****'
0.5   = ETASCA (number of angles is proportional to
[(3+x)/ETASCA]^2 )
'**** Wavelengths (micron) ****'
0.350 0.800 100   'LIN' = wavelengths (first,last,how
many,how=LIN,INV,LOG)
'**** Effective Radii (micron) **** '
2.18 2.18 1 'LIN' = aeff (first,last,how many,how=LIN,INV,LOG)
'**** Define Incident Polarizations ****'
(0,0) (1.,0.) (0.,0.) = Polarization state e01 (k along x axis)
2 = IORTH  (=1 to do only pol. state e01; =2 to also do orth.
pol. state)
'**** Specify which output files to write ****'
1 = IWRKSC (=0 to suppress, =1 to write ".sca" file for each
target orient.
1 = IWRPOL (=0 to suppress, =1 to write ".pol" file for each
(BETA,THETA)
'**** Prescribe Target Rotations ****'
0.    0.   1  = BETAMI, BETAMX, NBETA  (beta=rotation around a1)
```

```
0.    0.   1  = THETMI, THETMX, NTHETA (theta=angle between a1
and k)
0.    0.   1  = PHIMIN, PHIMAX, NPHI (phi=rotation angle of a1
around k)
'**** Specify first IWAV, IRAD, IORI (normally 0 0 0) ****'
0   0   0    = first IWAV, first IRAD, first IORI (0 0 0 to begin
fresh)
'**** Select Elements of S_ij Matrix to Print ****'
9     = NSMELTS = number of elements of S_ij to print (not more
than 9)
11 12 13 14 21 22 23 24 31 = indices ij of elements to print
'**** Specify Scattered Directions ****'
'LFRAME' = CMDFRM (LFRAME, TFRAME for Lab Frame or Target Frame)
2 = NPLANES = number of scattering planes
0.   0. 180.  0.1 = phi, thetan_min, thetan_max, dtheta (in deg)
for plane 1
90.  0. 180.  0.1 = phi, thetan_min, thetan_max, dtheta (in deg)
for plane 2
```

The output files generated upon execution of code are written in the form of wxxxryyy*.* file. A typical output file containing the results for the first wavelength (w000), first target radius (r000), and first orientation (k000) is named w000r000k000.sca and contains all necessary input details as well as the output data

```
>REAPAR  ========= Parameter file for v7.1 ===================
 >  **** Preliminaries ****
 >REAPAR NOTORQ - do not compute torques
 >REAPAR PBCGS2 - CCG Method
 >REAPAR GPFAFT - using GPFA package from Clive Temperton
 >REAPAR GKDLDR - Gutkowicz-Krusin & Draine (2004) LDR for alpha
 >REAPAR NOTBIN - Unformatted binary dump option
 >REAPAR **** Initial Memory Allocation ****
 >REAPAR allow MXNX,MXNY,MXNZ=   180   180   180 for target
generation
 >REAPAR **** Target Geometry and Composition ****
 >REAPAR FROM_FILE - Shape definition
 >REAPAR  NCOMP=   1
 >REAPAR  1 /home2/harish/ddscat301/diel/DEFORMEDSPH5.txt
 >REAPAR **** Error Tolerance ****
 >REAPAR  1.000E-05 = TOL = max. acceptable normalized residue
|Ax-E|/|E|
 >  **** Interaction cutoff parameter for PBC calculations ****
 >REAPAR [GAMMA is not used in present calculation]
 >  **** Angular resolution for calculation of <cos>, etc. ****
```

```
 >REAPAR  0.5000 = ETASCA (parameter controlling number of
scattering angles
 >  **** Wavelengths (micron) ****
 >REAPAR 100 wavelengths from  0.3500 to  0.8000
 >  **** Effective Radii (micron) ****
 >REAPAR   1 eff. radii from  2.1800 to  2.1800
 >DIVIDE  Only one element initialized
 >  **** Define Incident Polarizations ****
 >REAPAR IORTH= 2
 >REAPAR **** Specify which output files to write ****
 >REAPAR IWRKSC= 1
 >REAPAR IWRPOL= 1
 >  **** Prescribe Target Rotations ****
 >  **** Specify first IWAV, IRAD, IORI (normally 0 0 0) ****
 >REAPAR Do orthogonal polarization for each case
 >REAPAR    0.00   0.00 Range of BETA values ; NBETA =   1
 >REAPAR    0.00   0.00 Range of THETA values; NTHETA=   1
 >REAPAR    0.00   0.00 Range of PHI values ;   NPHI =   1
 >  **** Select Elements of S_ij Matrix to Print ****
 >REAPAR **** Specify Scattered Directions ****
 >REAPAR     0.0    0.0  180.0 = phi, theta_min, theta_max for
scatt. plane   1
 >REAPAR 1801 = number of scattering angles in this scattering
plane
 >REAPAR    90.0    0.0  180.0 = phi, theta_min, theta_max for
scatt. plane   2
 >REAPAR 1801 = number of scattering angles in this scattering
plane
 >DDSCAT Allocate memory for first call to TARGET...
 >DDSCAT allocating    33.37 MB for IXYZ0;  total=    69.23 MB
 >DDSCAT allocating    33.37 MB for ICOMP;  total=   102.60 MB
 >DDSCAT allocating    11.12 MB for IOCC;   total=   113.72 MB
 >DDSCAT allocating    33.37 MB for ISCR1;  total=   147.09 MB
 >DDSCAT allocating    22.25 MB for BETADF; total=   169.34 MB
 >DDSCAT allocating    22.25 MB for PHIDF;  total=   191.59 MB
 >DDSCAT allocating    22.25 MB for THETADF;total=   213.84 MB
 >DDSCAT allocating    22.25 MB for SCRRS2; total=   236.08 MB
 >REASHP about to open shape file=
>REASHP CFLSHP=
 >REAHSP shape.dat
 >REASHP  requires  1 different refractive index files
 >REASHP  requires  1 different refractive index files
 >TARGET:> DEFORMEDSPH5_final_spike: NBX, NBY, NBZ= 144  74 150
        306600 = NAT0 = number of dipoles in target
 >DDSCAT returned from TARGET:
 >DDSCAT    -65    65 = min, max values of JX
 >DDSCAT    -68    67 = min, max values of JY
 >DDSCAT    -33    33 = min, max values of JZ
 >DDSCAT    0.00000   0.00000   0.00000 = X0(1-3)
 >DDSCAT  --- physical extent of target volume (occupied sites)
```

```
 >DIELEC /home2/harish/ddscat301/diel/DEFORMEDSPH5.txt
 >DIELEC DEFORMEDSPH5 w.r.t.medim=1.33 final spiked
 >DIELEC  completed reading file =
 >DIELEC /home2/harish/ddscat301/diel/DEFORMEDSPH5.txt
 m= ( 1.1572 , 0.0009),  epsilon= (  1.3391 ,  0.0020)  for
material 1
    2.180000 = AEFF = effective radius (physical units)
    0.023906 = d/aeff for this target
    0.350000 = WAVE = wavelength (physical units)
   39.135273 = k*aeff = 2*pi*aeff/lambda
    0.935565 = k*d
 >ALPHA  GKDLDR Lattice dispersion relation for |m|k_0d=1.0826
 >DIRECT_CALC Estimated total cputime required by DIRECT_CALC=
……
……
```

Appendix B

Abridged report generated by COMSOL Multiphysics depicting the steps involved in modeling the simulation.

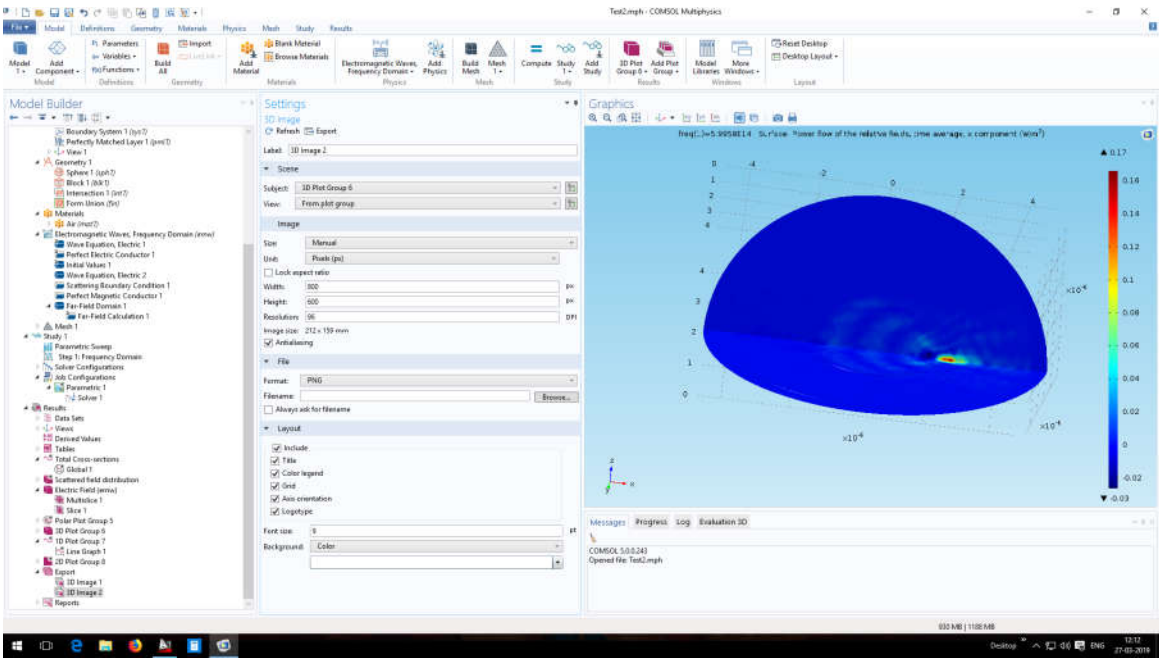

Global Definitions

Parameters 1

Parameters

Name	Expression	Description
r0	1500[nm]	Sphere radius
lda	500[nm]	Wavelength
f0	c_const/lda	Frequency
t_air	10*lda	Thickness of air around sphere
t_pml	1*lda	Thickness of PML shell

Name	Expression	Description
h_max	lda/10	maximum mesh element size in air
E0	1[V/m]	
S_in	E0^2/(2*Z0_const)	
sigma_geom	pi*r0^2	

Model 1 (mod1)

Definitions

scPoav	emw.relPoavx*onx + emw.relPoavy*ony + emw.relPoavz*onz
Poav	emw.Poavx*onx + emw.Poavy*ony + emw.Poavz*onz
ECS_OT	-4*pi/emw.k0*int_OT(imag(emw.Efarz*1[m]))/E0
ACS	4*int_ACS(emw.Qrh)/S_in
SCS	4*int_SCS(scPoav)/S_in
ECS	ACS + SCS
r	sqrt(x^2 + y^2 + z^2)
dSCS_far	(emw.normEfar^2/(r/1[m])^2)/abs(E0)^2*r^2
RCS	4*pi*int_BS(dSCS_far)

Domain Properties

Perfectly Matched Layer 1

Identifier	pml1
Geometric entity level	Domain
Selection	Domains 1, 5

Geometry

Settings

Name	Value
Center coordinate	{0, 0, 0}
Typical wavelength from	Physics interface

Name	Value
Physics	Electromagnetic Waves, Frequency Domain

Equations

$$\nabla \times \mu_r^{-1}(\nabla \times \mathbf{E}) - k_0^2\left(\epsilon_r - \frac{j\sigma}{\omega\epsilon_0}\right)\mathbf{E} = \mathbf{0}$$

Settings

Description	Value
Solve for	Scattered field
Background electric field	{0, 0, E0*exp(j*emw.k0*x)}

Used products

COMSOL Multiphysics

RF Module

Wave Equation, Electric 1

Selection

Geometric entity level	Domain
Selection	Domains 1–2, 4–5

Properties from material

Property	Material	Property group
Relative permittivity	Air	Basic
Relative permeability	Air	Basic
Electrical conductivity	Air	Basic

Selection

Geometric entity level	Boundary
Selection	Boundaries 2, 5, 9, 17–18

$$\mathbf{n} \times \mathbf{E} = \mathbf{0}$$

Scattering Boundary Condition 1

Scattering Boundary Condition 1

Selection

Geometric entity level	Boundary
Selection	Boundaries 3, 16

$$\mathbf{n} \times (\nabla \times (\mathbf{E} + \mathbf{E}_b)) - (jk + 1/r)\mathbf{n} \times (\mathbf{E} \times \mathbf{n}) = 0$$

Settings

Description	Value
Wave type	Spherical wave
Wave direction	{((nx)), ((ny)), ((nz))}

Wave Equation, Electric 2

Wave Equation, Electric 2

Selection

Geometric entity level	Domain
Selection	Domain 3

$$\nabla \times \mu_r^{-1}(\nabla \times \mathbf{E}) - k_0^2(\epsilon_r - \frac{j\sigma}{\omega\epsilon_0})\mathbf{E} = \mathbf{0}$$

Description	Value
Relative permittivity	User defined
Relative permittivity	{{2.52, 0, 0}, {0, 2.52, 0}, {0, 0, 2.52}}

Mesh 1

Mesh statistics

Property	Value
Minimum element quality	0.1886
Average element quality	0.7813
Tetrahedral elements	1169079
Prism elements	59180
Triangular elements	44431
Quadrilateral elements	1550
Edge elements	945
Vertex elements	12

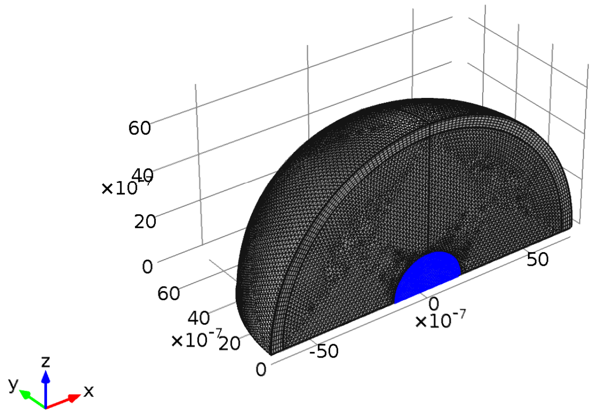

Mesh 1

Size (size)

Settings

Name	**Value**
Maximum element size	h_max
Minimum element size	2.8E9
Resolution of curvature	0.2
Maximum element growth rate	1.3
Predefined size	Extremely fine
Custom element size	Custom

References

[1] J. W. P. Hsu, "Near-field scanning optical microscopy studies of electronic and photonic materials and devices," *Mat. Sci. Eng. R: Reports,* vol. 33, pp. 1-50, 2001.

[2] A. M. H. Won and G. V. Eleftheriade, "Advances in Imaging Beyond the Diffraction Limit," *IEEE Photonics Journal,* vol. 4, pp. 556-589, 2012.

[3] B. Huang, M. Bates and X. Zhuang, "Super resolution fluorescence microscopy," *Annu. Rev. Biochem.,* vol. 78, pp. 993-1016, 2009.

[4] S. W. Hell and J. Wichmann, "Breaking the diffraction resolution limit by stimulated emission: stimulated-emission-depletion fluorescence microscopy," *Opt. Lett.,* vol. 19, pp. 780-782, 1994.

[5] E. Betzig, G. H. Patterson and H. F. Hess, "Imaging intracellular fluorescent proteins at nanometer resolution," *Science,* vol. 313, pp. 1642-1645, 2006.

[6] M. J. Rust, M. Bates and X. Zhuang, "Sub-diffraction-limit imaging by stochastic optical reconstruction microscopy (STORM)," *Nat. Methods,* vol. 3, pp. 793-795, 2006.

[7] M. G. Gustafsson, "Surpassing the lateral resolution limit by a factor of two using structured illumination microscopy," *J Microsc.,* vol. 198, pp. 82-87, 2000.

[8] F. J. Garcia-Vidal, L. Martin-Moreno, T. W. Ebbesen and L. Kuipers, "Light passing through sub-wavelength apertures," *Rev. Mod. Phys.,* vol. 82, pp. 729-787, 2010.

[9] Z. G. Chen, A. Taflove and V. Backman, "Photonic nanojet enhancement of backscattering of light by nanoparticles: a potential novel visible-light ultramicroscopy technique," *Opt. Exp.,* vol. 12, pp. 1214-1220, 2004.

[10] S. Kong, A. V. Sahakian, A. Heifetz, A. Taflove and V. Backman, "Robust detection of deeply sub-wavelength pits in simulated optical data-storage disks using photonic jets," *Appl. Phys. Lett.,* vol. 92, p. 211102, 2008.

[11] J. Ferrand, J. Wenger, A. Devilez, M. Pianta and B. Stout et al, "Direct imaging of photonic nanojets," *Opt. Exp.,* vol. 16, pp. 6930-6940, 2008.

[12] I. Mahariq and H. Kurt, "On- and off-optical-resonance dynamics of dielectric microcylinders under plane wave illumination," *J. Opt. Soc. Am. B,* vol. 32, pp. 1022-1030, 2015.

[13] I. Mahariq, V. Astratov and H. Kurt, "Persistence of photonic nanojet formation under the deformation of circular boundary," *J. Opt. Soc. Am. B,* vol. 33, pp. 535-542, 2016.

[14] B. Lukyanchuk, R. P. Domínguez, I. Minin, O. Minin and Z. Wang, "Refractive index less than two: photonic," *Opt. Mat. Exp.,* vol. 7, pp. 1820-1847, 2017.

[15] Z. Wang, W. Guo, L. Li, B. Luk'yanchuk, A. Khan, Z. Liu, Z. Chen and M. Hong, "Optical virtual imaging at 50 nm lateral resolution with a white-light nanoscope," *Nature Commun.,* vol. 2, p. 218, 2011.

[16] L. A. Krivitsky, J. J. Wang, Z. Wang and B. Lukyanchuk, "Locomotion of microspheres for super-resolution imaging," *Sci. Rep.,* vol. 3, p. 3501, 2013.

[17] D. Gerard, A. Devilez, H. Aouani, B. Stout, N. Bonod, J. Wenger, E. Popov and H. Rigneault, "Efficient excitation and collection of single-molecule fluorescence close to a dielectric microsphere," *J. Opt. Soc. Am. B,* vol. 26, pp. 1473-1478, 2009.

[18] D. Gerard, J. Wenger, A. Devilez, D. Gachet, B. Stout, N. Bonod, E. Popov and H. Rigneault, "Strong electromagnetic confinement near dielectric microspheres to enhance single-molecule fluorescence," *Opt. Exp.,* vol. 16, pp. 15297-15303, 2008.

[19] S. Lee, L. Li, Y. Ben-Aryeh, Z. Wang and W. Guo, "Overcoming the diffraction limit induced by microsphere optical nanoscopy," *J. Opt.,* vol. 15, p. 125710, 2013.

[20] J. A. Stratton, Electromagnetic Theory, New York: McGraw-Hill Book Company Inc., 1941.

[21] H. C. van de Hulst, Light scattering by small particles, New York: Dovar Publications, Inc., 1957.

[22] C. F. Bohren and D. R. Huffman, Absorption and Scattering of Light by Small Particles, New York: John Wiley & Sons, Inc., 1983.

[23] M. Kerker, The scattering of light and other electromagnetic radiation, New York: Academic Press Inc., 1969.

[24] M. I. Mishchenko, J. W. Hovenier and L. Travis, Light Scattering by Nonspherical Particles: Theory,Measurements, and Applications, San Diego, California: Academic Press, 2000.

[25] M. J. Riedl, Optical design fundamentals for infrared systems, 2nd Edition, Bellingham USA: SPIE Press, 2001.

[26] J. P. Barton, D. R. Alexander and S. A. Schaub, "Internal and near-surface electromagnetic fields for a spherical particle irradiated by a focused laser beam," *J. Appl. Phys.,* vol. 64, pp. 1632-1639, 1988.

[27] H. J. Münzer, M. Mosbacher, M. Bertsch, J. Zimmermann, P. Leiderer and J. Boneberg, "Local field enhancement effects for nanostructuring of surfaces," *J. Microsc. ,* vol. 202, p. 129–135, 2001.

[28] M. Mosbacher, H.-J. Münzer, J. Zimmermann, J. Solis, J. Boneberg and P. Leiderer, "Optical field enhancement effects in laser-assisted particle removal," *Appl. Phys., A Mater. Sci. Process. ,* vol. 72, p. 41–44, 2001.

[29] Y. W. Zheng, B. S. Luk'yanchuk, Y. F. Lu, W. D. Song and Z. H. Mai, "Dry laser cleaning of particles from solid substrates: experiments and theory," *J. Appl. Phys. ,* vol. 90, p. 2135–2142 , 2001.

[30] Y. F. Lu, L. Zhang, W. D. Song, Y. W. Zheng and B. S. Luk'yanchuk, "Laser writing of a sub-wavelength structure on silicon (100) surfaces with particle enhanced optical irradiation," *JETP Lett.,* vol. 72, pp. 457-459, 2000.

[31] P. Leiderer, C. Bartels, J. König-Birk, M. Mosbacher and J. Boneberg, "Imaging optical near-fields of nanostructures," *Appl. Phys. Lett.,* vol. 85, pp. 5370-5372, 2004.

[32] S. M. Huang, M. H. Hong, Y. F. Lu, B. S. Luk'yanchuk, W. D. Song and T. C. Chong, "Pulsed laser-assisted surface structuring with optical near-field enhanced effects," *J. Appl. Phys.,* vol. 92, pp. 2495-2500, 2002.

[33] K. Piglmayer, R. Denk and D. Bäuerle, "Laser-induced surface patterning by means of microspheres," *Appl. Phys. Lett.,* vol. 80, pp. 4693-4695, 2002.

[34] P. Wu, J. Li, K. Wei and W. Yue, "Tunable and ultra-elongated photonic nanojet generated by a liquid-immersed core–shell dielectric microsphere," *Appl. Phys. Exp.,* vol. 8, p. 112001, 2015.

[35] S. C. Kong, A. Taflove and V. Backman, "Quasi one-dimensional light beam generated by a graded-index microsphere," *Opt. Exp.,* vol. 17, pp. 3722-3731, 2009.

[36] C. Y. Liu, "Ultra-elongated photonic nanojets generated by a graded-index microellipsoid," *Prog. Electromag. Res. Lett.,* vol. 37, pp. 153-165, 2013.

[37] M. Kim, T. Scharf, S. Mühlig, C. Rockstuhl and H. P. Herzig, "Engineering

photonic nanojets," *Opt. Exp.,* vol. 19, pp. 10206-10220, 2011.

[38] A. Heifetz, S. C. Kong, A. V. Sahakian, A. Taflove and V. Backman, "Photonic Nanojets," *J. Comput. Theor. Nanosci.,* vol. 6, pp. 1979-1992, 2009.

[39] K. J. Yi, H. Wang, Y. F. Lu and Z. Y. Yang, "Enhanced Raman scattering by self-assembled silica spherical microparticles," *J. Appl. Phys.,* vol. 101, p. 063528, 2007.

[40] J. F. Cardenas, "Raman scattering enhancement by dielectric spheres," *J. Raman Spectrosc.,* vol. 44, pp. 540-543, 2013.

[41] T. W. Chang, X. Wang, A. Mahigir, G. Veronis, G. L. Liu and M. R. Gartia, "Marangoni Convection Assisted Single Molecule Detection with Nanojet Surface Enhanced Raman Spectroscopy," *ACS Sens.,* vol. 2, pp. 1133-1138, 2017.

[42] W. A. Challener and A. V. Itagi, "Near-Field Optics for Heat-Assisted Magnetic Recording (Experiment, Theory, and Modeling)," in *Modern Aspects of Electrochemistry, 44, M. Schlesinger (Ed.)*, New York, Springer, 2009, pp. 53-111.

[43] W. Wu, A. Katsnelson, O. Memis and H. Mohseni, "A deep sub-wavelength process for the formation of highly uniform arrays of nanoholes and nanopillars," *Nanotechnology,* vol. 18, p. 485302, 2007.

[44] E. McLeod and C. Arnold, "Sub-wavelength direct-write nanopatterning using optically trapped microspheres," *Nat. Nanotechnol.,* vol. 3, pp. 413-417, 2008.

[45] F. J. Valdivia-Valero and M. Nieto-Vesperinas, “Optical forces on cylinders near sub-wavelength slits illuminated by a photonic nanojet,” *Opt. Comm.,* vol. 294, p. 351–360, 2013.

[46] L. Yue, O. V. Minin, Z. Wang, J. N. Monks, A. S. Shalin and I. V. Minin, “Photonic hook: a new curved light beam,” *Opt. Lett.,* vol. 43, pp. 771-774, 2018.

[47] H. Wang, X. Wu and D. Shen, “Trapping and manipulating nanoparticles in photonic nanojets,” *Opt. Lett.,* vol. 41, pp. 1652-1655, 2016.

[48] K. W. Allen, A. Darafsheh, F. Abolmaali, N. Mojaverian and N. I. Limberopoulos et al., “Microsphere-chain waveguides: Focusing and transport properties,” *Appl. Phys. Lett.,* vol. 105, p. 021112, 2014.

[49] X. Hao, C. Kuang, X. Liu, H. Zhang and Y. Li, “Microsphere based microscope with optical super-resolution capability,” *Appl. Phys. Lett.,* vol. 99, p. 203102, 2011.

[50] H. Yang, N. Moullan, J. Auwerx and M. A. M. Gijs, “Super□Resolution Biological Microscopy Using Virtual Imaging by a Microsphere Nanoscope,” *Small,* vol. 10, p. 1712–1718, 2014.

[51] L. Li, W. Guo, Y. Yan, S. Lee and T. Wang, “Label-free super-resolution imaging of adenoviruses by submerged microsphere optical nanoscopy,” *Light: Sci. Appl.,* vol. 2, p. e104, 2013.

[52] F. Wang, L. Liu, H. Yu, Y. Wen and P. Yu et al., “Scanning superlens microscopy for non-invasive large field-of-view visible light nanoscale imaging,” *Nat. Comm.,* vol. 7, p. 13748, 2016.

[53] A. Darafsheh, N. I. Limberopoulos, J. S. Derov, D. E. Walker Jr. and V. N. Astratov, “Advantages of microsphere-assisted super-resolution imaging technique over solid immersion lens and confocal microscopie,” *Appl. Phys. Lett.,* vol. 104, p. 061117, 2014.

[54] W. Fan, B. Yan, Z. Wang and L. Wu, “Three-dimensional all-dielectric metamaterial solid immersion lens for sub-wavelength imaging at visible frequencies,” *Sci. Adv.,* vol. 2, p. e1600901, 2016.

[55] M. I. Mishchenko, L. D. Travis and D. W. Mackowski, “T-matrix computations of light scattering by nonspherical particles: A review,” *J. Quant. Spectrosc. Radiat. Transfer,* vol. 55, pp. 535-575, 1996.

[56] R. F. Harrington, Field Computation by Moment Methods, New York: IEEE Press, 1993.

[57] E. M. Purcell and C. R. Pennypacker, “Scattering and Absorption of Light by Nonspherical Dielectric Grains,” *Astrophys. J.,* vol. 186, pp. 705-714, 1973.

[58] B. T. Draine and P. J. Flatau, “Discrete-dipole approximation for scattering calculations,” *J. Opt. Soc. Am. A,* vol. 11, pp. 1491-1499, 1994.

[59] B. T. Draine and J. Goodman, "Beyond Clausius-Mossotti - Wave propagation on a polarizable point lattice and the discrete dipole approximation," *Astrophys. J.,* vol. 405, pp. 685-697, 1993.

[60] K. Yee, "Numerical solution of initial boundary value problems involving Maxwell's equations in isotropic media," *IEEE Transactions on Antennas and Propagation,* vol. 14, pp. 302-307, 1966.

[61] A. Taflove and S. C. Hagness, Computational Electrodynamics: The Finite-Difference Time-Domain Method II Ed, Boston: Artech House, 2000.

[62] J. Parsons, C. P. Burrows, J. R. Sambles and W. L. Barnes, "A comparison of techniques used to simulate the scattering of electromagnetic radiation by metallic nanostructures," *J. Mod. Opt.,* vol. 57, p. 1362, 2010.

[63] G. W. Mulholland, C. F. Bohren and K. A. Fuller, "Light-scattering by agglomerates - coupled electric and magnetic dipole method," *Langmuir,* vol. 10, pp. 2533-2546, 1994.

[64] V. L. Loke, M. P. Menguc and T. A. Nieminen, "Discrete dipole approximation with surface interaction: Computational toolbox for MATLAB," *J. Quat. Spect. Radiat. Trans.,* vol. 27, pp. 2293-2303, 2010.

[65] B. T. Draine and P. J. Flatau, "Discrete-dipole approximation for periodic targets," *J. Opt. Soc. Am. A,* vol. 25, pp. 2593-2703, 2008.

[66] J. Jin, The Finite Element Method in Electromagnetics, 2nd ed., New York: John Wiley & Sons, 2002.

[67] S. G. Johnson, "Notes on perfectly matched layers, http://math.mit.edu/ stevenj/18.369/pml.pdf," 2010.

[68] Comsol Inc , Comsol Multiphysics, Burlington, MA, 2015.

[69] M. H. Jyothi, D. Bipin and B. Choudhury, "Design and Optimization of Multilayer Ideal Cloak," in *COMSOL Conference*, Bangalore, India, October 20-21, 2016.

[70] WiTec, "WiTec Alpha300 User Manual," WiTec GmbH, Ulm, Germany, 2008.

[71] E. Synge, "A suggested method for extending microscopic resolution into the ultra-microscopic region," *Philosophical Magazine Series 7,* vol. 6, pp. 356-362, 1928.

[72] R. Dantham, P. Bisht and C. Namboodiri, "Enhancement of Raman scattering by two orders of magnitude using photonic nanojet of a microsphere," *J. Appl. Phys.,* vol. 109, p. 103103., 2011.

[73] P. Ghenuche, J. Torres, P. Ferrand and J. Wenger, "Multi-focus parallel detection of fluorescent molecules at picomolar concentration with photonic nanojets arrays," *Appl. Phys. Lett.,* vol. 105, p. 131102, 2014.

[74] J. Kim, K. Cho, I. Kim, W. Kim, T. Lee and K. Lee, "Fabrication of plasmonic nanodiscsby photonic nanojet lithography," *Appl. Phys. Exp.,* vol. 5, p. 025201, 2012.

[75] A. Heifetz, S. Kong, A. Sahakian, A. Taflove and V. Backman, "Photonic nanojet," *J. Comput. Theor. Nanosci.,* vol. 6, pp. 1979-1999, 2009.

[76] I. V. Minin, O. V. Minin and Y. E. Geints, "Localized EM and photonic jets from nonspherical and non-asymmetrical dielectric mesoscale objects: Brief review," *Ann. Phys. (Berlin),* vol. 527, pp. 491-497, 2015.

[77] C. Y. Liu, "Photonic jets produced by dielectric micro cuboids," *Appl. Opt.,* vol. 54, pp. 8694-8699, 2015.

[78] I. V. Minin, O. V. Minin, V. Pacheco-Peña and M. Beruete, "Localized photonic jets from flat, three dimensional dielectric cuboids in the reflection mode," *Opt. Lett.,* vol. 40, pp. 2329-2332, 2015.

[79] D. M. Closkey, J. J. Wang and J. F. Donegan, "Low divergence photonic nanojets from Si3N4 micro-disks," *Opt. Exp.,* vol. 20, pp. 128-140, 2012.

[80] Y. Shen, L. V. Wang and J. T. Shen, "Ultralong photonic nanojet formed by a two-layer dielectric microsphere," *Opt. Lett.,* vol. 39, pp. 4120-4123, 2014.

[81] P. K. Kushwaha, H. S. Patel, M. K. Swami and P. Gupta, "Controlled shaping of photonic nanojets using core shell microspheres," *SPIE Proceedings,* vol. 9654, p. 96541H, 2015.

[82] C. Liu, "Photonic nanojet shaping of dielectric non-spherical micro particles," *Physica E,* vol. 64, pp. 23-28, 2014.

[83] C. Liu and F. Lin, “Geometric effect on photonic nanojet generated by dielectric micro-cylinders with non-cylindrical cross-sections,” *Opt. Commun.,* vol. 380, pp. 287-296, 2016.

[84] N. Eti, I. H. Giden, Z. Hayran, B. Rezaei and H. Kurt, “Manipulation of photonic nanojet using liquid crystals for elliptical and circular core–shell variations,” *J. Mod. Opt.,* vol. 64, pp. 1566-1577, 2017.

[85] G. Kattawar, C. Li, P. W. Zhai and P. Yang, “Electric and magnetic energy density distributions inside and outside dielectric particles illuminated by a plane electromagnetic wave,” *Opt. Exp.,* vol. 13, pp. 4554-4559, 2005.

[86] G. Gouesbet and G. Grehan, “Generalized Lorentz–Mie theory for a sphere with an eccentrically located spherical inclusion,” *J. Mod. Opt.,* vol. 47, pp. 821-837, 2000.

[87] V. S. C. M. Rao and S. D. Gupta, “Broken azimuthal degeneracy with whispering gallery modes of microspheres,” *J. Opt. A: Pure Appl. Opt.,* vol. 7, pp. 279-285, 2005.

[88] Y. E. Geints, A. A. Zemlyanov and E. K. Panina, “Localized light jets from radially symmetric non-spherical dielectric microparticles,” *Atmos. Ocean. Opt.,* vol. 28, pp. 436-440, 2015.

[89] Y. E. Geints, I. V. Minin, E. K. Panina, A. A. Zemlyanov and O. V. Minin, “Comparison of photonic nanojets key parameters produced by nonspherical microparticles,” *Opt. Quant. Electron.,* vol. 49, pp. 1-7, 2017.

[90] T. Jalali and D. Erni, “Highly confined photonic nanojet from elliptical particles,” *J. Mod. Opt.,* vol. 61, pp. 1069-1076, 2014.

[91] G. B. Sukhorukov, E. Donath, S. Davis, H. Lichtenfeld, F. Caruso, V. I. Popov and H.Mohwald, “Stepwise polyelectrolyte assembly on particle surfaces: a novel approachto colloid design,” *Polym. Adv. Technol.,* vol. 9, pp. 759-767, 1998.

[92] S. H. Kim, A. Abbaspourrad and D. A. Weitz, “Amphiphilic crescent-moon-shaped microparticles formed by selective adsorption of colloids,” *J. Am. Chem. Soc.,* vol. 133, pp. 5516-5524, 2011.

[93] J. Li, S. Ding, C. Zhang and Z. Yang, “Synthesis of composite eccentric double-shelled hollow spheres,” *Polymer,* vol. 50, pp. 3943-3949, 2009.

[94] Q. Wang, L. Yu, C. Liu and X. Xu, “Enhancement of multipolar Fano resonances by nanocrescent elliptical disk structures,” *Euro. Phys. Lett.,* vol. 118, p. 64002, 2017.

[95] A. Aubry, D. Y. Lei, A. I. Fernandez-Dominguez, Y. Sonnefraud, S. A. Maier and J. B.Pendry, “Plasmonic light-harvesting devices over the whole visible spectrum,” *Nano Lett.,* vol. 10, pp. 2574-2579, 2010.

[96] A. Atre, A. Garca-Etxarri, H. Alaeian and J. Dionne, “Toward high-efficiency solar up-conversion with plasmonic nanostructures,” *J. Opt.,* vol. 14, p. 024008, 2012.

[97] E. E. Ekanem, Z. Zhang and G. T. Vladisavljevic, “Facile microfluidic production of composite polymer core–shell microcapsules and crescent-shaped

microparticles," *J. Colloid Interface Sci.,* vol. 498, pp. 387-394, 2017.

[98] A. S. Ang, A. Karabchevsky, I. V. Minin, O. V. Minin, S. V. Sukhov and A. S. Shalin, "Photonic Hook' based optomechanical nanoparticle manipulator," *Scientific Reports,* vol. 8, p. 2029, 2018.

[99] N. C. Lindquist, J. Jose, S. Cherukulappurath, X. Chen, T. W. Johnson and S. H. Oh, "Tip□based plasmonics: squeezing light with metallic nanoprobes," *Las. Photonic. Rev.,* vol. 7, pp. 453-477, 2013.

[100] J. S. Bouillard, S. Vilain, W. Dickson and A. V. Zayats, "Hyperspectral imaging with scanning near-field optical microscopy: applications in plasmonics," *Opt. Exp.,* vol. 18, pp. 16513-16519, 2010.

[101] B. Hecht, B. Sick, U. P. Wild, V. Deckert, R. Zenobi, O. J. F. Martin and D. W. Pohl, "Scanning near-field optical microscopy with aperture probes: Fundamentals and applications," *J. Chem. Phys.,* vol. 112, pp. 7761-7774, 2000.

[102] Novotny, L. and C. Hafner, "Light propagation in a cylindrical waveguide with a complex, metallic, dielectric function," *Phys. Rev. E,* vol. 50, pp. 4094-4106, 1994.

[103] T. J. Antosiewicz, P. Wróbel and T. Szoplik, "Performance of Scanning Near-Field Optical Microscope Probes with Single Groove and Various Metal Coatings," *Plasmonics,* vol. 6, pp. 11-18, 2011.

[104] E. X. Jin and X. Xu, "Enhanced optical near field from a bowtie aperture," *Appl.*

Phys. Lett., vol. 88, p. 153110, 2006.

[105] P. Burgos, Z. Lu, A. Ianoul, C. Hnatovsky, M. L. Viriot, L. J. Johnston and R. S. Taylor, “Nearfield scanning optical microscopy probes: a comparison of pulled and double etched bent NSOM probes for fluorescence imaging of biological samples,” *J. Microsc.,* vol. 211, pp. 37-47, 2003.

[106] M. Celebrano, P. Biagioni, M. Zavelani-Rossi and D. Polli, “Hollow-pyramid based scanning near-field optical microscope coupled to femtosecond pulses: A tool for nonlinear optics at the nanoscale,” *Rev. Sci. Instrum.,* vol. 80, p. 033704, 2009.

[107] H. La Rosa, B. I. Yakobson and H. D. Hallen, “Origins and effects of thermal processes on nearfield optical probes,” *Appl. Phys. Lett.,* vol. 67, pp. 2597-2599, 1995.

[108] E. S. Erickson and R. C. Dunn, “Sample heating in near-field scanning optical microscopy,” *Appl. Phys. Lett.,* vol. 87, p. 201102, 2005.

[109] F. Zenhausern, M. P. O’Boyle and H. K. Wickramasinghe, “Apertureless near□field optical microscope,” *Appl. Phys. Lett.,* vol. 65, pp. 1623-1625, 1994.

[110] L. Aeschimann, “Apertureless Scanning Near-Field, PhD Thesis Institute of Microtechnology, University of Neuchâtel,” Switzerland, 2004.

[111] L. Wang and X. Xua, “High transmission nanoscale bowtie-shaped aperture probe for near-field optical imaging,” *Appl. Phys. Lett.,* vol. 90, p. 261105, 2007.

[112] A. Naber, D. Molenda, U. C. Fischer, H. J. Maas, C. Hoppener and N. F. H. Lu, "Enhanced Light Confinement in a Near-Field Optical Probe with a Triangular Aperture," *Phys. Rev. Lett.,* vol. 89, p. 210801, 2002.

[113] J. A. Matteo, D. P. Fromm, Y. Yuen, P. J. Schuck, W. E. Moerner and L. Hesselink, "Spectral analysis of strongly enhanced visible light transmission through single C-shaped nanoapertures," *Appl. Phys. Lett.,* vol. 85, pp. 648-650, 2004.

[114] J. A. Matteo and L. Hesselink, "Fractal extensions of near-field aperture shapes for enhanced transmission and resolution," *Opt. Exp.,* vol. 13, pp. 636-647, 2005.

[115] W. Bao and N. C. F. R. D. S. W. e. a. M. Melli, "Mapping Local Charge Recombination Heterogeneity by Multidimensional Nanospectroscopic Imaging," *Science,* vol. 338, pp. 1317-1321, 2012.

[116] H. Guo, Y. Han, X. Weng, Y. Zhao, G. Sui, Y. Wang and S. Zhuang, "Near-field focusing of the dielectric microsphere with wavelength scale radius," *Opt. Exp.,* vol. 21, pp. 2434-2443, 2013.

[117] Y. Chen, Y. Luo and X. Xie, "Improving near-field throughput in a hollow metallic tapered waveguide via wavefront modulation," *J. Mod. Opt.,* vol. 60, pp. 1359-1363, 2013.

[118] E. Betzig, J. K. Trautman, J. S. Weiner, T. D. Harris and R. Wolfe, "Polarization contrast in near-field scanning optical microscopy," *Appl. Opt.,* vol. 31, pp. 4563-4568, 1992.

[119] R. Micheletto, M. Allegrini and Y. Kawakami, "Near-field evidence of local polarized emission centers in InGaN/GaN materials," *Appl. Phys. Lett.,* vol. 95, p. 211904, 2009.

[120] A. Ambrosio, M. Alderighi, M. Labardi, L. Pardi and F. Fuso, "Near-field optical microscopy of polymer-based films with dispersed terthiophene chromophores for polarizer applications," *Nanotech.,* vol. 15, pp. S270-S275, 2004.

[121] T. Setälä, A. Shevchenko, M. Kaivola and A. T. Friberg, "Degree of polarization for optical near fields," *Phys. Rev. E,* vol. 66, pp. 016615-7, 2002.

[122] J. J. Gil, "Intrinsic Stokes parameters for 3D and 2D polarization states," *J. Eur. Opt. Soc. -RP,* vol. 10, p. 15054, 2015.

[123] L. R. Shobin and S. Manivannan, "One pot rapid synthesis of silver nanowires using NaCl assisted glycerol mediated polyol process," *Electron. Mater. Lett.,* vol. 10, pp. 1027-1031, 2014.

[124] A. Pucci, F. Neubrech, J. Aizpurua, T. Cornelius and M. L. Chapelle, "Electromagnetic nanowire resonances for field-enhanced spectroscopy," in *One-Dimensional Nanostructures ed Z M Wang*, New York, Springer, 2008, pp. 175-215.

[125] M. K. Swami, H. S. Patel, A. Uppal, P. K. Kushwaha and P. K. Gupta, "Spectral Mueller matrix measurements for characterization of depolarization from non-spherical gold nanoparticles," *Opt. Comm.,* vol. 308, pp. 136-141, 2013.

[126] M. K. Swami, H. S. Patel, P. Geethu, A. Uppal, P. K. Kushwaha and P. K. Gupta, "Effect of gold nanoparticles on depolarization characteristics of Intralipid tissue phantom," *Opt. Lett.,* vol. 38, pp. 2855-2857, 2013.

[127] S. Melle, J. L. Menéndez and G. Armelles, "Magneto-optical properties of nickel nanowire arrays," *Appl. Phys. Lett.,* vol. 83, pp. 4547-4549, 2003.

[128] G. Schider, J. R. Krenn, W. Gotschy, B. Lamprecht and H. Ditlbacher et al., "Optical properties of Ag and Au nanowire gratings," *J. Appl. Phys.,* vol. 90, pp. 3825-3830, 2001.

[129] N. G. Khlebtsov, "Anisotropic properties of plasmonic nanoparticles: depolarized light scattering, dichroism, and birefringence," *J. Nanophot.,* vol. 4, p. 041587, 2010.

[130] L. A. Nafie, "Recent advances in linear and non□linear Raman spectroscopy. Part X," *J. Raman Spectrosc.,* vol. 47, pp. 1548-1565, 2016.

[131] T. J. Vickers, C. K. Mann, J. Zhu and C. K. Chong, "Quantitative Resonance Raman Spectroscopy," *Appl. Spectrosc. Rev.,* vol. 26, pp. 341-375, 1991.

[132] A. Kudelski, "Analytical applications of Raman spectroscopy," *Talanta,* vol. 76, pp. 1-8, 2008.

[133] W. J. Tipping, M. Lee, A. Serrels, V. G. Brunton and A. N. Hulme, "Stimulated Raman scattering microscopy: an emerging tool for drug discovery," *Chem. Soc.*

Rev., vol. 45, pp. 2075-2089, 2016.

[134] R. S. Das and Y. K. Agrawal, "Raman spectroscopy: Recent advancements, techniques and applications," *Vib. Spectrosc.,* vol. 57, pp. 163-176, 2011.

[135] G. M. Das, R. Laha and V. R. Dantham, "Photonic nanojet mediated SERS technique for enhancing the Raman scattering of a few molecules," *J. Raman Spectrosc.,* vol. 47, pp. 895-900, 2016.

[136] M. Cicerone, "Molecular imaging with CARS micro-spectroscopy," *Curr. Opin. Chem. Biol.,* vol. 33, pp. 179-185, 2016.

[137] K. Kneipp, Y. Wang, H. Kneipp, L. T. Perelman and I. Itzkan et al., "Single Molecule Detection Using Surface-Enhanced Raman Scattering (SERS)," *Phys. Rev. Lett.,* vol. 78, pp. 1667-1670, 1997.

[138] E. Bailo and V. Deckert, "Tip-enhanced Raman scattering," *Chem. Soc. Rev.,* vol. 37, pp. 921-930, 2008.

[139] M. V. Jouravlev, "Formation of optical fields of stimulated Raman scattering with a resolution beyond the Abbe diffraction limit by spherical microlens cavities with whispering gallery modes: Near-field approximation," *Opt. Spectrosc.,* vol. 112, pp. 624-630, 2012.

[140] P. K. Upputuri, Z. Wu, L. Gong, C. K. Ong and H. Wang, "Super-resolution coherent anti-Stokes Raman scattering microscopy with photonic nanojets," *Opt.*

Exp., vol. 22, pp. 12890-12899, 2014.

[141] I. Alessandri, N. Bontempi and L. E. Depero, “Colloidal lenses as universal Raman scattering enhancers,” *RSC Adv.,* vol. 4, pp. 38152-38158, 2014.

[142] M. Duocastella, F. Tantussi, A. Haddadpour, R. P. Zaccaria and A. Jacassi et al, “Combination of scanning probe technology with photonic nanojets,” *Sci. Rep.,* vol. 7, p. 3474, 2017.

[143] A. Desmedt, D. Talaga and J. L. Bruneel, “Enhancement of the Raman Scattering Signal Due to a Nanolens Effect,” *Appl. Spectrosc.,* vol. 61, pp. 621-623, 2007.

[144] C. L. Du, J. Kasim, Y. M. You, D. N. Shi and Z. X. Shen, “Enhancement of Raman scattering by individual dielectric microspheres,” *J. Raman Spectrosc.,* vol. 42, pp. 145-148, 2011.

[145] Y. Z. Yan, C. Xing, Y. H. Jia, Y. Zeng, Y. Zhao and Y. J. Jiang, “Self-assembled dielectric microsphere array enhanced Raman scattering for large-area and ultra-long working distance confocal detection,” *Opt. Exp.,* vol. 23, pp. 25854-25865, 2015.

[146] I. Alessandri and J. R. Lombardi, “Enhanced Raman Scattering with Dielectrics,” *Chem. Rev.,* vol. 116, pp. 14921-14981, 2016.

[147] D. E. Aspnes and A. A. Studna, “Dielectric functions and optical parameters of Si, Ge, GaP, GaAs, GaSb, InP, InAs, and InSb from 1.5 to 6.0 eV,” *Phys. Rev. B,* vol.

27, pp. 985-1009, 1983.

[148] B. Riscob, I. Bhaumik, S. Ganesamoorthy, R. Bhatt and N. Vijayan et al., "Crystal growth of Ru-doped congruent LiNbO3 and investigation of crystalline perfection and optical properties," *J. Appl. Cryst.,* vol. 48, pp. 1753-1760, 2015.

[149] N. J. Everall, "Modeling and Measuring the Effect of Refraction on the Depth Resolution of Confocal Raman Microscopy," *Appl. Spectrosc.,* vol. 54, pp. 773-782, 2000.

[150] A. Darafsheh, "Influence of the background medium on imaging performance of microsphere-assisted super-resolution microscopy," *Opt. Lett.,* vol. 42, pp. 735-738, 2017.